INFORMATION TO USERS

This manuscript has been reproduced from the microfilm master. UMI films the text directly from the original or copy submitted. Thus, some thesis and dissertation copies are in typewriter face, while others may be from any type of computer printer.

The quality of this reproduction is dependent upon the quality of the copy submitted. Broken or indistinct print, colored or poor quality illustrations and photographs, print bleedthrough, substandard margins, and improper alignment can adversely affect reproduction.

In the unlikely event that the author did not send UMI a complete manuscript and there are missing pages, these will be noted. Also, if unauthorized copyright material had to be removed, a note will indicate the deletion.

Oversize materials (e.g., maps, drawings, charts) are reproduced by sectioning the original, beginning at the upper left-hand corner and continuing from left to right in equal sections with small overlaps.

ProQuest Information and Learning
300 North Zeeb Road, Ann Arbor, MI 48106-1346 USA
800-521-0600

University of Alberta

QUANTIFYING AND MODELLING THE SPATIO-TEMPORAL DYNAMICS OF NUCLEAR PROTEINS

by

Gustavo Carrero

A thesis submitted to the Faculty of Graduate Studies and Research
in partial fulfillment of the requirements for the degree of
Doctor of Philosophy

in

Applied Mathematics

Department of Mathematical and Statistical Sciences
Edmonton, Alberta
Fall 2005

From a mathematical point of view, the art of good modelling relies on: (i) a sound understanding and appreciation of the biological problem; (ii) a realistic mathematical representation of the important biological phenomena; (iii) finding useful solutions, preferably quantitative; and what is crucially important (iv) a biological interpretation of the mathematical results in terms of insights and predictions. The mathematics is dictated by the biology and not vice-versa. Sometimes the mathematics can be very simple. Useful mathematical biology research is not judged by mathematical standards but by different and no less demanding ones.

J.D. Murray [77]

ABSTRACT

The combination of fluorescence microscopy techniques and mathematical modelling facilitates the study of two important aspects of the dynamics of nuclear proteins in living cells: (i) the quantitative assessment of the mobility of the proteins, and (ii) their spatial organization in the cell nucleus. The first aspect is addressed by examining three models that can be used to interpret experimental FRAP (fluorescence recovery after photobleaching) data: a diffusion model, a reaction-diffusion model, and a compartmental model. The second aspect is addressed by developing a fourth-order aggregation-diffusion model, whose dynamics provide an explanation for the aggregation of nuclear proteins.

The diffusion model describes the dynamics of diffusive nuclear proteins. By analyzing FRAP data with this model, estimates of effective diffusion coefficients can be obtained. It is shown that these estimates can be affected by the presence of the nuclear membrane. The reaction-diffusion model and the compartmental model describe the dynamics of diffusive nuclear proteins undergoing binding events. The analysis of these models leads to an elegant explanation of two important limiting dynamical types of behaviour exhibited by FRAP data, namely a reduced diffusive behaviour, and a biphasic behaviour. The results are used to characterize FRAP data of two nuclear proteins: histone H1 and actin, and to estimate kinetic parameters such as binding and unbinding rates.

The fourth-order aggregation-diffusion model provides a description of the aggregation process undergone by splicing factors (nuclear proteins which play an important role in RNA splicing). A linear stability analysis of the model reveals the emergence of spatial patterns, and a bifurcation analysis is used to delimit regions of stability and instability.

ACKNOWLEDGEMENTS

I would like to express my sincere and greatest gratitude to Dr. Gerda de Vries for sharing her knowledge and joy of mathematical biology, and being a wonderful teacher and supervisor. I am also greatly indebted to Dr. Michael Hendzel for presenting the biological problems addressed in this thesis as a challenge for interdisciplinary work, and offering his experimental expertise that made possible this research. I am grateful to the members of Michael Hendzel's lab at the Cross Cancer Institute, specifically to Ellen Crawford and Darin McDonald, for the invaluable help in providing the experimental data presented in this thesis, and answering all my trivial questions about biological processes.

I also wish to show my appreciation to Dr. Thomas Hillen and Dr. Mark Lewis who were always willing to offer suggestions and feedback. Special thanks to Dr. Karl Hadeler for suggesting the use of compartmental modelling in the analysis of FRAP data.

This research was supported by MITACS (The Mathematics of Information Technology and Complex Systems), a Canadian Network of Centres of Excellence for the Mathematical Sciences. I would like to acknowledge Dr. Jack Tuszynski, who has kept alive this research as a MITACS project.

Finally, it is a pleasure to thank my wife, Nury, for her continuous loving support and her spontaneous and beautiful smile that always gives me strength.

Table of Contents

List of Tables

List of Figures

Chapter 1

Introduction

The study of the dynamics of nuclear proteins has received an enormous amount of attention during the last fifteen years. The reason for such a strong interest is related to the important roles that nuclear proteins play in the regulation of gene expression and in the development of new technologies that have allowed experimentalists to explore the microscopic world of the nucleus in eukaryotic cells.

One of the major consequences of the sequencing of entire genomes, and the resulting studies that examine whole genome changes in gene expression, is the need to address the complexity of the cellular environment [5, 23, 67, 81, 89, 93]. Fortunately, the cell nucleus has a less complex topology than the cytoplasm. Rather than containing a multitude of membrane-bound structures, the cell nucleus contains only an outer membrane that restricts the flow of molecules greater than approximately 50 KDa. Because there are no membrane barriers within the interior of the nucleus, the environment is relatively homogeneous and accessible by diffusion [67]. Besides diffusion, binding events between smaller molecules, such as proteins, and larger molecules, such as chromosomes, may be the principal determinant of how molecules move through and spatially distribute within the nucleoplasm [10]. Obtaining measurements of the molecular diffusivity, the binding events and how, for example, mutations in proteins change these binding events, is a critical stepping stone to quantitative modelling of the functional dynamics of the genome [20, 88].

The method that is most commonly used to obtain measurements of the move-

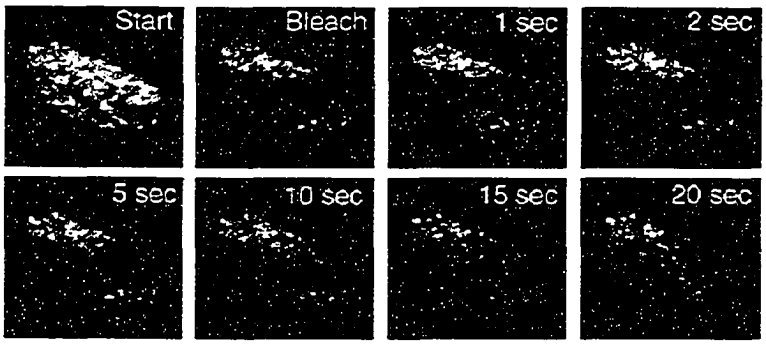

Figure 1.1: Example of a FRAP experiment. The image was obtained at Dr. Hendzel's lab at the Cross Cancer Institute, University of Alberta. The splicing factor ASF was tagged with a fluorescent protein (GFP), and a band of width 3 μm was photobleached across the nucleus of a living cell. As time elapses, the photobleached region recovers its fluorescence.

ment of proteins in cells is called FRAP (Fluorescence Recovery After Photobleaching). FRAP is an experimental technique used to measure the mobility of fluorescently tagged molecules [1, 8, 45, 57, 99, 111, 112]. The underlying principle in a FRAP experiment is that biomolecules are coupled to a fluorescent tag and can be visualized and monitored over space and time using fluorescence microscopy. Under typical experimental conditions, the concentration of fluorescent biomolecules is at steady state before photobleaching. To study the kinetic behaviour of this population of fluorescent molecules, a specific region within the sample is *photobleached*, i.e., it is exposed to a brief but sufficiently intense excitation pulse that irreversibly inactivates fluorescence emission. Thus, molecules outside of the photobleached region remain fluorescent whereas the molecules within the photobleached region are nonfluorescent. If the underlying steady-state distribution reflects biomolecules that are in a constant flux, the fluorescent and nonfluorescent pools will mix over time until a new steady state of fluorescent biomolecules is achieved. The time required to reach this steady state is a reflection of the rate at which fluorescently tagged molecules normally move. To measure this mobility, the fluorescence intensity in the photobleached region is recorded over time by collecting images of the fluorescently labelled sample until equilibrium is reached (figure 1.1). The resulting

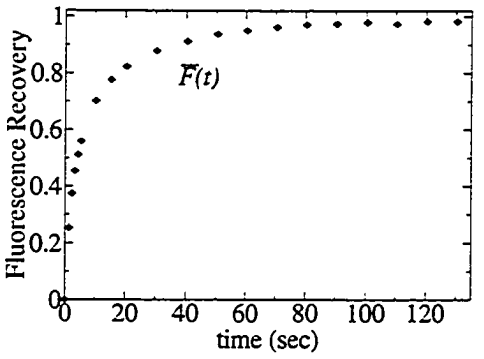

Figure 1.2: Fluorescence intensity recovery of type H1 histone after photobleaching a band of width 1.5 μm across the nucleus of a SK-N-SH human neuroblastoma cell. The FRAP data were obtained at Dr. Hendzel's lab at the Cross Cancer Institute, University of Alberta.

fluorescence recovery data are used to plot a normalized fluorescence recovery curve of the fluoresce intensity versus time (figure 1.2).

FRAP was developed during the 1970s for studying molecular diffusion [1, 22, 56, 90, 95], but its application to the study of proteins in living cells is more recent and driven largely by the identification and development of fluorescent proteins that can be used as cotranslational tags for proteins of interest [36, 43, 45, 57, 94, 106, 109, 110], that is, a protein under investigation can be targeted or tagged with a fluorescent tag by fusing the gene encoding the fluorescent tag protein with the gene encoding the endogenous protein. A successful tagging results in a fluorescent fusion protein whose function remains the same as that of the host protein. In particular, the use of Green Fluorescent Protein (GFP) from the jellyfish *Aequorea victoria* as a cotranslational tag has been crucial for visualizing and monitoring the localization of proteins in living cells [11, 58, 64, 92, 102, 115], and has made the use of FRAP experiments a powerful tool to study the mobility of nuclear proteins [12, 24, 40, 46, 63, 82, 87, 96].

Phair and Misteli [87] were the first ones to use FRAP experiments to demonstrate the fact that the movement of nuclear proteins can occur by diffusion [63, 83, 85]. They provide estimates of diffusion coefficients of nucleoplasmic GFP fusion proteins involved in the process of DNA transcription and RNA splicing (for

example, GFP fused to HMG-17, pre-mRNA splicing factor SF2/ASF, and rRNA processing protein fibrillarin). They found that nuclear proteins migrate about 50 to 100-fold slower than predicted based on their molecular weight and on the diffusion of inert molecules (e.g., green fluorescent protein) in the nucleoplasm [46, 87]. This reduced mobility, together with the fact that the spatial distribution pattern of the fluorescently tagged proteins was not always homogeneous but rather heterogeneous (for example, the distribution of GFP-SF2/ASF) supported the idea that these nuclear proteins were interacting with other nuclear components or structures, and that diffusion coefficients were a measure of the overall protein mobility.

In order to estimate the diffusion coefficients, Phair and Misteli [87] used the techniques developed by Axelrod *et al.* [1]; that is, to estimate an effective diffusion coefficient by fitting the solution of the diffusion equation on an infinite domain to the FRAP data. This point of intersection between nuclear protein dynamics and mathematics in the context of FRAP experiments is the point of origin for this research project, from which the following interesting questions arise:

1. How is the diffusion equation related to the analysis of FRAP data?

2. Does the approximation that diffusion occurs on an infinite domain lead to sufficiently accurate estimates of diffusion coefficients when in reality the nucleus is bounded by a membrane?

3. Are the fluorescently tagged proteins merely diffusing or are they undergoing molecular interactions?

4. How can we incorporate simple protein interactions in the analysis of FRAP data?

5. Is it possible to explain the heterogeneous spatial distribution of some nuclear proteins?

The main objective of this thesis is to address the aforementioned questions through mathematical modelling. These questions can be divided into two types according to the problem they address: (i) mobility, and (ii) pattern formation.

The first four questions are of mobility type, and the last question is of pattern-formation type. The thesis is divided into five main chapters, each one of which starts with a brief introduction and ends with a discussion. Chapter 2 deals with mobility questions 1 and 2, chapters 3-5 deal with mobility questions 3 and 4, and chapter 6 deals with pattern-formation question 5.

Chapter 2 offers a brief review of FRAP experiments and an exposition of how the diffusion equation is incorporated in the analysis of experimental FRAP data. We also address the issue of neglecting the nuclear membrane in the analysis, i.e., of estimating effective diffusion coefficients using the diffusion equation on an infinite domain. This method gives satisfactory results provided the photobleached area is small relative to the size of the domain and away from the nuclear membrane. We discuss the influence of the membrane and the location of the photobleaching on the estimation of diffusion coefficients for diffusing biomolecules in a bounded domain, and show that overestimations or underestimations can result from ignoring the membrane. We provide a simple methodology to estimate effective diffusion coefficients of nuclear proteins when the nuclear membrane is taken into consideration, and apply it to estimate the overall mobility of two nuclear proteins, histone H1 and nuclear actin.

However, fitting the diffusion equation to the experimental data might not be satisfactory. The reason for this is that most functional nuclear proteins undergo interactions with subcellular structures, affecting the recovery of fluorescence. In particular, FRAP experiments have shown that nuclear proteins can move about 50 to 100-fold slower than predicted based on their molecular weight [46, 87]. This reduced mobility is a direct consequence of binding interactions with macromolecules or structures, such as chromatin or interchromatin domains within the nucleoplasm, which are sufficiently large that they do not diffuse significant distances on the time-scale of the FRAP experiment [10, 36, 51, 69, 100]. During FRAP experiments, fluorescent biomolecules undergoing binding events redistribute into the photobleached region by first dissociating from their binding sites outside of the photobleached region and then, through a random walk, eventually encountering a

binding site within the photobleached region. As a result, reversible association is the rate-limiting step in the recovery of fluorescence. Therefore, it would be meaningful and biologically informative to incorporate these binding interactions into mathematical models that can be used to fit the experimental data.

In chapter 3, we consider a well-known linear reaction-diffusion equation to describe the dynamics of diffusive fluorescent proteins in the cell nucleus undergoing a reversible binding-unbinding process with an approximate spatially homogeneous structure that is considered immobile on the time scale of molecular movement. For example, chromatin-associated proteins interact with interphase chromatin that approaches a homogeneous distribution in human cell lines and is immobile on the time scale of a typical FRAP experiment. The reaction-diffusion model can be used to analyze FRAP data and quantify these molecular interactions. On the basis of the solution of the model, we derive an explicit theoretical recovery curve that can be used to fit experimental FRAP data and estimate the kinetic parameters that describe reversible binding interactions, namely the binding (association) and unbinding (dissociation) rates. These parameters can be used to infer biologically meaningful information of the protein dynamics, such as the protein residence time in a bound state, the average time between binding events, the proportion of the protein population that is bound, and the proportion that is free to diffuse.

Of particular interest is the application of the reaction-diffusion model presented in chapter 3 to quantify the spatio-temporal dynamics of histone H1 and nuclear actin. We describe the dynamics of these proteins and confirm that the model assumptions are met. By interpreting FRAP data of these proteins with the reaction-diffusion model, we conclude that the data can be explained satisfactorily when the protein interactions are taken into consideration. Specifically, the interpretation of FRAP data for histone H1 leads to the hypothesis that another subpopulation of the protein should be considered, namely a subpopulation weakly bound to the chromatin structure. This hypothesis is consistent with the experimental evidence of a rapid exchange of histone H1 on chromatin [51]. Further, the interpretation of FRAP data for nuclear actin supports recent evidence that actin is present in the

nucleus in polymeric form [61].

We notice that the relevant biological information determined in chapter 3 (the protein residence time in a bound state, the wandering time between binding events, the proportion of the protein population that is bound, and the proportion that is free to diffuse) can be obtained from the time-dependent parameters representing the binding and unbinding rates, and does not make any use of spatial information. This, together with the fact that FRAP data are presented as a space-independent function, give rise to the following question: Can we simplify the task of parameter estimation by developing a new approach for analyzing FRAP data of nuclear proteins undergoing binding events in which time represents the only independent variable?

Motivated by this question, we introduce in chapter 4 a new approach for analyzing experimental FRAP data of nuclear proteins undergoing a reversible binding interaction. Specifically, we propose a compartmental model that consists of a system of ordinary differential equations, where the only independent variable is time. The model is based on the fact that photobleaching the cell nucleus creates bleached and unbleached compartments, where the dynamics of the fluorescent proteins can be monitored. The kinetic parameters of the model are the binding and unbinding rates, and a new parameter, called the diffusional transfer coefficient, that describes the flux of fluorescent proteins in and out of the compartments. By solving the model explicitly, we derive a theoretical recovery curve that can be used to fit FRAP data and estimate binding and unbinding rates, which in turn allows us to extract the relevant biological information. The model allows for a significant simplification in the task of parameter estimation. Specifically, the resulting theoretical recovery curve is given by a simple sum of two exponential terms. We present a parameter estimation methodology, and apply it to estimate the proportions of the polymeric and monomeric pools of actin within the nucleus [61]. The results are consistent with the estimates obtained using the reaction-diffusion model in chapter 3.

The apparent tradeoff for the simplicity of the theoretical recovery curve obtained from the compartmental model is that it does not offer a straightforward estimate

of a diffusion coefficient, but instead it provides an estimate of a new parameter, the diffusional transfer coefficient. Therefore, the following new question arises: Is the diffusional transfer coefficient related to the diffusion coefficient? In other words, what is the relationship between the reaction-diffusion model presented in chapter 3 and the compartmental model developed in chapter 4?

We address this question in chapter 5. Specifically, we relate the diffusional transfer coefficient to the diffusion coefficient by applying the concepts of *residence time*, *transit time* [31, 32], and *mean time to capture* [3]. The resulting relation provides a simplified method for estimating the diffusion coefficient. The method is applied to estimate the diffusion coefficient of nuclear actin. The estimate is consistent with the one obtained in chapter 3 using the reaction-diffusion model.

The other main issue addressed in chapter 5 is related to the behaviour of FRAP data presented in both chapter 3 and chapter 4. In particular, we note that the behaviour of FRAP data for histone H1 differs greatly for that of nuclear actin: the FRAP data for histone H1 is characterized by a slow and gradual recovery, whereas the FRAP data for nuclear actin exhibits a biphasic behaviour, with a fast initial recovery followed by a slow final recovery. The natural questions that arise are the following: Can we explain the origin of these types of behaviour mathematically? Can we take advantage of these particular features to employ simpler theoretical recovery curves to fit the data?

Motivated by these questions, we offer in chapter 5 a characterization of the fluorescence recovery curves for nuclear proteins whose dynamics can be described by the reaction-diffusion model presented in chapter 3 or the compartmental model developed in chapter 4. Specifically, we use perturbation analysis to provide a formal mathematical explanation of two limiting dynamical types of behaviour exhibited by FRAP data, namely (i) a reduced diffusive behaviour, in which the recovery curve looks like the one produced by a single slower diffusing population, and (ii) a biphasic recovery, distinguished by a fast phase and a slow phase. We identify successfully the FRAP data for histone H1 as having a reduced diffusive behaviour, and the FRAP data for nuclear actin as having a biphasic behaviour. The perturbation analysis

also provides a spectrum of simple theoretical recovery curves that simplifies the task of parameter estimation.

In chapter 6, we focus our attention on the last problem in this research project: the one concerning the heterogeneity in the spatial distribution of nuclear proteins demonstrated by fluorescence microscopy images. In particular, we focus on the spatial heterogeneous distribution of splicing factors. Splicing factors are nuclear proteins that remove introns (noncoding sequences in the genes) from precursor mRNA molecules in order to form the mature mRNA. During interphase, splicing factors are concentrated in approximately 25 to 50 clusters. These aggregates of splicing factors, which are heterogeneously distributed in a "speckled" pattern in the nucleus are called Splicing Factor Compartments (SFC's) or nuclear speckles [46, 49, 87, 97, 98]. The natural question that arises is the following: What causes the compartmentalization of splicing factors? The objective of chapter 6 is to address this question using mathematical modelling. In the chapter, we review the most recent findings on the dynamical nature of splicing factors, and based on current biological hypotheses for their self-organization, we propose a fourth-order aggregation-diffusion model that describes a possible mechanism for the formation of splicing factor compartments. The model incorporates two hypotheses, namely (1) that self-organization of dephosphorylated splicing factors, modulated by a phosphorylation-dephosphorylation cycle, is responsible for the formation and disappearance of speckles, and (2) that an underlying nuclear structure plays a major role in the organization of splicing factors. A linear stability analysis about homogeneous steady-state solutions of the model reveals how the self-interaction among dephosphorylated splicing factors can result in the onset of spatial patterns. A detailed bifurcation analysis of the model describes how phosphorylation and dephosphorylation modulate the onset of the compartmentalization of splicing factors, and allows us to to delimit regions of stability and instability.

Finally, we summarize the main results of the thesis and discuss the direction of future work in chapter 7.

Chapter 2

Analysis of FRAP Data with the Diffusion Equation

Fluorescence Recovery After Photobleaching (FRAP) is an experimental technique used to measure the mobility of proteins within the cell nucleus. After proteins of interest are fluorescently tagged for their visualization and monitoring, a small region of the nucleus is photobleached. The experimental FRAP data are obtained by recording the recovery of the fluorescence in this region over time. The curve obtained by plotting the data is referred to as the *fluorescence recovery curve*, or *FRAP curve*, or simply *FRAP data*. An example of a fluorescence recovery curve is shown in figure 1.2.

The fluorescence recovery data recorded, say at times t_j, with $1 \leq j \leq n$, can be presented in two forms: normalized with respect to the fluorescence intensity in the bleached region before photobleaching,

$$F^*(t_j)\ ; \tag{2.1}$$

or normalized with respect to the expected final fluorescence intensity in the bleached region after recovery,

$$\overline{F}(t_j)\ . \tag{2.2}$$

Assuming that the entire population of biomolecules is mobile, the difference be-

tween these normalizations is that in the first case the proportion of the fluorescence intensity lost due to photobleaching is exhibited in the recovery, and therefore, the normalized data will not reach unity, i.e., $F^*(t_n) < 1$, whereas in the second case this loss is not exhibited in the recovery, and consequently, $\overline{F}(t_n) \approx 1$. The importance of this difference will become apparent later. The data shown in figure 1.2 are normalized in form (2.2).

Depending on the purpose of the experiment, FRAP data can be analyzed differently. A simple measurement such as the half-time of fluorescence recovery may be sufficient to describe the protein behaviour, but in general, mathematical modelling is required to describe the mobility of proteins and estimate kinetic parameters by fitting theoretical fluorescence recovery curves to the experimental FRAP curves. The most commonly used approach is based on the assumption that the spatio-temporal dynamics of the proteins is diffusive in nature. Under this assumption, the kinetic parameter that measures the rate of movement is the diffusion coefficient, which reflects the mean squared displacement of the proteins through a random walk over time. Because the diffusion equation does not take into consideration any kind of interaction that nuclear proteins might be undergoing, the measurement obtained has been more appropriately termed *effective* or *apparent* diffusion coefficient [58, 67, 95].

In this chapter, we will concentrate on the analysis of FRAP data for nuclear proteins using the diffusion equation. The diffusion equation was studied in the context of FRAP data by Axelrod et al. [1]. Their work assumes that biomolecules diffuse on a two-dimensional infinite domain, where the photobleached region is a circular area, and the results have been applied recently to estimate effective diffusion coefficients of nuclear proteins [87]. However, the cell nucleus is a finite region bounded by a membrane, and therefore it is biologically reasonable to consider a bounded domain in the analysis. Thus, on the basis of the work in [1], section 2.1 aims at presenting an exposition of how the diffusion equation, on both bounded and unbounded domains, is used in the analysis of FRAP data for nuclear proteins. The treatment of the diffusion equation using circular photobleached regions

on infinite or circular domains requires a radially symmetric initial condition and a solution depending only on the radial variable. This does not allow us to study the influence of the location of the photobleaching on the fluorescence recovery. For this reason, we have chosen rectangular photobleached regions on infinite or rectangular domains for the analysis of FRAP data. This will allow us to compare the behaviour of fluorescence recovery curves on bounded and unbounded domains, to assess the influence of the nuclear membrane and the location of the photobleached region on the fluorescence recovery, and to reduce the problem to a one-dimensional spatial domain. By solving the diffusion equation explicitly, we will be able to derive theoretical recovery curves that can be used to interpret FRAP data and estimate effective diffusion coefficients. In section 2.2, we shall see how the incorporation of a nuclear membrane into the analysis provides an explanation for the experimental differences in the fluorescence recovery curves that are observed depending on the size and the location of the photobleached region. In section 2.3, we shall discuss how the oversight of a nuclear membrane can lead to erroneous estimations of effective diffusion coefficients. In this section, we will also provide a very simple methodology for estimating effective diffusion coefficients for nuclear proteins using FRAP experiments. The methodology will be applied to experimental FRAP data of two nuclear proteins, histone H1 and nuclear actin, in order to quantify their overall mobility in the cell nucleus. The chapter concludes with a discussion in section 2.4.

2.1 Obtaining Theoretical Recovery Curves from The Diffusion Equation

When performing FRAP experiments to determine the overall mobility of nuclear proteins, the cell nuclei are considered to be flat domains, due to the typical experimental set-up in which the cell is flattened. Thus, the spatial domain of the problem has two dimensions. The kinetic process responsible for the movement of fluorescent biomolecules after photobleaching is assumed to be diffusion, described

by the diffusion equation,

$$\begin{aligned} &\frac{\partial}{\partial t}u(x,y;t) = D\,\Delta u(x,y;t)\,, \qquad t>0\,, \\ &u(x,y;0) = f(x,y)\,, \end{aligned} \tag{2.3}$$

where $u(x,y;t)$ represents the concentration of the fluorescent (unbleached) protein after photobleaching at position (x,y) at time t, $\Delta = \frac{\partial^2}{\partial x^2} + \frac{\partial^2}{\partial y^2}$ denotes the Laplacian operator, D is the effective diffusion coefficient, and the initial condition $f(x,y)$ represents the distribution of fluorescent (unbleached) proteins right after photobleaching.

Thus, under the assumption that the tagged fluorescent proteins are moving randomly according to the diffusion equation (2.3), the photobleached region will recover fluorescence at a rate dictated by the effective diffusion coefficient D. Therefore, the main task is to estimate this parameter, which will be a quantitative measurement of the overall mobility of the protein under investigation. To do so, it is necessary to solve the diffusion equation in order to obtain a theoretical fluorescence recovery curve that can be used to fit the FRAP data.

In this section, we will present an exposition of how the diffusion equation (2.3) is used in the analysis of FRAP data. The results are based on the work by Axelrod et al. [1], who assume that biomolecules diffuse on an infinite domain. Since our focus is on the dynamics of nuclear proteins that are confined to a bounded domain, namely the cell nucleus, we will extend the results by also considering bounded domains.

As a first step to obtaining a theoretical fluorescence recovery curve, we determine the initial condition $f(x,y)$ in (2.3). For simplicity, we will assume not only that photobleaching is performed on a cell nucleus that has reached a steady-state distribution of fluorescent proteins, but also that the intensity of the laser beam used to photobleach a region is set up with the following rectangular intensity profile

$$I(x,y) = \begin{cases} \dfrac{P}{4\,h_1\,h_2}\,, & |x-c_1| \le h_1\,,\ |y-c_2| \le h_2\,, \\ 0\,, & y-c_2 > |h_2|\,, \\ 0\,, & x-c_1 > |h_1|\,, \end{cases} \tag{2.4}$$

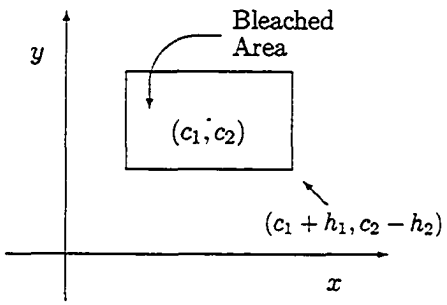

Figure 2.1: Photobleached region in two dimensions.

where P is the laser power, $2h_1$ and $2h_2$ are the dimensions of the area being photobleached, and $c = (c_1, c_2)$ is the center of the photobleaching (see figure 2.1).

The great advantage of this profile is that it provides a simple initial condition for the partial differential equation (2.3). Assuming, as in [1], that the photobleaching is a simple irreversible linear reaction described by the ordinary differential equation

$$\frac{du}{dt} = -\alpha I u \,, \tag{2.5}$$

where $-\alpha I$ denotes the constant rate of the reaction, and that a short laser beam pulse lasts a time T, then the initial condition f for the unbleached population of the protein is given by

$$u(x, y; 0) = f(x, y) = u_0 \exp\left(-\alpha I(x, y) T\right), \tag{2.6}$$

where u_0 is the initial uniform steady state of the fusion protein before photobleaching. Due to the exponential term in (2.6), if the laser power P is sufficiently large, the initial condition for (2.3) can be approximated as follows:

$$u(x, y, 0) = f(x, y) = \begin{cases} 0 \,, & |x - c_1| \le h_1 \,,\ |y - c_2| \le h_2 \,, \\ u_0 \,, & |y - c_2| > h_2 \,, \\ u_0 \,, & |x - c_1| > h_1 \,. \end{cases} \tag{2.7}$$

To solve the initial value problem (2.3), it still remains to introduce a spatial domain. The approach that has been used to study diffusion processes in the cell nucleus monitored by photobleaching technique assumes an infinite domain [1, 87].

We will review this approach in section 2.1.3. However, the cell nucleus is a finite region bounded by a membrane. We will treat this case of bounded domains in sections 2.1.1 and 2.1.2. We summarize the resulting theoretical fluorescence recovery curves for both bounded and unbounded domains in section 2.1.4. The consequences of considering an unbounded versus a bounded domain when estimating effective diffusion coefficients will be discussed in the remainder of this chapter.

2.1.1 Explicit Solution on a Bounded Domain

Denoting the cell nucleus as Ω, approximating its shape with a rectangle

$$\Omega = \{(x,y) \in \mathbb{R}^2 ;\, 0 < x < a\,,\; 0 < y < b\}\,,$$

and assuming that there is no flux of fluorescent biomolecules into or out of it on the time scale of a FRAP experiment, the diffusion equation (2.3) becomes an initial boundary-value problem subject to Neumann (no-flux) boundary conditions:

$$\begin{aligned}
&\frac{\partial}{\partial t}u(x,y;t) = D\,\Delta u(x,y;t)\,, && (x,y) \in \Omega\,,\;\; t>0\,,\\
&\frac{\partial}{\partial x}u(x,y;t) = 0\,, && (x,y) \in \partial\Omega_1\,,\;\; t>0\,,\\
&\frac{\partial}{\partial y}u(x,y;t) = 0\,, && (x,y) \in \partial\Omega_2\,,\;\; t>0\,,\\
&u(x,y;0) = f(x,y)\,; && (x,y) \in \Omega\,.
\end{aligned} \tag{2.8}$$

where

$$\partial\Omega_1 = \{(x,y) \in \mathbb{R}^2 ;\; x = 0, a\,,\quad 0 \le y \le b\,\}\,,$$

$$\partial\Omega_2 = \{(x,y) \in \mathbb{R}^2 ;\; y = 0, b\,,\quad 0 \le x \le a\,\}\,.$$

To solve (2.8) explicitly, we use the method of separation of variables. So, letting $u(x,y;t) = X(x)Y(y)T(t)$, and substituting this into (2.8), the following eigenvalue problem is obtained:

$$X'' = -\lambda X \quad,\quad X'(0) = X'(a) = 0\,, \tag{2.9}$$

$$Y'' = -\mu Y \quad,\quad Y'(0) = Y'(b) = 0\,, \tag{2.10}$$

$$T' = -(\lambda+\mu)D\,T\,. \tag{2.11}$$

From (2.9), we obtain the eigenvalues $\lambda_n = \left(\frac{n\pi}{a}\right)^2$, $n = 0, 1, 2, \ldots$, corresponding to the normalized eigenvectors

$$\begin{aligned} X_0 &= \frac{1}{\sqrt{a}}, \\ X_n &= \sqrt{\frac{2}{a}} \cos\left(\frac{n\pi x}{a}\right) , \; n = 1, 2, \ldots \quad . \end{aligned}$$

From (2.10), we obtain the eigenvalues $\mu_m = \left(\frac{m\pi}{b}\right)^2$, $m = 0, 1, 2, \ldots$, corresponding to the normalized eigenvectors

$$\begin{aligned} Y_0 &= \frac{1}{\sqrt{b}}, \\ Y_m &= \sqrt{\frac{2}{b}} \cos\left(\frac{m\pi y}{b}\right) , \; m = 1, 2, \ldots \quad . \end{aligned}$$

Thus, using the principle of superposition, the solution of the initial boundary-value problem (2.8) is given by

(2.12)

$$\begin{aligned} u(x,y,t) &= \frac{1}{\sqrt{ab}} A_{00} + \\ &\sqrt{\frac{2}{ab}} \sum_{n=1}^{\infty} A_{0n}\, e^{-(\frac{n\pi}{a})^2 Dt} \cos\left(\frac{n\pi x}{a}\right) + \\ &\sqrt{\frac{2}{ab}} \sum_{m=1}^{\infty} A_{m0}\, e^{-(\frac{m\pi}{b})^2 Dt} \cos\left(\frac{m\pi y}{b}\right) + \\ &\frac{2}{\sqrt{ab}} \sum_{n,m=1}^{\infty} A_{mn}\, e^{-\pi^2\left(\frac{n^2}{a^2}+\frac{m^2}{b^2}\right) Dt} \cos\left(\frac{n\pi x}{a}\right) \cos\left(\frac{m\pi y}{b}\right) , \end{aligned}$$

where the Fourier coefficients are given by

$$\begin{aligned} A_{00} &= \frac{1}{\sqrt{ab}} \int_0^a \int_0^b f(x,y)\, dy\, dx \\ &= \frac{u_0}{\sqrt{ab}} (ab - 4h_1 h_2) , \end{aligned}$$

$$A_{0n} = \sqrt{\frac{2}{ab}} \int_0^a \int_0^b f(x,y) \cos\left(\frac{n\pi x}{a}\right) dy\, dx$$

$$= 2h_2 u_0\, a \sqrt{\frac{2}{ab}}\, S_n(c_1, h_1, a)\,, \quad n \geq 1\,,$$

$$A_{m0} = \sqrt{\frac{2}{ab}} \int_0^a \int_0^b f(x,y) \cos\left(\frac{n\pi y}{b}\right) dy\, dx$$

$$= 2h_1 u_0\, b \sqrt{\frac{2}{ab}}\, S_m(c_2, h_2, b)\,, \quad m \geq 1\,,$$

$$A_{mn} = \frac{2}{\sqrt{ab}} \int_0^a \int_0^b f(x,y) \cos\left(\frac{n\pi y}{b}\right) \cos\left(\frac{n\pi x}{a}\right) dy\, dx$$

$$= -\frac{2u_0\, a\, b}{\sqrt{ab}} S_m(c_2, h_2, b)\, S_n(c_1, h_1, a)\,, \quad m, n \geq 1\,,$$

and

$$S_k(c,h,l) = \frac{1}{k\pi}\left[\sin\left(\frac{k\pi(c-h)}{l}\right) - \sin\left(\frac{k\pi(c+h)}{l}\right)\right]\,. \tag{2.13}$$

2.1.2 Reducing the Dimension Using a Band Photobleaching Profile

When studying the mobility of biomolecules in living cells using FRAP experiments, a very common photobleaching profile is a narrow band [10, 62, 100, 101, 110]. In this case, it suffices to consider a one-dimensional problem, as follows. If we approximate the shape of the cell nucleus with a rectangle and assume that the profile of the photobleaching is a narrow band of width $2h$, centered on the x-axis at c (figure 2.2), the initial boundary-value problem (2.8) is reduced to the one-dimensional

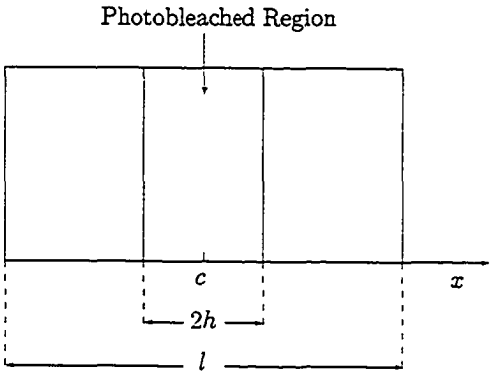

Figure 2.2: The shape of the cell nucleus is approximated with a rectangle of length l, and the profile of the photobleaching is a narrow band of width $2h$, centered on the x axis at c.

problem

$$
\begin{aligned}
&\frac{\partial}{\partial t}u(x,t) = D\frac{\partial^2}{\partial x^2}u(x,t)\,, \qquad x \in (0,l)\,,\ t>0\,,\\
&\frac{\partial u}{\partial x} = 0\,, \qquad x = 0,l\,,\ t>0\,,\\
&u(x,0) = f(x)\,, \qquad x \in (0,l)\,,
\end{aligned}
\tag{2.14}
$$

where the initial condition is given by

$$
f(x) = \begin{cases} 0\,, & |x-c| \le h\,,\\ u_0\,, & |x-c| > h\,. \end{cases}
\tag{2.15}
$$

Note that we have denoted the length of the rectangular domain by l (see figure 2.2) instead of a as was done for initial boundary-value problem (2.8).

To obtain an explicit solution of the initial boundary-value problem (2.14), we again apply the method of separation of variables. Expressing the solution as $u(x,t) = T(t)\,X(x)$, and substituting it into (2.14), we obtain the eigenvalue problem

$$T' = -\lambda DT \tag{2.16}$$

$$X'' = -\lambda X\ , \quad X'(0) = X'(l) = 0\,. \tag{2.17}$$

From (2.16), we obtain the eigenvalues $\lambda_n = \left(\frac{n\pi}{l}\right)^2$, $n = 0,1,2,\ldots$, corresponding

to the normalized eigenvectors

$$X_0 = \frac{1}{\sqrt{l}},$$
$$X_n = \sqrt{\frac{2}{l}} \cos\left(\frac{n\pi x}{l}\right), \; n = 1, 2, \ldots .$$

Thus, the solution of (2.14) is given by

(2.18)
$$\boxed{u(x,t) = \frac{A_0}{\sqrt{l}} + \sum_{n=1}^{\infty} A_n \, e^{-(\frac{n\pi}{l})^2 Dt} \sqrt{\frac{2}{l}} \cos\left(\frac{n\pi x}{l}\right),}$$

where the coefficients A_n are determined by the cosine Fourier series of the initial condition, that is

$$A_0 = \frac{1}{\sqrt{l}} \int_0^l f(x)dx = \frac{u_0}{\sqrt{l}}(l - 2h),$$

$$A_n = \sqrt{\frac{2}{l}} \int_0^l \cos\left(\frac{n\pi x}{l}\right) f(x)dx$$
$$= \sqrt{\frac{2}{l}} u_0 \frac{l}{n\pi} \left[\sin\left(\frac{n\pi(c-h)}{l}\right) - \sin\left(\frac{n\pi(c+h)}{l}\right)\right], \; n \geq 1 .$$

2.1.3 Explicit Solution on an Unbounded Domain

For an unbounded domain, the initial value problem for the diffusion equation (2.3) takes the form

(2.19)
$$\frac{\partial}{\partial t} u(\boldsymbol{x}, t) = D \, \Delta u, \quad \mathbb{R}^n \times (0, \infty),$$
$$u(\boldsymbol{x}, 0) = f(\boldsymbol{x}), \quad \mathbb{R}^n,$$

where $f(\boldsymbol{x})$ is given by (2.15) for $n = 1$ or by (2.7) for $n = 2$.

The explicit solutions for the Cauchy problem (2.19) for $n = 1$ and $n = 2$ can be obtained via Fourier transforms. We denote the Fourier transform of $u(\boldsymbol{x}, t)$ as

$$u^{\wedge}(\lambda, t) = \frac{1}{(2\pi)^{n/2}} \int_{\mathbb{R}^n} e^{-i\boldsymbol{x}\cdot\lambda} u(\boldsymbol{x}, t) \, d\boldsymbol{x}, \quad \lambda \in \mathbb{R}^n,$$

where $x \cdot \lambda$ denotes the dot product, and the inverse Fourier transform as

$$u^{\vee}(x,t) = \frac{1}{(2\pi)^{n/2}} \int_{\mathbb{R}^n} e^{i x \cdot \lambda} u(\lambda,t)\, d\lambda\,, \quad x \in \mathbb{R}^n\,.$$

Taking the Fourier transform in the x-variable of (2.19), we obtain the following ordinary differential equation for $u^{\wedge}$:

$$\begin{aligned} u_t^{\wedge}(\lambda,t) &= -D\,|\lambda|^2\, u^{\wedge}(\lambda,t)\,, \\ u^{\wedge}(\lambda,0) &= f^{\wedge}(\lambda)\,. \end{aligned} \tag{2.20}$$

The solution of (2.20) is given by

$$u^{\wedge}(\lambda,t) = f^{\wedge}(\lambda) e^{-t\,D\,|\lambda|^2} = f^{\wedge}(\lambda)((e^{-t\,D\,|\lambda|^2})^{\vee})^{\wedge}\,. \tag{2.21}$$

Now, denoting

$$F = (e^{-t\,D\,|\lambda|^2})^{\vee} = \frac{1}{(2\pi)^{n/2}} \int_{\mathbb{R}^n} e^{i x \cdot \lambda} e^{-t\,D\,|\lambda|^2}\, d\lambda = \frac{1}{(2\,D\,t)^{n/2}} e^{\frac{-|x|^2}{4\,D\,t}}\,,$$

(2.21) becomes

$$u^{\wedge}(\lambda,t) = f^{\wedge}(\lambda) F^{\wedge} = \frac{(f * F)^{\wedge}}{(2\pi)^{n/2}}\,, \tag{2.22}$$

where $*$ stands for the convolution product. Taking the inverse Fourier transform of (2.22), we obtain the solution

$$u(x,t) = \frac{1}{(4\pi\,D\,t)^{n/2}} \int_{\mathbb{R}^n} e^{-\frac{|x-\lambda|^2}{4\,D\,t}} f(\lambda)\, d\lambda\,, \tag{2.23}$$

Let us see how this solution is simplified when the initial $f(x)$ is given by (2.15) for $n = 1$ or by (2.7) for $n = 2$.

One-dimensional case

Using the initial condition (2.15), (2.23) reduces to

$$u(x,t) = \frac{u_0}{\sqrt{4\pi\,D\,t}} \int_{-\infty}^{c-h} e^{-\frac{|x-\lambda|^2}{4\,D\,t}} d\lambda + \frac{u_0}{\sqrt{4\pi\,D\,t}} \int_{c+h}^{\infty} e^{-\frac{|x-\lambda|^2}{4\,D\,t}} d\lambda\,. \tag{2.24}$$

By making the change of variable $\nu = \dfrac{x-\lambda}{\sqrt{4\,D\,t}}$ and splitting the integrals, (2.24) becomes

$$u(x,t) = \frac{u_0}{\sqrt{\pi}} \left(\int_{\frac{x-c+h}{\sqrt{4Dt}}}^{\infty} e^{-\nu^2} d\nu + \int_{-\infty}^{\frac{x-c-h}{\sqrt{4Dt}}} e^{-\nu^2} d\nu \right)\,. \tag{2.25}$$

Using the definition of the error function and the error function complement,

$$\operatorname{erf}(x) = \frac{2}{\sqrt{\pi}} \int_0^x e^{-\nu^2} d\nu, \tag{2.26}$$

$$\operatorname{erfc}(x) = 1 - \operatorname{erf}(x) = \frac{2}{\sqrt{\pi}} \int_x^\infty e^{-\nu^2} d\nu\,, \tag{2.27}$$

(see [16], page 14), we thus obtain that the solution to the diffusion equation (2.19) in a one-dimensional space with initial condition (2.15) is given by

$$\boxed{u(x,t) = \frac{u_0}{2}\left[\operatorname{erfc}\left(\frac{h+x-c}{\sqrt{4Dt}}\right) + \operatorname{erfc}\left(\frac{h-x+c}{\sqrt{4Dt}}\right)\right].} \tag{2.28}$$

Two-dimensional case

Let $\lambda = (s,\eta) \in \mathbb{R}^2$. Substituting the initial condition (2.7) into (2.23) with $n = 2$ we then obtain that

$$\begin{aligned} u(x,y,t) = \frac{u_0}{4\pi D t}\Bigg(& \int_{-\infty}^{c_1-h_1}\int_{-\infty}^{\infty} e^{-\frac{(x-s)^2+(y-\eta)^2}{4Dt}} d\eta\, ds + \\ & \int_{c_1+h_1}^{\infty}\int_{-\infty}^{\infty} e^{-\frac{(x-s)^2+(y-\eta)^2}{4Dt}} d\eta\, ds + \\ & \int_{c_1-h_1}^{c_1+h_1}\int_{-\infty}^{c_-h_2} e^{-\frac{(x-s)^2+(y-\eta)^2}{4Dt}} d\eta\, ds + \\ & \int_{c_1-h_1}^{c_1+h_1}\int_{c_2+h_2}^{\infty} e^{-\frac{(x-s)^2+(y-\eta)^2}{4Dt}} d\eta\, ds\Bigg)\,. \end{aligned} \tag{2.29}$$

This last expression can be rewritten as

$$
\begin{aligned}
u(x,y,t) = \frac{u_0}{4\pi D t}\int_{-\infty}^{\infty} e^{-\frac{(y-\eta)^2}{4Dt}} d\eta \times \\
\left(\int_{-\infty}^{c_1-h_1} e^{-\frac{(x-s)^2}{4Dt}} ds + \int_{c_1+h_1}^{\infty} e^{-\frac{(x-s)^2}{4Dt}} ds\right) + \\
\frac{u_0}{4\pi D t}\int_{c_1-h_1}^{c_1+h_1} e^{-\frac{(x-s)^2}{4Dt}} ds \times \\
\left(\int_{-\infty}^{c_2-h_2} e^{-\frac{(y-\eta)^2}{4Dt}} d\eta + \int_{c_2+h_2}^{\infty} e^{-\frac{(y-\eta)^2}{4Dt}} d\eta\right) .
\end{aligned}
\tag{2.30}
$$

Therefore, using the definition of the error function (2.26) and the error function complement (2.27), the solution to the diffusion equation (2.19) in a two-dimensional space with initial condition (2.7) is given by

$$
\boxed{u(x,y,t) = \frac{u_0}{2} g_{erc}(x,t,h_1,c_1) + \frac{u_0}{4} g_{er}(x,t,h_1,c_1)\, g_{erc}(y,t,h_2,c_2)\ ,}
\tag{2.31}
$$

where

$$
g_{erc}(z,t,h,c) = \left[\operatorname{erfc}\left(\frac{h+z-c}{\sqrt{4Dt}}\right) + \operatorname{erfc}\left(\frac{h-z+c}{\sqrt{4Dt}}\right)\right] ,
\tag{2.32}
$$

$$
g_{er}(z,t,h,c) = \left[\operatorname{erf}\left(\frac{h+z-c}{\sqrt{4Dt}}\right) + \operatorname{erf}\left(\frac{h-z+c}{\sqrt{4Dt}}\right)\right] .
\tag{2.33}
$$

2.1.4 Theoretical Fluorescence Recovery Curves

Having obtained the solution of the diffusion equation on both bounded and unbounded domains, we are now in a position to obtain theoretical fluorescence recovery curves that can be used to interpret the experimental FRAP data. To do so, it is assumed that the fluorescence intensity recorded in time in the photobleached region is proportional to the fluorescent population size in the region. Thus, the experimental FRAP curve is expected to be proportional to the following theoretical

recovery curve

$$R(t) = \int_{\Lambda} u(\boldsymbol{x}, t) d\boldsymbol{x} \,, \tag{2.34}$$

where Λ represents the photobleached region, and $u(\boldsymbol{x}, t)$ denotes the solution of the initial value problem (2.3). We normalize the recovery (2.34) with respect to the total population of fluorescent biomolecules in the photobleached region (before photobleaching), and obtain theoretical fluorescence recovery curves on bounded and unbounded domains that can be used to interpret and fit FRAP data.

Bounded Domains

When approximating the shape of the cell nucleus with a rectangle, and setting a photobleaching profile as in (2.4), we simply integrate the solution (2.12) of the initial boundary-value problem (2.8) over $\Lambda = [c_1 - h_1, c_1 + h_1] \times [c_2 - h_2, c_2 + h_2]$, and divide this result by the total population of fluorescent biomolecules in the photobleached region (before photobleaching), $4u_0 h_1 h_2$, to obtain the following theoretical fluorescence recovery curve:

$$\begin{aligned} F_{B2}(t) = {} & \frac{ab - 4h_1h_2}{ab} - \\ & \sum_{n=1}^{\infty} \frac{4h_2 a}{b h_1} e^{-(\frac{n\pi}{a})^2 Dt} S_n^2(c_1, h_1, a) - \\ & \sum_{m=1}^{\infty} \frac{2h_1 b}{a h_2} e^{-(\frac{m\pi}{b})^2 Dt} S_m^2(c_2, h_2, b) - \\ & \sum_{m,n=1}^{\infty} \frac{ab}{h_1 h_2} e^{-\pi^2 \left(\frac{n^2}{a^2} + \frac{m^2}{b^2}\right) Dt} S_m^2(c_2, h_2, b)\, S_n^2(c_1, h_1, a) \,. \end{aligned} \tag{2.35}$$

In a similar way, when the photobleaching profile is a band and the problem reduces to one dimension, the following theoretical fluorescence recovery curve is obtained:

$$F_B(t) = \frac{l - 2h}{l} - \frac{l}{h} \sum_{n=1}^{\infty} e^{-(\frac{n\pi}{l})^2 Dt} S_n^2(c, h, l) \,. \tag{2.36}$$

Unbounded Domains

By going through the same integration and normalization procedure with solutions (2.28) and (2.31) of the Cauchy problem (2.19) in one and two dimensions, respectively, one obtains the theoretical fluorescence recovery curve

$$F_U(t) = \frac{1}{4h}\int_{c-h}^{c+h}\left[\operatorname{erfc}\left(\frac{h+x-c}{\sqrt{4Dt}}\right)+\operatorname{erfc}\left(\frac{h-x+c}{\sqrt{4Dt}}\right)\right]dx\,, \tag{2.37}$$

for the one-dimensional case, and the theoretical fluorescence recovery curve

$$\begin{aligned} F_{U2}(t) &= \frac{1}{4h_1}\int_{c_1-h_1}^{c_1+h_1} g_{erc}(x,t,h_1,c_1)dx + \\ &\frac{1}{16h_1h_2}\int_{c_1-h_1}^{c_1+h_1} g_{er}(x,t,h_1,c_1)dx\int_{c_2-h_2}^{c_2+h_2} g_{erc}(y,t,h_2,c_2)dy\,. \end{aligned} \tag{2.38}$$

for the two-dimensional case.

There is an immediate, yet very important, distinction between the theoretical fluorescence recovery curve coming from the diffusion equation on an unbounded domain and that coming from the diffusion equation on a bounded domain. On an unbounded domain, the fluorescence intensity after photobleaching eventually returns to its initial level, due to the fact that the supply of fluorescent proteins from the unbleached region is unlimited; on a bounded domain, there is a permanent loss of fluorescence due to photobleaching. For example, compare the fluorescence recoveries in one dimension given by (2.36) and (2.37). The asymptotic recovery level for a *bounded* domain is given by

$$\lim_{t\to\infty} F_B(t) = \frac{l-2h}{l}\,, \tag{2.39}$$

whereas the asymptotic recovery level for an *unbounded* domain is given by

$$\begin{aligned} \lim_{t\to\infty} F_U(t) &= \frac{1}{4h}\lim_{t\to\infty}\int_{c-h}^{c+h}\left[\operatorname{erfc}\left(\frac{h+x-c}{\sqrt{4Dt}}\right)+\operatorname{erfc}\left(\frac{h-x+c}{\sqrt{4Dt}}\right)\right]dx \\ &= \frac{1}{4h}\int_{c-h}^{c+h} 2\operatorname{erfc}(0)dx = 1\,, \end{aligned} \tag{2.40}$$

and therefore

$$\lim_{t\to\infty} F_B(t) = \frac{l-2h}{l} < \lim_{t\to\infty} F_U(t) = 1\,. \tag{2.41}$$

In other words, the theoretical recovery on a bounded domain accounts for the loss of fluorescence and the one on an unbounded domain does not. For this reason, and since the experimental fluorescence recovery can be presented normalized with respect to the final fluorescence intensity in the bleached region ($\overline{F}(t_j)$, for $1 \leq j \leq n$), we introduce the following normalized recovery curves for one- and two-dimensional bounded domains, respectively,

$$\overline{F}_B(t) = \frac{F_B(t)}{\lim_{t\to\infty} F_B(t)}, \qquad \overline{F}_{B2}(t) = \frac{F_{B2}(t)}{\lim_{t\to\infty} F_{B2}(t)} \tag{2.42}$$

where $F_B(t)$ is given by (2.36) and $F_{B2}(t)$ is given by (2.35). The significance of the distinction between the theoretical fluorescence recovery curves presented so far will become apparent in the next sections.

2.2 Influence of the Nuclear Membrane

In order to assess the influence of the nuclear membrane on fluorescence recovery curves, a qualitative analysis of FRAP data of diffusing CBP (Creb Binding Protein) in Indian Muntjac cells and of simulated recovery curves is carried out. The reason for choosing CBP over other proteins is that it distributes homogeneously throughout the nucleus when it is overexpressed and, thus, the experimental setup corresponds well with the theoretical assumption that the fluorescent population has reached a homogeneous steady-state distribution. Details of the experimental procedure can be found in [51]. The analysis illustrates the importance of considering the existence of the membrane in the interpretation of FRAP data and the possible shortcomings that can arise when this is overlooked. When considering the nuclear membrane, significant differences in the recovery curves will appear depending not only on the size of the photobleached area, as would be expected, but also on its location.

To illustrate qualitatively how the size of the photobleached area causes differences in the fluorescence recovery, we analyze data from three single experiments, performed at the Cross Cancer Institute, University of Alberta, by D. McDonald (unpublished data). In these experiments, circular areas, located approximately in

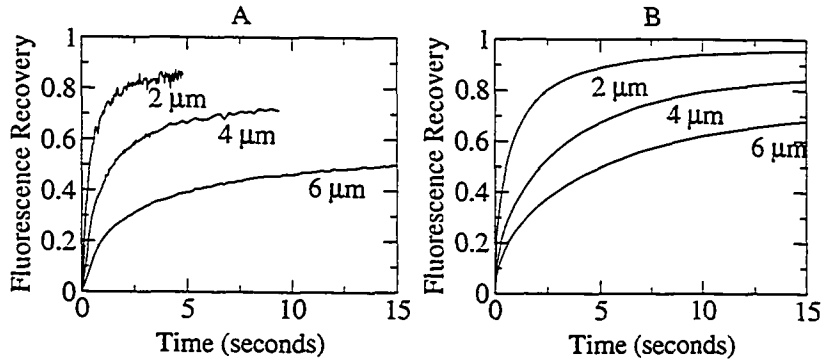

Figure 2.3: A: Recovery curves obtained from FRAP data of CBP, presented as in equation (2.1), after photobleaching circular areas of diameters 2, 4 and 6 μm in a nucleus of approximate dimensions 10 μm $\times$ 20 μm of an Indian Muntjac cell. B: Simulated fluorescence recovery curves, $F_{B2}(t)$, obtained from equation (2.35), for a population of proteins diffusing with a coefficient $D = 0.5\,\mu\text{m}^2/\text{s}$, after photobleaching square areas with side of lengths 2, 4 and 6 μm in a rectangular domain of dimensions 10 μm $\times$ 20 μm.

the center of the cell nucleus, and of diameters 2, 4 and 6 μm, were photobleached. The fluorescence recovery curves are shown in figure 2.3A. It can be seen that the asymptotic recovery levels depend on the size of the photobleached area. In particular, the larger the photobleached area, the smaller the asymptotic recovery level. The fluorescence recovery curves in figure 2.3A are qualitatively similar to the fluorescence recovery curves in figure 2.3B, $F_{B2}(t)$, obtained from equation (2.35) when simulating the photobleaching of square regions of different sizes in the center of a bounded rectangular domain. The use of square photobleached regions in the simulations aims simply at simplifying the computations and illustrating the qualitative similarity with the experimental fluorescence recovery.

In contrast, if an unbounded domain had been used in the simulations, this qualitative similarity with the experimental data would not have been exhibited, since the fluorescence recovery on an undounded domain approaches 1 as time goes to infinity.

To show how the location of the photobleaching affects the fluorescence recovery, two FRAP experiments were performed by D. McDonald at the Cross Cancer In-

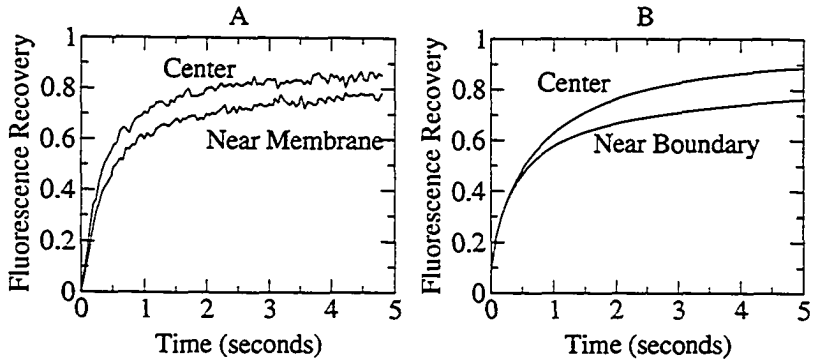

Figure 2.4: A: Recovery curves obtained from FRAP data of CBP, presented as in equation (2.1), after photobleaching a circular area of diameter $2\,\mu$m near the center and near the membrane (less than 0.5μm far to the membrane) of a cell nucleus of approximate dimensions $10\,\mu\text{m} \times 20\,\mu\text{m}$. B: Simulated fluorescence recovery curves for a population of proteins diffusing with a coefficient $D = 0.5\,\mu\text{m}^2/\text{s}$, after photobleaching a square with side of length $2\,\mu$m, in the center $(c_1, c_2) = (5, 10)$ of a rectangular domain of dimensions $10\,\mu\text{m} \times 20\,\mu\text{m}$, and near its boundary (when photobleached region is centered at $(c_1, c_2) = (8.5, 10.5)$).

stitute, University of Alberta: one in which photobleaching is done near the center of the nucleus and another one in which photobleaching is done close to the nuclear membrane. The fluorescence recovery curves are shown in figure 2.4A. We note that the rate of recovery is slower when photobleaching takes place close to the membrane. The same qualitative behaviour is exhibited in the corresponding theoretical simulations obtained from equation (2.35) when photobleaching a square region in the center of a rectangular domain and close to its boundary (figure 2.4B).

In contrast, had an unbounded domain been considered, the fluorescence recovery would have been independent of the location of the photobleached area, i.e., the fluorescence recoveries close to the boundary and in the center of the domain would have been identical. To illustrate this, consider, for example, the fluorescence recovery (2.38) on an infinite domain after photobleaching a square region centered

at $c = (c_1, c_2)$, which can be rewritten, using the expressions (2.32) and (2.33), as

$$F_{U2}(t) = \frac{1}{4h_1}\int_{c_1-h_1}^{c_1+h_1}\left[\operatorname{erfc}\left(\frac{h_1+x-c_1}{\sqrt{4Dt}}\right)+\operatorname{erfc}\left(\frac{h_1-x+c_1}{\sqrt{4Dt}}\right)\right]dx +$$

$$\frac{1}{16h_1h_2}\int_{c_1-h_1}^{c_1+h_1}\left[\operatorname{erf}\left(\frac{h_1+x-c_1}{\sqrt{4Dt}}\right)+\operatorname{erf}\left(\frac{h_1-x+c_1}{\sqrt{4Dt}}\right)\right]dx \times \tag{2.43}$$

$$\int_{c_2-h_2}^{c_2+h_2}\left[\operatorname{erfc}\left(\frac{h_2+y-c_2}{\sqrt{4Dt}}\right)+\operatorname{erfc}\left(\frac{h_2-y+c_2}{\sqrt{4Dt}}\right)\right]dy\,.$$

Introducing the changes of variables $w = x - c_1$, and $z = y - c_2$ (2.43) becomes

$$F_{U2}(t) = \frac{1}{4h_1}\int_{-h_1}^{h_1}\left[\operatorname{erfc}\left(\frac{h_1+w}{\sqrt{4Dt}}\right)+\operatorname{erfc}\left(\frac{h_1-w}{\sqrt{4Dt}}\right)\right]dw +$$

$$\frac{1}{16h_1h_2}\int_{-h_1}^{h_1}\left[\operatorname{erf}\left(\frac{h_1+w}{\sqrt{4Dt}}\right)+\operatorname{erf}\left(\frac{h_1-w}{\sqrt{4Dt}}\right)\right]dw \times \tag{2.44}$$

$$\int_{-h_2}^{h_2}\left[\operatorname{erfc}\left(\frac{h_2+z}{\sqrt{4Dt}}\right)+\operatorname{erfc}\left(\frac{h_2-z}{\sqrt{4Dt}}\right)\right]dz\,.$$

This last expression corresponds to the recovery curve when photobleaching a square region centered at $(c_1, c_2) = (0, 0)$, i.e.,

$$F_{U2}(t) = \frac{1}{4h_1}\int_{-h_1}^{h_1} g_{erc}(w,t,h_1,0)dw +$$

$$\frac{1}{16h_1h_2}\int_{-h_1}^{h_1} g_{er}(w,t,h_1,0)dw\int_{-h_2}^{h_2} g_{erc}(z,t,h_2,0)dz\,, \tag{2.45}$$

which implies that the fluorescence recovery on an infinite domain is independent of the location of the photobleached region.

2.3 Estimating Effective Diffusion Coefficients

From the considerations in the previous section, it is expected that if one assumes an infinite domain for estimating effective diffusion coefficients, erroneous estimations will arise. This issue is investigated in section 2.3.1, where the importance of considering a bounded domain to avoid underestimations or overestimations of

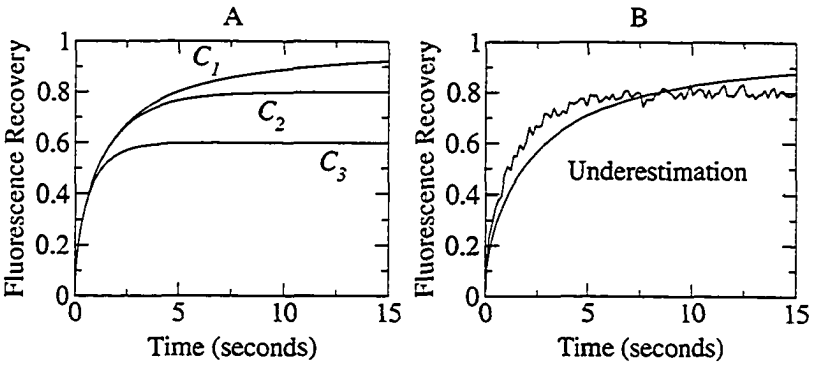

Figure 2.5: A: Fluorescence recovery curves characterized by a diffusion coefficient $D = 0.25\,\mu\text{m}^2/\text{s}$, after photobleaching a square region of area $4\,\mu\text{m}^2$ in the center of the domain. The curve C_1 represents the fluorescence recovery $F_{U2}(t)$ (equation (2.38)) on an infinite domain, and the curves C_2 and C_3 represent the fluorescence recovery $F_{B2}(t)$ (equation (2.35)) on square domains of areas $20\,\mu\text{m}^2$ and $10\,\mu\text{m}^2$, respectively. B: The fluorescence recovery curve $F_{U2}(t)$ on an infinite domain (smooth curve) is used to fit the simulated FRAP data (irregular curve) obtained from adding noise to the curve C_2. This fitting gives an underestimated diffusion coefficient $D_{est} \approx 0.15\,\mu\text{m}^2/\text{s}$.

diffusion coefficients is stressed. In section 2.3.2, we will apply the results from the present and previous sections to estimate effective diffusion coefficients of two nuclear proteins, namely histone H1 and actin.

2.3.1 Erroneous Estimations

To understand how erroneous estimations are produced, consider, for example, a fluorescent population of biomolecules moving with a diffusion coefficient $D = 0.25\,\mu\text{m}^2/\text{s}$ on an infinite domain and on square domains of sizes $20\,\mu\text{m}^2$ and $10\,\mu\text{m}^2$. If a square region of area $4\,\mu\text{m}^2$ is photobleached in the center of the domain, the theoretical fluorescence recovery curves would be as shown in figure 2.5A. The difference between the curves comes from the fact that the corresponding asymptotic recovery levels depend on the size of the domain. The larger the domain, the closer the fluorescence recovery level is to one. Thus, the recovery curve corresponding to an infinite domain lies above those corresponding to bounded domains (see figure

2.5A). Consequently, if we were to estimate a diffusion coefficient of biomolecules diffusing on a bounded domain using a recovery curve corresponding to an infinite domain, the diffusion coefficient would be *underestimated.* We show this with a numerical example. The irregular curve, shown in figure 2.5B, represents simulated FRAP data on a bounded domain presented in the form (2.1), and obtained by adding noise to the recovery curve C_2 in figure 2.5A. The simulated data are fitted with the theoretical fluorescence recovery $F_{U2}(t)$ on an infinite domain, given by equation (2.38), using the nonlinear least-squares method [4, 78], where the only unknown parameter is the diffusion coefficient. The function *nlinfit* in MATLAB is used for every nonlinear least-squares fitting in the thesis. Although the fit seems quite accurate, an *underestimated* diffusion coefficient, $D_{est} \approx 0.15\,\mu\text{m}^2/\text{s}$ is obtained, as expected from the explanation given above. Note that this underestimation can get worse if the photobleaching takes place close to the boundary, or if the size of the photobleached region is bigger.

Since the underestimation appears to be caused by the difference between the recovery levels for bounded and unbounded domains, a possible solution to this problem seems to be to normalize the recovery curves in such a way that they both approach the same recovery level; in other words, to consider the normalized recovery curve for a bounded domain given by equation (2.42). In fact, this is the procedure followed in [87]. By applying this normalization to the recovery curves in figure 2.5A, we obtain the normalized theoretical recovery curves, shown in figure 2.6A. Notice that the normalization reverses the order of the recovery curves. Thus, the normalized recovery corresponding to an unbounded domain is now below all those corresponding to bounded domains. Consequently, when the FRAP data is presented in a normalized form (2.2), and we were to estimate a diffusion coefficient of biomolecules diffusing on a bounded domain, using a recovery curve corresponding to an infinite domain, the diffusion coefficient would be *overestimated*, as shown in figure 2.6B. So, normalization transforms an underestimation problem into an overestimation problem. Of course, it is not the normalization that is the cause of erroneous estimations, rather the oversight of the nuclear membrane.

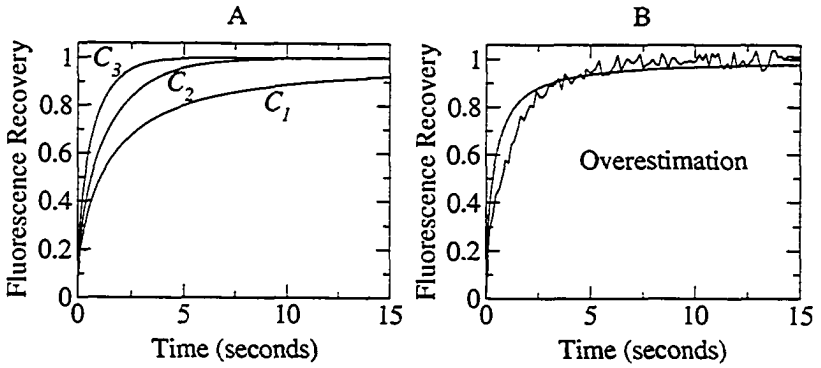

Figure 2.6: A: Normalized fluorescence recovery curves characterized by a diffusion coefficient $D = 0.25\,\mu\text{m}^2/\text{s}$, after photobleaching a square region of area $4\,\mu\text{m}^2$ in the center of the domain. The curve C_1 represents the fluorescence recovery $F_{U2}(t)$ (equation (2.38)) on an infinite domain, and the curves C_2 and C_3 represent the fluoresce recovery $\overline{F}_{B2}(t)$ (equation (2.42)) on square domains of areas $20\,\mu\text{m}^2$ and $10\,\mu\text{m}^2$, respectively. B: The fluorescence recovery curve $F_{U2}(t)$ on an infinite domain (smooth curve) is used to fit the simulated FRAP data (irregular curve) obtained from adding noise to the curve C_2. This fitting gives an overestimated diffusion coefficient $D_{est} \approx 0.93\,\mu\text{m}^2/\text{s}$.

2.3.2 Application to Nuclear Proteins

From the previous analysis, we conclude that it is necessary to consider theoretical recovery curves on a bounded domain if one wants to avoid erroneous estimations of effective diffusion coefficients of nuclear proteins. However, incorporating aspects such as the size and the geometry of the domain (the nucleus) or the size and location of the photobleaching in full detail can result in a lack of an explicit theoretical recovery curve for estimating effective diffusion coefficients. For this reason, a simple methodology to estimate effective diffusion coefficients using FRAP experiments is to approximate the cell nucleus with a rectangle of length l, and set up the photobleaching profile as a narrow band of width $2h$ situated in the center of the cell nucleus in order to reduce the dimension of the problem from 2 to 1. By doing so, the problem reduces to fitting the experimental FRAP data with the theoretical fluorescence recovery curve, $F_B(t)$, given by equation (2.36), where the length l

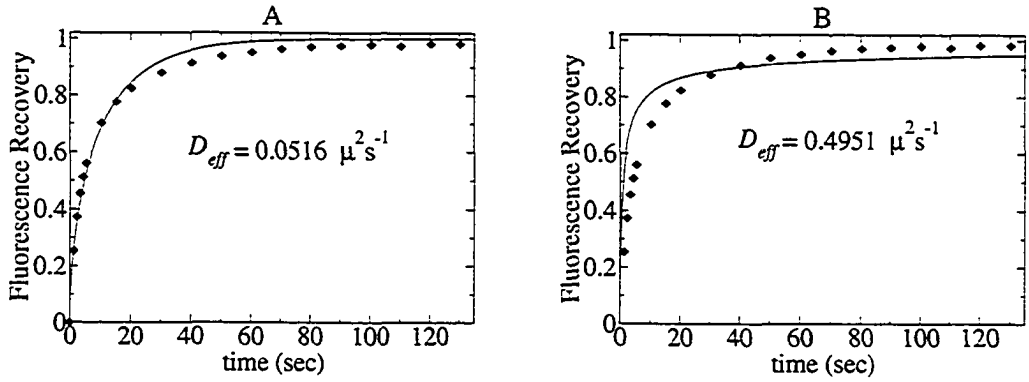

Figure 2.7: A: The GFP-histone H1 FRAP data (diamonds) are fitted with the theoretical recovery curve $\overline{F}_B(t)$, given by equation (2.42)(solid curve). From the fitting, an estimated effective diffusion coefficient, $D_{eff} = 0.0516\,\mu\text{m}^2/\text{s}$, is obtained. B: The same data (diamonds) are fitted with the theoretical recovery curve on an infinite domain, $F_U(t)$, given by equation (2.37)(solid curve). From the fitting, an overestimated effective diffusion coefficient, $D_{eff} = 0.4951\,\mu\text{m}^2/\text{s}$, is obtained.

has to be estimated in addition to the diffusion coefficient. However, it is easy to estimate l. In particular, by assuming that the fluorescence intensity in a nuclear region is proportional to its size, the length l can be estimated in terms of the fluorescence intensity on the nucleus before photobleaching, F_0, and immediately after photobleaching, F_a, as follows:

$$l = 2h\frac{F_0}{F_0 - F_a}\,. \tag{2.46}$$

To illustrate how this simple methodology works, FRAP data of two nuclear proteins, actin and histone H1, are analyzed. These proteins are of particular interest to the present research project. However, since the immediate purpose is to illustrate how effective diffusion coefficients can be estimated accurately, details regarding the dynamics of these proteins will be presented later. The FRAP experiments on these two proteins were performed by E. Crawford at the Cross Cancer Institute, University of Alberta.

The FRAP data on histone H1 are shown in figure 2.7, and obtained after tagging GFP to the protein in SK-N-SH human neuroblastoma cells, and photobleaching a narrow band of width $2h = 1.5\,\mu m$ in the cell nucleus. The data were normalized

with respect to the expected final fluorescence intensity in the bleached region after recovery,

$$F_a\left(1-\frac{F_a}{F_0}\right), \tag{2.47}$$

where $1-\frac{F_a}{F_0}$ represents the proportion of fluorescence intensity in the bleached region. Using equation (2.46), an estimated length $l = 5.6\,\mu m$ for the cell nucleus is obtained. To estimate an effective diffusion coefficient, the theoretical recovery curve $\overline{F}_B(t)$ (equation (2.42)) is fitted to the data using the method of nonlinear least squares [4, 78]. By doing so, an effective diffusion coefficient $D_{eff} = 0.0516\,\mu\text{m}^2/\text{s}$ for histone H1 is obtained (figure 2.7A). Also, to demonstrate that significantly different estimates may arise when assuming an infinite domain, the experimental FRAP data on histone H1 were fitted with the theoretical recovery curve $F_U(t)$ (equation (2.37)). From the fitting, an approximately tenfold overestimate of the effective diffusion coefficient, $D_{eff} = 0.4951\,\mu\text{m}^2/\text{s}$, is obtained (figure 2.7B).

The FRAP data for nuclear actin, shown in figure 2.8, were obtained after tagging GFP to the protein in HeLa cells, and photobleaching a narrow band of width $2h = 2\,\mu m$ in the cell nucleus. The data were normalized with respect to the expected final fluorescence intensity in the bleached region after recovery (equation (2.47)). Using equation (2.46), the estimated length of the cell nucleus is $l = 6.3\,\mu m$. By fitting the theoretical recovery curve $\overline{F}_B(t)$ (equation (2.42)) to the data, one obtains an estimated effective diffusion coefficient $D_{eff} = 0.2344\,\mu\text{m}^2/\text{s}$ for nuclear actin (figure 2.8A). The GFP-actin FRAP data is also fitted with the theoretical recovery curve on an infinite domain, $F_U(t)$, given by equation (2.37) (figure 2.8B). As expected, the fitting leads to an overestimation of the effective diffusion coefficient. Note that the latter fitting appears to be more accurate than the one on a bounded domain. However, this must not be taken in favor of using the fluorescence recovery on a unbounded domain, but rather as a sign that other aspects of the dynamics of nuclear actin should be considered.

We have, therefore, obtained a quantitative measurement of the overall mobility of histone H1 and actin in the cell nucleus. A more thorough analysis of the presented

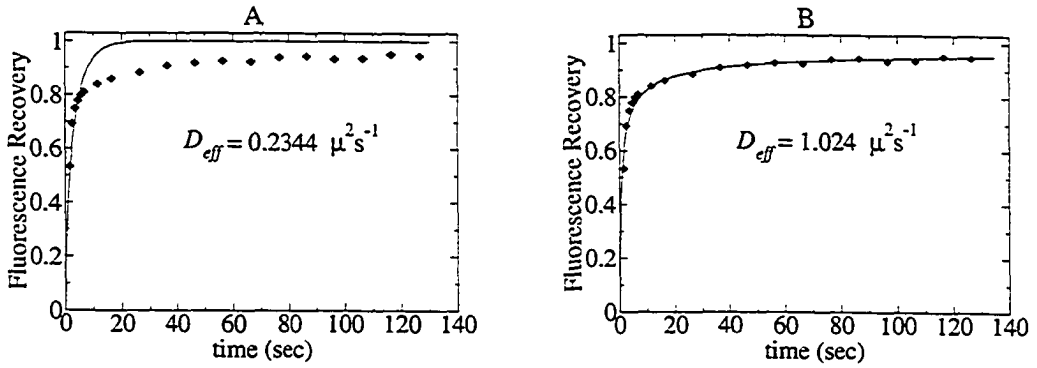

Figure 2.8: A: The GFP-actin FRAP data (diamonds) are fitted with the theoretical recovery curve $\overline{F}_B(t)$, given by equation (2.42)(solid curve). From the fitting, an estimated effective diffusion coefficient, $D_{eff} = 0.2344\,\mu\text{m}^2/\text{s}$, is obtained. B: The same data (diamonds) are fitted with the theoretical recovery curve on an infinite domain, $F_U(t)$, given by equation (2.37)(solid curve). From the fitting, an overestimated effective diffusion coefficient, $D_{eff} = 1.024\,\mu\text{m}^2/\text{s}$, is obtained.

FRAP data will be carried out in the next chapters.

2.4 Discussion

In this chapter, we have summarized how the diffusion equation is incorporated into the analysis of FRAP data. In particular, we have shown that the interpretation of FRAP data with theoretical recovery curves obtained from a diffusion process on an unbounded domain can easily lead to erroneous estimations. Therefore, to quantify the overall mobility of biomolecules wandering in a bounded domain, it is necessary to account for the boundary. In the context of FRAP experiments on proteins in the cell nucleus, the nuclear membrane plays an important role in the observed rate of fluorescence recovery, and its consideration allows for a more accurate estimation of effective diffusion coefficients.

When a bounded domain is taken into account, and the photobleached region is not too small compared to the size of the domain, differences in the rate of theoretical fluorescence recoveries due to the size and the location of the photobleached region become evident. These differences are qualitatively the same as the ones obtained

experimentally, and may contribute to the variability observed in the measurements when performing several FRAP experiments. Note that these differences cannot be explained if the diffusion process is assumed to take place on an infinite domain.

It is troublesome to consider aspects such as the shape of the domain or the location of the photobleaching if an explicit theoretical recovery curve is wanted. For this reason, we have reduced the problem of finding an explicit theoretical recovery curve to one dimension by approximating the shape of the cell nucleus with a rectangle and setting the photobleaching profile of the FRAP experiment to be a narrow band across the center of the domain. In this way, the simple methodology for estimating effective diffusion coefficients of nuclear proteins using FRAP experiments is to fit the theoretical recovery curve $\overline{F}_B(t)$, given by equation (2.42), to the experimental data (which is assumed to be normalized with respect to the expected final fluorescence intensity in the bleached region after recovery).

It is important to bear in mind that the effective diffusion coefficient represents only a quantification of the overall mobility of the nuclear protein under study. If one desires more specific information regarding protein interactions that may affect the rate of fluorescence recovery, then other mathematical models, describing the spatio-temporal dynamics of the fluorescent proteins, are needed to interpret the experimental FRAP data. Such models are the subject of chapters 3 and 4.

Chapter 3

Quantifying Protein Interactions by Interpreting FRAP Data with a Reaction-Diffusion Model

When analyzing the overall mobility of nuclear proteins using FRAP experiments, it was seen in chapter 2 that one could simply fit the diffusion equation to estimate an effective diffusion coefficient. However, this analysis offers very little in terms of describing more specific spatio-temporal dynamics. Most functional nuclear proteins interact with structures (e.g., chromatin, and splicing factor compartments) that are essentially immobile on the time scale of molecular movement. These interactions, that are described by binding and unbinding events, either may be involved in the performance of a catalytic or structural role in a biological process or may be a result of a sequestration into compartments that function to regulate the nucleoplasmic availability of specific nuclear proteins. Although diffusion is responsible for redistributing these biomolecules once they dissociate from their binding sites, the binding event itself might be the determining factor for the rate of a protein's movement throughout the nucleus. For this reason, it would be biologically infor-

mative to obtain measurements of binding and unbinding in addition to a diffusion coefficient.

In this chapter, we discuss the use of a reaction-diffusion model that is used to quantify FRAP data when molecular binding events are taking place. In particular, we focus on nuclear proteins that undergo binding and unbinding events with an approximately spatially homogeneous structure that is considered immobile on the time scale of molecular movement. For example, chromatin-associated proteins interact with interphase chromatin, which approaches a homogeneous distribution in human cell lines and is immobile on the time scale of a typical FRAP experiment [10]. Therefore, the proposed reaction-diffusion model is characterized by a resting (bound) and a moving (unbound) phase. This type of coupled dynamical system falls into the more general category of parabolic models with resting phase that have been studied by Hillen in [38]. Other applications of resting-moving dynamics can be found in [30, 54], where the authors modelled biological invasions with mobile and stationary states for dispersal and reproduction, and studied the effect of switching states on the invasion speed.

The particular reaction-diffusion model to be studied in this chapter has been applied previously in the context of reversible chemical reactions [16], and was used by Tardy et al. [101] to study the dynamics of cytoplasmic actin dynamics during photoactivated fluorescence (PAF) experiments. PAF experiments can be thought to be the negative analog of FRAP experiments, because a region is photoactivated instead of photobleached, i.e., the resultant image of the experiment is a bright spot (the region photoactivated) on a dark background. In their work, Tardy et al. [101] solved the model explicitly to interpret PAF measurements of cytoplasmic actin and estimate dynamical parameters such as the actin monomer diffusion coefficient, the filament turnover rate, and the ratio of polymerized and unpolymerized actin.

This chapter aims at understanding the proposed reaction-diffusion model in the context of FRAP experiments. The results are desirable in order to better appreciate a new model that will be introduced in chapter 4 and a more thorough analysis that will be carried out in chapter 5.

In section 3.1, the reaction-diffusion model is introduced in the context of FRAP experiments. On the basis of its solution, we obtain an explicit theoretical recovery curve that can be used to fit FRAP data in order to obtain a quantification of the interaction in terms of binding and unbinding rates (section 3.2). Applications to the dynamics of H1 histone and nuclear actin are presented in section 3.3. The chapter concludes with a brief discussion of the results (section 3.4).

3.1 The Reaction-Diffusion Model

A reaction-diffusion model is used to describe the dynamics of fluorescent diffusive proteins in the cell nucleus that undergo a reversible binding-unbinding process with a structure that is assumed to be immobile on the time scale of molecular movement and spatially homogeneously distributed (e.g., chromatin) [10]. The model is the well-known linear system of reaction-diffusion equations for reversible reactions subject to Neumann (no-flux) boundary conditions:

$$
\begin{aligned}
&\frac{\partial}{\partial t}u(x,t) = D\frac{\partial^2}{\partial x^2}u(x,t) - k_b u(x,t) + k_u v(x,t)\,, && x\in(0,l)\,, \quad t>0\,,\\
&\frac{\partial}{\partial t}v(x,t) = k_b u(x,t) - k_u v(x,t)\,, && x\in(0,l)\,, \quad t>0\,,\\
&\frac{\partial u}{\partial x} = \frac{\partial v}{\partial x} = 0\,, && x=0,l\,, \quad t>0\,,\\
&u(x,0) = f(x)\,, \quad v(x,0) = g(x)\,, && x\in(0,l)\,,
\end{aligned}
\tag{3.1}
$$

where u and v represent the population density of fluorescent biomolecules free to diffuse and bound to the immobile structure, respectively, D is the diffusion coefficient, k_b and k_u represent the binding and unbinding rates, respectively, t represents time, x is the spatial coordinate of position, $(0,l)$ is the spatial domain, and $f(x)$ and $g(x)$ are the initial conditions of fluorescent unbound and bound species immediately after photobleaching, respectively.

Note that the spatial domain in equation (3.1) is one-dimensional, which means that the shape of the domain (the cell nucleus) has been approximated with a rectangle of length l, and that the photobleaching profile has been assumed to be a narrow band of width $2h$, as discussed previously in section 2.1.2. Therefore,

the length l can be estimated using equation (2.46). Moreover, assuming that the photobleaching is centered at c, and performed in a cell nucleus that has reached a homogeneous steady-state solution (u_0, v_0) that satisfies $u_0 + v_0 = 1$, we can express the initial conditions of equation (3.1) as

$$f(x) = \begin{cases} 0\,, & |x-c| \leq h\,, \\ P_u\,, & |x-c| > h\,, \end{cases} \tag{3.2}$$

and

$$g(x) = \begin{cases} 0\,, & |x-c| \leq h\,, \\ P_b\,, & |x-c| > h\,, \end{cases} \tag{3.3}$$

where $P_u = \dfrac{k_u}{k_b + k_u}$ and $P_b = \dfrac{k_b}{k_b + k_u}$ represent the proportions of unbound and bound populations, respectively.

3.2 Explicit Solution and Theoretical Recovery Curve

Analogously to the previous chapter, we can obtain a theoretical recovery curve that can be used to fit FRAP data by integrating the solution of the reaction-diffusion equations (3.1)-(3.3) over the photobleached region. The following theorem summarizes the results of this procedure.

Theorem 1. Assume that the system of reaction-diffusion equations (3.1)-(3.3) is used to describe the dynamics of a fluorescent protein in a FRAP experiment where a narrow band of width $2h$ is photobleached. If the FRAP data is presented normalized with respect to the expected final fluorescence intensity in the bleached region after recovery, then the following theoretical recovery curve can be used to fit the data:

$$F(t) = 1 - \frac{l^2}{h(l-2h)(k_b+k_u)} \sum_{n=1}^{\infty} \left(B_{1n} F_{1n} e^{r_{1n} t} + B_{2n} F_{2n} e^{r_{2n} t} \right) S_n^2\,, \tag{3.4}$$

where the length l can be estimated using equation (2.46),

$$S_n = \frac{1}{n\pi} \left[\sin\left(\frac{n\pi(c-h)}{l} \right) - \sin\left(\frac{n\pi(c+h)}{l} \right) \right]\,, \tag{3.5}$$

$$r_{jn} = -\frac{k_b + k_u + D\left(\frac{n\pi}{l}\right)^2}{2} + (-1)^{j+1}\frac{Q_n}{2}\,, \quad j = 1,2\,, \tag{3.6}$$

$$Q_n = \sqrt{\left[k_b + k_u + D\left(\frac{n\pi}{l}\right)^2\right]^2 - 4k_u D\left(\frac{n\pi}{l}\right)^2}\,, \tag{3.7}$$

$$F_{jn} = (-1)^{j+1}\frac{r_{jn} + k_b + k_u}{Q_n}\,, \quad j = 1,2\,, \tag{3.8}$$

$$B_{jn} = k_b + k_u + r_{jn} + D\left(\frac{n\pi}{l}\right)^2\,, \quad j = 1,2\,. \tag{3.9}$$

Proof. To obtain an explicit solution for the system of reaction-diffusion equations (3.1)-(3.3), we apply the method of Laplace transforms (see [44] or [116]). We denote the Laplace transforms of $u(x,t)$ and $v(x,t)$ as

$$\mathcal{L}(u) = \hat{u}\,(x,s) = \int_0^\infty u(x,t)e^{-st}dt\,, \quad \mathcal{L}(v) = \hat{v}\,(x,s) = \int_0^\infty v(x,t)e^{-st}dt\,, \tag{3.10}$$

respectively. The Laplace transforms of the partial derivatives $\frac{\partial u}{\partial t}$ and $\frac{\partial v}{\partial t}$ are given by

$$\begin{aligned} \mathcal{L}\left(\frac{\partial u}{\partial t}\right) &= s\mathcal{L}(u) - u(x,0) = s\hat{u}\,(x,s) - u(x,0)\,, \\ \mathcal{L}\left(\frac{\partial v}{\partial t}\right) &= s\mathcal{L}(v) - v(x,0) = s\hat{v}\,(x,s) - v(x,0)\,. \end{aligned} \tag{3.11}$$

Using (3.10) and (3.11), the system of reaction-diffusion equations (3.1)-(3.3) is reduced to

$$\begin{aligned} & s\,\hat{u}\,(x,s) - f(x) = D\,\frac{\partial^2 \hat{u}}{\partial x^2} - s\,\hat{v}\,(x,s) + g(x)\,, && x \in (0,l)\,, \\ & s\,\hat{v}\,(x,s) - g(x) = k_b\hat{u}\,(x,s) - k_u\hat{v}\,(x,s)\,, && x \in (0,l)\,, \\ & \frac{\partial \hat{u}}{\partial x} = 0\,, && x = 0, l\,. \end{aligned} \tag{3.12}$$

From the second equation of (3.12), we obtain

$$\hat{v}\,(x,s) = \frac{k_b\,\hat{u}\,(x,s) + g(x)}{s + k_u}\,. \tag{3.13}$$

Replacing this last expression into the first equation of (3.12), the following second-order ordinary differential equation for $\hat{u}\,(x,s)$ with respect to x is obtained:

$$\begin{aligned} &D\,\frac{\partial^2 \hat{u}}{\partial x^2} + g(s)\,\hat{u}\,(x,s) + p\,(x,s) = 0\,, \quad x \in (0,l)\,, \\ &\frac{\partial \hat{u}}{\partial x} = 0\,, \qquad\qquad\qquad\qquad\qquad\quad x = 0, l\,. \end{aligned} \tag{3.14}$$

where

$$g(s) = -s\left(\frac{k_b}{s + k_u} + 1\right)\,, \tag{3.15}$$

$$p\,(x,s) = f(x) + \left(1 - \frac{s}{s + k_u}\right) g(x)\,. \tag{3.16}$$

The objective now is to solve the second-order equation (3.14) and then apply the inverse Laplace transform to the solution $\hat{u}\,(x,s)$ in order to obtain $u(x,t)$. To solve (3.14), we assume that its solution is given by the Fourier series

$$\hat{u}\,(x,s) = A_0(s) + \sum_{n=1}^{\infty} A_n(s) \cos\left(\frac{n\pi x}{l}\right)\,, \tag{3.17}$$

and express equation (3.16) also as a Fourier series, namely

$$p(x,s) = a_0(s) + \sum_{n=1}^{\infty} a_n(s) \cos\left(\frac{n\pi x}{l}\right)\,, \tag{3.18}$$

where

$$\begin{aligned} a_0(s) &= \frac{1}{l}\int_0^l p(x,s)\,dx = \frac{1}{l}\left(\frac{s + k_b + k_u}{s + k_u}\right)\frac{k_u}{k_b + k_u}\,(l - 2h)\,, \\ a_n(s) &= \frac{2}{l}\int_0^l \cos\left(\frac{n\pi x}{l}\right) p(x,s)\,dx = 2\left(\frac{s + k_b + k_u}{s + k_u}\right)\frac{k_u}{k_b + k_u}\,S_n\,, \end{aligned} \tag{3.19}$$

and S_n is given in equation (3.5). To find the Fourier coefficients $A_i(s)$, $i = 0, 1, 2, \ldots$, of the solution $\hat{u}\,(x,s)$, the Fourier series (3.17) and (3.18) are substituted into the second-order equation (3.14). By doing so, the following equality is obtained

$$g(s)A_0(s) + \sum_{n=1}^{\infty}\left(g(s) - D\left(\frac{n\pi}{l}\right)^2\right) A_n(s)\cos\left(\frac{n\pi x}{l}\right) = -a_0(s) - \sum_{n=1}^{\infty} a_n(s)\cos\left(\frac{n\pi x}{l}\right)\,. \tag{3.20}$$

By equating the coefficients of the Fourier series in the left- and right-hand sides of (3.20), we obtain

$$
\begin{aligned}
A_0(s) &= -\frac{a_0(s)}{g(s)}\,, \\
A_n(s) &= -\frac{a_n(s)}{g(s) - D\left(\frac{n\pi}{l}\right)^2}\,.
\end{aligned}
\tag{3.21}
$$

Substitution of expression (3.15) for $g(s)$ and expressions (3.19) for $a_0(s)$ and $a_n(s)$ into the Fourier coefficients (3.21) of $\hat{u}\,(x,s)$ yields

$$
\begin{aligned}
A_0(s) &= \frac{1}{s}\frac{k_u}{k_b+k_u}\frac{l-2h}{l}\,, \\
A_n(s) &= \frac{2s\left[k_u/(k_b+k_u)\right]S_n + 2k_u S_n}{(s-r_{1n})(s-r_{2n})}\,,
\end{aligned}
\tag{3.22}
$$

where S_n is as in equation (3.5), and r_{1n} and r_{2n} are as given in equation (3.6). It is convenient to rewrite $A_n(s)$ as

$$
\begin{aligned}
A_0(s) &= \frac{A}{s}\,, \\
A_n(s) &= \frac{A_{1n}}{s-r_{1n}} + \frac{A_{2n}}{s-r_{2n}}\,,
\end{aligned}
\tag{3.23}
$$

where

$$
\begin{aligned}
A &= \frac{k_u}{k_b+k_u}\frac{l-2h}{l}\,, \\
A_{jn} &= 2\frac{k_u}{k_b+k_u}S_n F_{jn}\,, \quad j=1,2\,,
\end{aligned}
\tag{3.24}
$$

and F_{jn} is as given in equation (3.8).

With the Fourier coefficients (3.23) in hand, we now have the solution $\hat{u}\,(x,s)$ for (3.14), namely equation (3.17). To obtain the solution $u(x,t)$ of (3.1), we take the inverse Laplace transform, denoted by $\mathcal{L}^{-1}$, of $\hat{u}\,(x,s)$. In particular,

$$
u(x,t) = \mathcal{L}^{-1}(\hat{u}\,(x,s)) = \mathcal{L}^{-1}(A_0(s)) + \sum_{n=1}^{\infty}\mathcal{L}^{-1}(A_n(s))\cos\left(\frac{n\pi x}{l}\right)\,.
\tag{3.25}
$$

Using the fact that

$$
\begin{aligned}
\mathcal{L}^{-1}(A_0(s)) &= \mathcal{L}^{-1}\left(\frac{A}{s}\right) = A = \frac{k_u}{k_b+k_u}\frac{l-2h}{l}\,, \\
\mathcal{L}^{-1}(A_n(s)) &= \mathcal{L}^{-1}\left(\frac{A_{1n}}{s-r_{1n}} + \frac{A_{2n}}{s-r_{2n}}\right) = A_{1n}e^{r_{1n}t} + A_{2n}e^{r_{2n}t} \\
&= 2\frac{k_u}{k_b+k_u}\left(S_n F_{1n}e^{r_{1n}t} + S_n F_{2n}e^{r_{2n}t}\right)\,,
\end{aligned}
\tag{3.26}
$$

the solution $u(x,t)$ can be written as

(3.27)

$$u(x,t) = \frac{k_u}{k_b+k_u}\frac{l-2h}{l} + 2\frac{k_u}{k_b+k_u}\sum_{n=1}^{\infty}\left(S_nF_{1n}e^{r_{1n}t} + S_nF_{2n}e^{r_{2n}t}\right)\cos\left(\frac{n\pi x}{l}\right),$$

where S_n, r_{jn}, and F_{jn}, $j = 1,2$, are given by equations (3.5), (3.6), and (3.8), respectively.

To obtain $v(x,t)$, we first isolate it from the first equation in (3.1),

$$v(x,t) = \frac{1}{k_u}\left(\frac{\partial}{\partial t}u(x,t) - D\frac{\partial^2}{\partial x^2}u(x,t) + k_b u(x,t)\right). \tag{3.28}$$

By substituting the solution (3.27) for $u(x,t)$ into equation (3.28), the following expression for the solution $v(x,t)$ of (3.1) is obtained:

(3.29)

$$v(x,t) = \frac{k_b}{k_b+k_u}\frac{l-2h}{l} + \frac{2}{k_b+k_u}\sum_{n=1}^{\infty}\left(B_{1n}S_nF_{1n}e^{r_{1n}t} + B_{2n}S_nF_{2n}e^{r_{2n}t}\right)\cos\left(\frac{n\pi x}{l}\right),$$

where S_n, r_{jn}, F_{jn}, and B_{jn}, $j = 1,2$, are given by equations (3.5), (3.6), (3.8), and (3.9), respectively.

Having an explicit solution $(u(x,t), v(x,t))$ for the system of reaction-difusion equations (3.1)-(3.3), given by equations (3.27) and (3.29), we are now in a position to obtain a theoretical fluorescence recovery curve $F(t)$ to fit the FRAP data. Integrating the total concentration of fluorescent biomolecules $c(x,t) = u(x,t) + v(x,t)$ over the photobleached region $\Lambda = [c-h, c+h]$, and normalizing the result with respect to the recovery level of the total fluorescent population in the photobleached region, we obtain the following theoretical fluorescence recovery curve:

$$\begin{aligned} F(t) &= \frac{\int_{c-h}^{c+h} c(x,t)dt}{\lim_{t\to\infty}\int_{c-h}^{c+h} c(x,t)dt} = \frac{l}{2h(l-2h)}\int_{c-h}^{c+h}\left(u(x,t)+v(x,t)\right)dt \\ &= 1 - \frac{l^2}{h(l-2h)(k_b+k_u)}\sum_{n=1}^{\infty}\left(B_{1n}F_{1n}e^{r_{1n}t} + B_{2n}F_{2n}e^{r_{2n}t}\right)S_n^2, \end{aligned} \tag{3.30}$$

where S_n, r_{jn}, F_{jn}, and B_{jn}, $j = 1,2$, are given by equations (3.5), (3.6), (3.8), and (3.9), respectively. This concludes the proof. □

3.3 Application to the Dynamics of Nuclear Proteins

In this section, we will discuss the application of the reaction-diffusion model (3.1) in combination with FRAP experiments to the dynamics of two nuclear proteins, namely (1) a chromatin-associated protein, histone H1 (section 3.3.1), and (2) nuclear actin (section 3.3.2).

3.3.1 Histone H1

Complexes of eukaryotic DNA and other nuclear proteins are referred to as chromatin. The majority of chromatin-associated proteins are the histones, which are abundant nuclear proteins that package the DNA in the cell nucleus. Specifically, the DNA is wrapped around histones in units called nucleosomes, and sealed by a particular type of histone called histone H1.

Like many other nuclear proteins, histone H1 moves passively by rapid diffusion through the nuclear space. In addition to this, histone H1 binds (unbinds) to (from) the chromatin structure. The binding (unbinding) of histone proteins to (from) the chromatin regulates its organization, which in turn influences protein interactions and gene expression [51, 86]. In the case of histone H1, this turnover process occurs very rapidly [18, 27, 51, 69]. This rapid transient binding to the chromatin structure can affect considerably its overall mobility, and therefore the rate of fluorescence recovery in a FRAP experiment.

In order to quantify the mobility of histone H1 and its transient binding to the chromatin structure, the reaction-diffusion model (3.1) is applied to the dynamics of histone H1 during FRAP experiments. More specifically, photobleaching is performed with a band profile on a cell nucleus during the interphase (the interval between periods of chromosomal and cell division) of the cell cycle, when the chromatin structure can be assumed to be homogeneously distributed throughout the cell nucleus [14]. Since the chromatin structure is relatively immobile on the time scale of molecular movement and during the typical lasting time of FRAP experiments, we are able to model the dynamics of histone H1 with the system of

reaction-diffusion equations (3.1)-(3.3), where $u(x,t)$ represents the population density of histone H1 that is free to diffuse and $v(x,t)$ represents the the population density of histone H1 bound to the chromatin structure.

With the application of the reaction-diffusion model (3.1) to the dynamics of histone H1 during FRAP experiments, we can extract quantitative information about the biophysical properties of this chromatin-associated protein. In particular, we can determine the following biological information:

- $\tau_r = \dfrac{1}{k_u}$: the average residence time of the protein bound to the chromatin structure;
- $\tau_w = \dfrac{1}{k_b}$: the average time between binding events;
- $P_b = \dfrac{k_b}{k_b + k_u}$: the proportion of the protein bound to the chromatin structure;
- $P_u = \dfrac{k_u}{k_b + k_u}$: the proportion of the protein free to diffuse,

where k_b and k_u are the binding and unbinding rates of histone H1 to the chromatin structure, respectively. The estimation of these parameters is important if one wants to describe quantitatively the *in vivo* behaviour of a protein [10].

We revisit the FRAP data on histone H1 that were presented earlier in section 2.3.2. The data are presented again in figure 3.1 (diamonds). To estimate the diffusion coefficient D, and the binding and unbinding rates, k_b and k_u, we applied theorem 1. More specifically, the theoretical fluorescence recovery curve given by equation (3.4) is fitted to the FRAP data using the method of nonlinear least squares [4, 78]. By doing so, estimations for the diffusion coefficient, $D = 0.073\,\mu\text{m}^2/\text{s}$, the binding rate, $k_b = 0.0026\,\text{s}^{-1}$, and the unbinding rate, $k_u = 0.0193\,\text{s}^{-1}$, are obtained (figure 3.1). With these estimated parameters, we obtain a proportion $P_b = k_b/(k_b + k_u) \approx 0.12$ of the population of histone H1 that is bound to the chromatin structure and a proportion $P_u = k_u/(k_b + k_u) \approx 0.88$ that is free to diffuse.

Note that the estimated diffusion coefficient, $D = 0.073\,\mu\text{m}^2/\text{s}$, is higher than the effective diffusion coefficient, $D_{eff} = 0.0516\,\mu\text{m}^2/\text{s}$, obtained by fitting the dif-

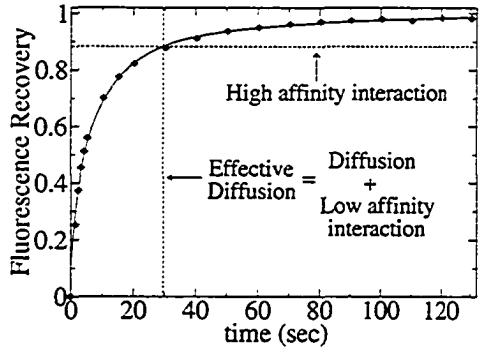

Figure 3.1: GFP-histone H1 FRAP data (diamonds) are fitted with the theoretical recovery curve (3.4) (solid curve). From the fitting, estimations for the diffusion coefficient, $D = 0.073\,\mu\text{m}^2/\text{s}$, the binding rate, $k_b = 0.0026\,\text{s}^{-1}$, and the unbinding rate, $k_u = 0.0193\,\text{s}^{-1}$, are obtained.

fusion equation to the data (figure 2.7), but it is still smaller than expected for a diffusing biomolecule of the molecular weight of histone H1. Also, and most important, the proportion of bound population P_b is very low and smaller than biologically expected; one would expect a high proportion of histone H1 to be bound to the chromatin structure because of the role that histone H1 plays in the packing of chromatin. To interpret this apparent discrepancy, we hypothesized that the 12% obtained for the bound population actually corresponds to a high-affinity (strongly) bound subpopulation of histone H1, and the apparent high percentage of free biomolecules is comprised by the actual diffusing subpopulation and a low-affinity (weakly) bound subpopulation (figure 3.1). This means that the estimated diffusion coefficient is an effective diffusion coefficient that accounts for the actual diffusing population and for the weakly bound population. This hypothesis is consistent with the experimental evidence of a rapid exchange of histone H1 on chromatin [51], and will be corroborated in chapter 5, where a more thoroughly analysis of both the data and the model is carried out.

3.3.2 Nuclear Actin

The second application is related to the dynamics of nuclear actin. Actin is an abundant cellular protein that is present in both monomeric and polymeric forms.

These forms of actin are also referred to as globular (G-actin) and filamentous (F-actin) forms, respectively. The use of the term polymeric accounts for the assembly of monomers into filaments.

Actin is widely known for its functions in the cytoplasm: it plays a major role in the structural organization, movement and division of the cell. Nonetheless, actin is not a protein exclusive to the cytoplasm. It is also known to be present in the nucleus. Nuclear actin has recently been identified as a functional component of chromatin remodelling complexes and is thought to be a structural element of a nuclear matrix as well [7, 91, 105]. Yet a long-standing question in cell biology is whether or not polymeric actin (F-actin) is common to cell nuclei. Recent work has provided evidence that nuclear actin is present in filamentous form [61]. In order to support this result and obtain quantitative estimates of the size of the globular and filamentous pools of actin in a cell nucleus, we will apply theorem 1 to nuclear actin FRAP data.

In particular, we revisit the FRAP data on nuclear actin that were presented earlier in section 2.3.2. The data are presented again in figure 3.2 (diamonds). We observe that the FRAP curve comprises a fast recovery phase and a slow recovery phase. Recall from section 2.3.2 that the fast phase is fitted well by the theoretical fluorescence recovery curve (2.42) coming from the diffusion equation (2.14), whereas the slow phase is not (figure 2.8A). In other words, a simple diffusion process does not account for these two phases of the recovery. A valid explanation for both the fast and slow phases can be given if the data are interpreted with the reaction-diffusion model (3.1).

The main biological assumptions that need to be made in order to interpret the FRAP data with the reaction-diffusion model (3.1) are the following:

- two populations of actin are considered, namely a globular population $u(x,t)$ that is free to diffuse, and an immobile filamentous population $v(x,t)$;
- there is no net growth of the globular or filamentous population pools on the time scale of the experiment;

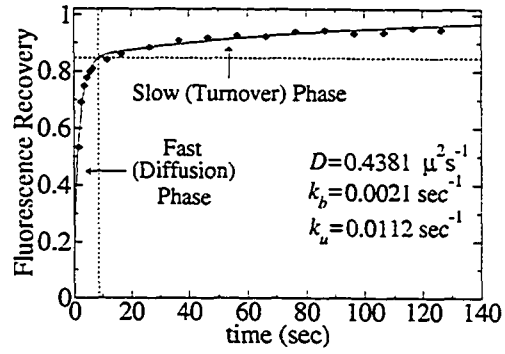

Figure 3.2: GFP-actin FRAP data (diamonds) are fitted with the theoretical recovery curve (3.4) (solid curve). From the fitting, estimations for the diffusion coefficient, $D = 0.4381\,\mu\text{m}^2/\text{s}$, the association rate, $k_b = 0.0021\,\text{s}^{-1}$, and the dissociation rate, $k_u = 0.0112\,\text{s}^{-1}$, are obtained.

- there is an exchange rate between the two populations that is uniform throughout the nucleus, and is described by an association rate k_b of globular actin to the filamentous pool, and a dissociation rate k_u of globular actin from the filaments.

Fitting of recovery curve (3.4) to the FRAP data yields estimates for the diffusion coefficient, $D = 0.4381\,\mu\text{m}^2/\text{s}$, the association rate, $k_b = 0.0021\,\text{s}^{-1}$, and the dissociation rate, $k_u = 0.0112\,\text{s}^{-1}$. The fitting is quite accurate for both the slow and fast phases of the recovery. The fast phase is attributed to the fast diffusion whereas the turnover of globular actin into an immobile population is responsible for the slow recovery phase (figure 3.2). Moreover, with these estimated parameters, we are now in a position to extract the following important quantitative information of GFP-actin in the nucleus:

- $\tau_r = \dfrac{1}{k_u} \approx 89\,\text{sec}$: the average residence time of GFP-actin in filamentous form;
- $\tau_w = \dfrac{1}{k_b} \approx 476\,\text{sec}$: the average wandering time of GFP-actin between associations to filaments;
- $P_b = \dfrac{k_b}{k_b + k_u} = 0.16$: the proportion of GFP-actin in filamentous form;

- $P_u = \dfrac{k_u}{k_b + k_u} = 0.84$: the proportion of GFP-actin in globular form.

3.4 Discussion

It has become clear in this section that the interpretation of FRAP experimental data for nuclear proteins depends on the available knowledge of the particular molecular behaviour of the protein under consideration and the mathematical model used to describe the dynamics of the biomolecules. The quantitative analysis of FRAP data for nuclear proteins undergoing a reversible binding process using the reaction-diffusion model (3.1) provides relevant biological information such as binding affinities, residence time of the protein in bound state, proportion of the protein population dynamically bound, and proportion of the protein population moving freely by diffusion.

We applied the reaction-diffusion model first to the dynamics of histone H1, a chromatin-binding protein. Although the fitting of the data was quite accurate, the quantitative estimate obtained for the proportion of bound population to the chromatin structure was much lower than biologically expected. To interpret this apparent discrepancy we hypothesize that there are two types of binding interactions of histone H1 with the chromatin structure, namely a low-affinity (weak binding) interaction, and a high-affinity (strong binding) interaction. This hypothesis is consistent with the experimental evidence of a rapid exchange of histone H1 on chromatin [51], and will be the subject of further investigation in chapter 5.

The reaction-diffusion model (3.1) was also applied to the dynamics of nuclear actin. By assuming the existence of an "immobile" filamentous population in the cell nucleus, the FRAP data was interpreted with the reaction-diffusion model, and the theoretical recovery curve (3.4) obtained from it was fitted accurately to the FRAP data. The biphasic behaviour of the experimental data was explained satisfactorily by the model, and a quantification of the proportions of the population in globular and filamentous forms was obtained.

The importance of studying the functional interactions of histone H1 and actin

in the nucleus directly by monitoring the molecular flux of molecules at steady-state using FRAP and the reaction-diffusion model (3.1) lies in the fact that quantitative differences in the binding affinity of proteins is believed to be the basis for developmental regulation of gene expression and the resultant differentiation of cells into different cell types and tissues. These results promise to be a useful tool for quantifying the effect of mutations in proteins, which is a critical stepping stone for understanding the functional dynamics of the genome.

Chapter 4

Simplifying the Task of Parameter Estimation by Interpreting FRAP Data with a Compartmental Model

As mentioned in chapter 3, important biological information to be determined when analyzing FRAP experimental data for nuclear proteins undergoing a reversible binding process is the residence time of the protein in a bound state and the sizes of the bound and free pools. This quantitative information can be obtained from the time-dependent parameters representing the binding and unbinding rates, and does not make any use of spatial information. Motivated by this fact, and noticing that FRAP data are presented as a time-dependent function, we will propose a simple compartmental model (a linear system of ordinary differential equations) that describes the dynamics during FRAP experiments of nuclear proteins undergoing a reversible binding process with a homogeneously distributed and immobile structure. In contrast to the reaction-diffusion system (3.1), space will not be considered explicitly. This will simplify the task of parameter estimation and will make the analysis more accessible and understandable to the experimentalists.

After introducing the compartmental model (section 4.1), it will be solved explicitly in order to obtain a theoretical recovery curve that can be used to fit FRAP data (section 4.2). In section 4.3, the parameter estimation methodology will be presented and applied to the dynamics of nuclear actin. The chapter will end with a discussion of the results (section 4.4).

4.1 The Compartmental Model

Similar to the reaction-diffusion model (3.1), the proposed compartmental model assumes two interacting populations, namely a population of biomolecules that can move freely, and a bound population of biomolecules. When performing a photobleaching of a narrow band in the center of the cell nucleus, both populations occupy three physical compartments within the cell nucleus, namely the photobleached region C_0 that spans the cell nucleus, the left unbleached region C_1, and the right unbleached region C_2 (figure 4.1A). The schematic model illustrated in figure 4.1B describes the dynamics of fluorescent biomolecules. The model can be translated into the following system of ordinary differential equations,

$$
\begin{aligned}
\dot{u}_0 &= -2D_1u_0 + D_2u_1 + D_2u_2 - k_bu_0 + k_uv_0 \,, \\
\dot{u}_1 &= D_1u_0 - D_2u_1 - k_bu_1 + k_uv_1 \,, \\
\dot{u}_2 &= D_1u_0 - D_2u_2 - k_bu_2 + k_uv_2 \,, \\
\dot{v}_0 &= k_bu_0 - k_uv_0 \,, \\
\dot{v}_1 &= k_bu_1 - k_uv_1 \,, \\
\dot{v}_2 &= k_bu_2 - k_uv_2 \,,
\end{aligned}
\tag{4.1}
$$

where the dot denotes the derivative with respect to time t, u_0, u_1, and u_2 represent the populations of diffusing fluorescent molecules in C_0, C_1, and C_2, respectively, v_0, v_1, and v_2 represent the populations of fluorescent molecules bound to the immobile structure in C_0, C_1, and C_2, respectively, k_b is the binding rate of molecules to the immobile structure, k_u is the unbinding rate of molecules from the structure, D_1 is the fractional diffusional transfer coefficient from compartment C_0 to compartment

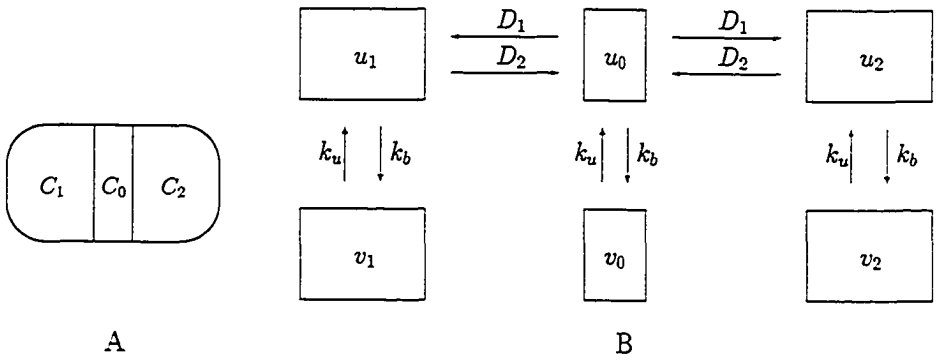

Figure 4.1: A: Three compartments are formed during FRAP experiments: the photobleached region C_0, the left unbleached region C_1, and the right unbleached region C_2. B: Compartmental model describing the dynamics of fluorescent proteins undergoing binding and unbinding events, after photobleaching a narrow band across the cell nucleus. u_0, u_1, and u_2 represent the populations of diffusing fluorescent molecules in C_0, C_1, and C_2, respectively, v_0, v_1, and v_2 represent the populations of fluorescent molecules bound to the immobile structure in C_0, C_1, and C_2, respectively, k_b and k_u are the binding and unbinding rates, and D_1 and D_2 are the fractional diffusional transfer coefficients.

C_1 or C_2, and D_2 is the fractional diffusional transfer coefficient from compartments C_1 and C_2 to compartment C_0. Also, it is assumed that there is no direct transfer from compartment C_1 to C_2, and viceversa.

Under the symmetry assumption that photobleaching is performed on a uniform steady state of fluorescent biomolecules in the center of the nucleus, C_1 and C_2 have the same size, $u_1 = u_2$, and $v_1 = v_2$. Thus, system (4.1) can be reduced to four equations. Despite this fact, we continue the analysis with six equations. This maintains the clarity of the relation of the schematic model of the experimental setup (figure 4.1) with the system of ordinary differential equations (4.1), and does not add any significant difficulty to the analysis.

Note that if the compartmental model (4.1) were to be used to interpret FRAP data, four parameters would have to be estimated. However, the "fractional diffusional transfer" coefficients D_1 and D_2 can be expressed in terms of a new parameter,

D_t, called the "diffusional transfer coefficient", and defined as

$$D_t = D_1 + D_2 \,. \tag{4.2}$$

To understand how D_1 and D_2 can be expressed in terms of D_t, we denote the steady state describing the uniform distribution of fluorescent biomolecules by

$$(\bar{u}, \bar{v}) = (\bar{u}_0, \bar{u}_1, \bar{u}_2, \bar{v}_0, \bar{v}_1, \bar{v}_2) \,. \tag{4.3}$$

By setting all the equations in system (4.1) to zero we find that

$$(\bar{u}, \bar{v}) = \left(\frac{k_u}{k_b} \frac{D_2}{D_1}, \frac{k_u}{k_b}, \frac{k_u}{k_b}, \frac{D_2}{D_1}, 1, 1 \right) K \,, \tag{4.4}$$

where K is determined by the total amount of biomolecules in the cell nucleus. On the one hand, the second and third coordinates of the steady state $(\bar{u}, \bar{v})$ are given by

$$\bar{u}_1 = \bar{u}_2 = \frac{D_1}{D_2} \bar{u}_0 \,. \tag{4.5}$$

On the other hand, assuming that the fluorescence in each compartment is proportional to the amount of fluorescent biomolecules in it, and denoting the total fluorescence in the cell nucleus before photobleaching by F_0, and the fluorescence in the nucleus immediately after photobleaching by F_a, we also have that

$$\bar{u}_0 \propto \frac{F_0 - F_a}{F_0} \,, \quad \bar{u}_1 = \bar{u}_2 \propto \frac{F_a/2}{F_0} \,, \tag{4.6}$$

and therefore,

$$\bar{u}_1 = \bar{u}_2 = \frac{F_a/2}{F_0 - F_a} \bar{u}_0 \,. \tag{4.7}$$

From equations (4.5) and (4.7), we conclude that the fractional diffusional transfer coefficients have to satisfy the following

$$\frac{D_1}{D_2} = \frac{F_a/2}{F_0 - F_a} \,. \tag{4.8}$$

Finally, from the definition of the diffusional transfer coefficient (4.2), and equation (4.8), we conclude that the fractional diffusional transfer coefficients D_1 and D_2 can

be described in terms of the diffusional transfer coefficient D_t, as follows

$$
\begin{aligned}
D_1 &= \frac{F_a/2}{F_0 - F_a/2} D_t = \frac{r}{2-r} D_t \,, \\
D_2 &= \frac{F_0 - F_a}{F_0 - F_a/2} D_t = 2\,\frac{1-r}{2-r} D_t \,,
\end{aligned}
\tag{4.9}
$$

where

$$
r = \frac{F_a}{F_0} < 1 \,. \tag{4.10}
$$

In light of relation (4.9), there are now three instead of four unknown parameters to be estimated, namely D_t, k_b, and k_u.

4.2 Explicit Solution and Theoretical Recovery Curve

In order to solve system (4.1) and derive the theoretical recovery curve based on the compartmental model, an initial condition for system (4.1) is required. The following proposition provides this initial condition.

Proposition 2. Assume that the compartmental model (4.1) describes the dynamics of fluorescent nuclear proteins in a FRAP experiment. If the photobleaching of a narrow band is performed on an equilibrium state $(\bar{u}, \bar{v}) = (\bar{u}_0, \bar{u}_1, \bar{u}_2, \bar{v}_0, \bar{v}_1, \bar{v}_2)$ that satisfies $\bar{u}_0 + \bar{u}_1 + \bar{u}_2 + \bar{v}_0 + \bar{v}_1 + \bar{v}_2 = 1$, then the initial condition that reflects the FRAP experimental setting is given by

$$
(\bar{u}_0, \bar{v}_0) = \left(0, \frac{k_u}{k_b + k_u}\frac{r}{2}, \frac{k_u}{k_b + k_u}\frac{r}{2}, 0, \frac{k_b}{k_b + k_u}\frac{r}{2}, \frac{k_b}{k_b + k_u}\frac{r}{2}\right) \,, \tag{4.11}
$$

where r is as in equation (4.10).

Proof. Before photobleaching is performed, the distribution of fluorescent biomolecules is given by the steady state $(\bar{u}, \bar{v})$, expressed in equation (4.4). Photobleaching a region C_0 will disrupt this equilibrium: there no longer are fluorescent biomolecules in compartment C_0. Therefore, the initial condition for the compartmental model (4.1) that reflects the FRAP experimental setup is given by

$$
(\bar{u}_0, \bar{v}_0) = \left(0, \frac{k_u}{k_b}, \frac{k_u}{k_b}, 0, 1, 1\right) K \,. \tag{4.12}
$$

The restriction $\bar{u}_0 + \bar{u}_1 + \bar{u}_2 + \bar{v}_0 + \bar{v}_1 + \bar{v}_2 = 1$ on the steady state (4.4) provides $K = \dfrac{k_b}{k_b + k_u}\dfrac{r}{2}$. Thus, using this value for K, it follows that the initial condition (4.12) can be rewritten as equation (4.11). This completes the proof. □

With the initial condition (4.11) in hand, and using matrix notation, the system (4.1) can be rewritten as the following initial-value problem:

$$\begin{aligned} \dot{\boldsymbol{w}} &= A\,\boldsymbol{w}\,, \\ \boldsymbol{w}(0) &= \boldsymbol{w_0}\,, \end{aligned} \tag{4.13}$$

where $\boldsymbol{w} = (u_0, u_1, u_2, v_0, v_1, v_2)^T$, the initial condition $\boldsymbol{w_0} = (\bar{u}_0, \bar{v}_0)^T$, with $(\bar{u}_0, \bar{v}_0)$ given by (4.11), and A is the following 6×6 matrix:

$$A = \begin{pmatrix} -2D_1 - k_b & D_2 & D_2 & k_u & 0 & 0 \\ D_1 & -D_2 - k_b & 0 & 0 & k_u & 0 \\ D_1 & 0 & -D_2 - k_b & 0 & 0 & k_u \\ k_b & 0 & 0 & -k_u & 0 & 0 \\ 0 & k_b & 0 & 0 & -k_u & 0 \\ 0 & 0 & k_b & 0 & 0 & -k_u \end{pmatrix}, \tag{4.14}$$

with D_1 and D_2 given by equation (4.9).

Theorem 3. Assume that the initial value problem (4.13) is used to describe the dynamics of fluorescent proteins in a FRAP experiment. If the FRAP data are presented normalized with respect to the expected final fluorescence intensity in the bleached region after recovery, then the following theoretical recovery curve can be used to fit the data:

$$F(t) = 1 - \gamma e^{\alpha t} - (1 - \gamma) e^{\beta t}, \tag{4.15}$$

where

$$\begin{aligned} \alpha &= -S_1 + S_2\,, \\ \beta &= -S_1 - S_2\,, \end{aligned} \tag{4.16}$$

and

$$\gamma = \frac{1}{2}\frac{k_b}{k_b+k_u}\frac{S_1+S_2}{S_2}\left(\frac{-S_1+S_2+k_u}{k_b}+1\right),$$

$$S_1 = \frac{k_b+k_u}{2}+\frac{D_t}{2-r}, \tag{4.17}$$

$$S_2 = \sqrt{\left(\frac{k_b+k_u}{2}+\frac{D_t}{2-r}\right)^2 - 2\frac{k_u D_t}{2-r}}\,.$$

Proof. To find a theoretical recovery curve based on the initial-value problem (4.13), we first need the solution of (4.13). We start by proving that the eigenvalues of the matrix A are distinct and real. The eigenvalues of A are determined by the roots of its characteristic polynomial $p(\lambda) = \det(A - \lambda I)$. Calculating this determinant, we obtain that

$$p(\lambda) = \frac{1}{(r-2)^2}\lambda\,(\lambda + k_b + k_u)\,p_1(\lambda)\,p_2(\lambda)\,, \tag{4.18}$$

where

$$p_1(\lambda) = (r-2)\lambda^2 + [(k_b+k_u)\,(r-2) - 2D_t]\,\lambda - 2\,k_u D_t\,, \tag{4.19}$$

$$p_2(\lambda) = (r-2)\lambda^2 + [(k_b+k_u)\,(r-2) + 2(r-1)D_t]\,\lambda + 2(r-1)k_u D_t\,. \tag{4.20}$$

Thus, the eigenvalues of A are given by

$$\begin{aligned} &\lambda_1 = 0\,, && \lambda_2 = -S_1 + S_2\,, && \lambda_3 = -S_1 - S_2\,, \\ &\lambda_4 = -(k_b+k_u)\,, && \lambda_5 = -R_1 + R_2\,, && \lambda_6 = -R_1 - R_2\,, \end{aligned} \tag{4.21}$$

where λ_2 and λ_3 are the roots of $p_1(\lambda)$, λ_5 and λ_6 are the roots of $p_2(\lambda)$, S_1 and S_1 are as given in (4.17), and

$$R_1 = \frac{k_b+k_u}{2}+\frac{1-r}{2-r}D_t\,,$$

$$R_2 = \sqrt{\left(\frac{k_b+k_u}{2}+\frac{1-r}{2-r}D_t\right)^2 - 2\frac{1-r}{2-r}k_u D_t}\,. \tag{4.22}$$

Note that S_2 and R_2 can be rewritten as

$$S_2 = \sqrt{\frac{k_b^2}{4} + k_b\left(\frac{k_u}{2} + \frac{D_t}{2-r}\right) + \left(\frac{k_u}{2} - \frac{D_t}{2-r}\right)^2}, \tag{4.23}$$

$$R_2 = \sqrt{\frac{k_b^2}{4} + k_b\left(\frac{k_u}{2} + \frac{1-r}{2-r}D_t\right) + \left(\frac{k_u}{2} - \frac{1-r}{2-r}D_t\right)^2}. \tag{4.24}$$

Thus, keeping in mind that $0 < r < 1$ (see equation (4.10)), we have $S_2, R_2 > 0$, and conclude that the eigenvalues (4.21) of the matrix A are distinct and real. This implies that the solution of the initial-value problem is given by a sum of exponentials [26, 39]. Specifically,

$$w(t) = \sum_{i=1}^{6} c_i\, z_i\, e^{\lambda_i t}, \tag{4.25}$$

where λ_i are the eigenvalues of A, given by equation (4.21), z_i denote their corresponding eigenvectors, and the constants c_i depend on the initial condition (4.11). To find the eigenvectors z_i, we solve the equation

$$(A - \lambda_i I)\, z_i = 0 \tag{4.26}$$

for each of the eigenvalues λ_i of A. By doing so, we obtain

(4.27)

$$z_1 = \left(2\frac{1-r}{r},\ 1,\ 1,\ 2\frac{k_b}{k_u}\frac{1-r}{r},\ \frac{k_b}{k_u},\ \frac{k_b}{k_u}\right)^T,$$

$$z_2 = \left(2\frac{S_1 - S_2 - k_u}{k_b},\ \frac{-S_1 + S_2 + k_u}{k_b},\ \frac{-S_1 + S_2 + k_u}{k_b},\ -2,\ 1,\ 1\right)^T,$$

$$z_3 = \left(2\frac{S_1 + S_2 - k_u}{k_b},\ \frac{-S_1 - S_2 + k_u}{k_b},\ \frac{-S_1 - S_2 + k_u}{k_b},\ -2,\ 1,\ 1\right)^T,$$

$$z_4 = \left(-2\frac{1-r}{r},\ -1,\ -1,\ 2\frac{1-r}{r},\ 1,\ 1\right)^T,$$

$$z_5 = \left(0,\ \frac{R_1 - R_2 - k_u}{k_b},\ \frac{-R_1 + R_2 + k_u}{k_b},\ 0,\ -1,\ 1\right)^T,$$

$$z_6 = \left(0,\ \frac{R_1 + R_2 - k_u}{k_b},\ \frac{-R_1 - R_2 + k_u}{k_b},\ 0,\ -1,\ 1\right)^T.$$

To find the constants c_i, we evaluate the solution $\boldsymbol{w}(t)$ at $t = 0$, and obtain

$$\boldsymbol{w}(0) = \sum_{i=1}^{6} c_i \boldsymbol{z}_i = \boldsymbol{w}_0 \,. \tag{4.28}$$

In other words, we can find $\overline{c} = (c_1, c_2, c_3, c_4, c_5, c_6)^T$ by solving the equation

$$Z\overline{c} = \boldsymbol{w}_0 \,, \tag{4.29}$$

where Z is the 6×6 matrix whose columns are the eigenvectors $\boldsymbol{z}_i$ of A,

$$Z = \Big(\boldsymbol{z}_1 \mid \boldsymbol{z}_2 \mid \boldsymbol{z}_3 \mid \boldsymbol{z}_4 \mid \boldsymbol{z}_5 \mid \boldsymbol{z}_6 \Big) \,, \tag{4.30}$$

and $\boldsymbol{w}_0$ is as in (4.13). Thus, solving (4.29) we obtain

$$\overline{c} = \left(\frac{k_u}{k_b + k_u} \frac{r^2}{2}, \frac{k_b}{k_b + k_u} \frac{S_1 + S_2}{S_2} \frac{(1-r)r}{4}, \frac{k_b}{k_b + k_u} \frac{-S_1 + S_2}{S_2} \frac{(1-r)r}{4}, 0, 0, 0 \right)^T . \tag{4.31}$$

Substitution of λ_i (equation (4.21)), $\boldsymbol{z}_i$ (equation (4.27)), and c_i (equation (4.31)), for $i = 1, \ldots, 6$, into (4.25) leads to the following solution for the initial-value problem (4.13):

$$\boldsymbol{w}(t) = c_1 \boldsymbol{z}_1 + c_2 \boldsymbol{z}_2 e^{\lambda_2 t} + c_3 \boldsymbol{z}_3 e^{\lambda_3 t} \,. \tag{4.32}$$

Note that the solution (4.32) involves only two exponentials, which is a consequence of the zero eigenvalue in (4.21) and the specific initial conditions that lead to the three zeroes in (4.31).

To see how the solution $\boldsymbol{w}(t)$ of the initial-value problem allows us to find a theoretical recovery curve, we note that the fluorescence recovery in the photobleached region is described by the dynamics in the compartment C_0 (figure 4.1), i.e., by

$$R(t) = u_0(t) + v_0(t) \,. \tag{4.33}$$

Using the fact that $u_0(t)$ and $v_0(t)$ are the first and fourth components of $\boldsymbol{w}(t)$ (equation (4.32)), we can rewrite equation (4.33) as

$$R(t) = \tilde{c}_1 - \tilde{c}_2 e^{\lambda_2 t} - \tilde{c}_3 e^{\lambda_3 t} \,, \tag{4.34}$$

where

$$
\begin{aligned}
\tilde{c}_1 &= r\,(1-r)\,, \\
\tilde{c}_2 &= \frac{r(1-r)}{2}\,\frac{k_b}{k_b+k_u}\,\frac{S_1+S_2}{S_2}\left(\frac{-S_1+S_2+k_u}{k_b}+1\right), \\
\tilde{c}_3 &= \frac{r(1-r)}{2}\,\frac{k_b}{k_b+k_u}\,\frac{-S_1+S_2}{S_2}\left(\frac{-S_1-S_2+k_u}{k_b}+1\right).
\end{aligned}
\tag{4.35}
$$

By assumption, the experimental FRAP data is presented normalized with respect to the expected final fluorescence intensity in the bleached region after recovery. Thus, we normalize (4.34) by dividing it by $r(1-r)$, and obtain the following appropriate theoretical fluorescence recovery:

$$
F(t) = 1 - c_2^*\, e^{\lambda_2 t} - c_3^*\, e^{\lambda_3 t}\,,
\tag{4.36}
$$

where

$$
\begin{aligned}
c_2^* &= \frac{\tilde{c}_2}{r\,(1-r)} = \frac{1}{2}\,\frac{k_b}{k_b+k_u}\,\frac{S_1+S_2}{S_2}\left(\frac{-S_1+S_2+k_u}{k_b}+1\right), \\
c_3^* &= \frac{\tilde{c}_3}{r\,(1-r)} = \frac{1}{2}\,\frac{k_b}{k_b+k_u}\,\frac{-S_1+S_2}{S_2}\left(\frac{-S_1-S_2+k_u}{k_b}+1\right).
\end{aligned}
\tag{4.37}
$$

Apparently, if we were to fit the theoretical recovery (4.36) to a set of FRAP data, four parameters instead of three should be estimated. However, notice that an expansion of the expression $c_2^* + c_3^*$ yields the following:

$$
\begin{aligned}
c_2^* + c_3^* &= \frac{1}{2}\,\frac{1}{k_b+k_u}\,\frac{1}{S_2}\,[\,(S_1+S_2)\,(-S_1+S_2+k_u+k_b)+ \\
&\qquad (-S_1+S_2)\,(-S_1-S_2+k_u+k_b)\,] \\
&= \frac{1}{2}\,\frac{1}{k_b+k_u}\,\frac{1}{S_2}\,[\,2S_2\,(k_u+k_b)\,] \\
&= 1\,.
\end{aligned}
\tag{4.38}
$$

Therefore, denoting $\alpha = \lambda_2$, $\beta = \lambda_3$, and $\gamma = c_2^*$, the theoretical fluorescence recovery (4.36) can be rewritten as expression (4.15), which only involves three parameters. This completes the proof. □

From theorem 3, we conclude that the use of the compartmental model (4.1) to interpret FRAP data provides a simple exponential sum for the theoretical fluorescence recovery curve (equation (4.15)). The simplicity of this curve offers experimentalists a straightforward approach to quantify FRAP data, and simplifies the task of parameter estimation.

4.3 Parameter Estimation Methodology and Application to Nuclear Actin Dynamics

There are three dynamical parameters to be estimated when interpreting FRAP data using the compartmental model (4.1), namely the binding rate, k_b, the unbinding rate, k_u, and the diffusional transfer coefficient, D_t. However, the theoretical recovery curve given by equation (4.15) is expressed in terms of three new parameters, namely, α, β, and γ. These new parameters are, indeed, functions of the diffusional transfer coefficient, and the binding and unbinding rates (equations (4.16) and (4.17)). Thus, one could substitute these corresponding functions into (4.15), and obtain a theoretical recovery curve in terms of the original parameters that can be used to fit the data. Instead of doing that, we take advantage of the exponential sum in the recovery curve, and we propose the following procedure, requiring little computer capability to estimate the dynamical parameters:

1. Normalize the FRAP data with respect to the expected final fluorescence intensity in the bleached region after recovery, $F_a\,(1 - F_a/F_0)$ (see equation (2.47)).

2. Using the method of nonlinear least squares, fit the theoretical recovery curve given by the exponential sum (4.15) to the FRAP data, and obtain estimates for α, β, and γ.

3. Obtain estimates for S_1 and S_2 by solving the linear system (4.16), namely

$$\begin{aligned} S_1 &= \frac{-\alpha - \beta}{2}, \\ S_2 &= \frac{\alpha - \beta}{2}. \end{aligned} \tag{4.39}$$

4. Substitute the estimated values of S_1 and S_2 into the equations given by (4.17) and, using any numerical scheme for solving systems of nonlinear equations, solve the nonlinear system (4.17) in order to obtain estimates of the dynamical parameters D_t, k_b, and k_u.

For the purpose of illustrating this parameter estimation methodology, the compartmental model (4.1) is applied to the dynamics of nuclear actin. Two populations of nuclear actin are considered, namely a mobile population of globular actin free to diffuse, and an immobile filamentous population. The objective, as in section 3.3.2, is to find estimates for the sizes of the filamentous and globular nuclear actin pools.

Following the notation of the compartmental model (4.1), the two populations of nuclear actin occupy three physical compartments during a FRAP experiment in the cell nucleus, namely the photobleached region C_0, the left unbleached region C_1, and the right unbleached region C_2 (figure 4.1A). Thus, u_0, u_1, and u_2 represent the populations of diffusing globular actin in C_0, C_1, and C_2, respectively, v_0, v_1, and v_2 represent the immobile filamentous population of actin in C_0, C_1, and C_2, respectively, k_b is the association rate of globular actin to the filamentous pool, k_u is the dissociation rate of globular actin from the filamentous pool, and D_t is the diffusional transfer coefficient of nuclear actin.

We employ the above parameter estimation methodology to interpret the FRAP data presented in chapter 2 (figure 2.8), and chapter 3 (figure 3.2). The data already is normalized with respect to the expected final fluorescence intensity in the bleached region after recovery. Thus, by fitting the theoretical recovery curve given by the exponential sum (4.15) to the FRAP data (figure 4.2), we obtain the following estimates:

$$\alpha = 0.0131\,\mathrm{s}^{-1}, \quad \beta = 0.6568\,\mathrm{s}^{-1}, \quad \gamma = 0.1802\,. \tag{4.40}$$

These estimates are substituted into the linear system (4.16), which is solved to obtain

$$S_1 = 0.33495\,\mathrm{s}^{-1}, \quad S_2 = 0.32185\,\mathrm{s}^{-1}. \tag{4.41}$$

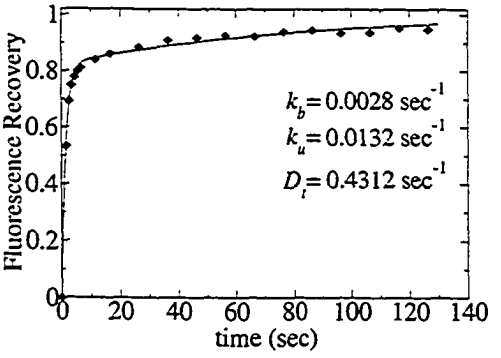

Figure 4.2: GFP-actin FRAP data (diamonds) are fitted with the theoretical recovery curve (4.15) (solid curve). From the fitting, estimates for the diffusional transfer coefficient, $D_t = 0.4312\,\mathrm{s}^{-1}$, the association rate, $k_b = 0.0028\,\mathrm{s}^{-1}$, and the dissociation rate, $k_u = 0.0132\,\mathrm{s}^{-1}$, are obtained. Notice from figure 3.2 that these estimates are of the same order of magnitude and very close to the ones obtained using the reaction-diffusion system (3.1).

Finally, by substituting the values of S_1 and S_2 given by equation (4.41) into the nonlinear system (4.17), and solving it, estimates for

$$D_t = 0.4312\,\mathrm{s}^{-1}, \quad k_b = 0.0028\,\mathrm{s}^{-1}, \quad k_u = 0.0132\,\mathrm{s}^{-1}, \tag{4.42}$$

are obtained.

As shown in figure 4.2, the fitting describes quite accurately the fast and slow phases of the recovery, corresponding to the fast diffusion and the turnover of globular actin into the immobile filamentous population. From the fitting, we obtain the following quantitative information of actin in the nucleus:

- $P_b = \dfrac{k_b}{k_b + k_u} = 0.17$: the proportion of nuclear actin in filamentous form,
- $P_u = \dfrac{k_u}{k_b + k_u} = 0.83$: the proportion of nuclear actin in globular form,
- $\tau_r = \dfrac{1}{k_u} \approx 76\,\mathrm{sec}$: the average residence time of nuclear actin in filamentous form,
- $\tau_w = \dfrac{1}{k_b} \approx 363\,\mathrm{sec}$: the average wandering time of nuclear actin between associations to filaments.

Notice from figure 3.2 that these estimates of the proportions of nuclear actin in globular and filamentous form, respectively, coincide, with a difference of less than 1%, from the estimates obtained in section 3.3.2 using the reaction-diffusion system (3.1).

Two aspects related to the estimated parameters are worth mentioning. First, there seems to be a close relationship between the estimated proportion of nuclear actin in filamentous form, P_b, and the estimated value for γ. Second, there seems to be a relationship between the dissociation rate k_u and the estimated value for α. These relationships will become apparent in chapter 5.

4.4 Discussion

In this chapter, we have derived another theoretical recovery curve that can be used for the interpretation of FRAP data. This theoretical recovery curve, given by equation (4.15), is derived from the compartmental model (4.1). We used it to analyze FRAP data of nuclear actin that also were analyzed with the theoretical recoveries derived from the diffusion equation (2.3) and the reaction-diffusion equation (3.1).

The variety of ways that we have employed so far to analyze the same set of data (for example, the nuclear actin FRAP data) leads to the conclusion that the specific theoretical recovery curve to be used for fitting depends on the criteria and needs of the particular experiment. In particular, if the main concern is the estimation of binding (association) and unbinding (dissociation) rates, then one can take advantage of the simplicity of equation (4.15) (a simple exponential sum) and use the compartmental model for the fitting. On the other hand, if one also is interested in the estimation of a diffusion coefficient, the theoretical recovery curve (3.4), coming from the reaction-diffusion model (3.1), may be more appropriate. However, the theoretical recovery curve (3.4) is not as simple as the theoretical recovery curve (4.15). The exponential sum that characterizes the latter simplifies the task of parameter estimation through the introduction of three new parameters (α, β and γ in equation (4.15)), and provides the experimentalists with a very

simple approach to analyze FRAP data. Nevertheless, the apparent tradeoff for the simplicity is that the compartmental model does not offer a straightforward estimation of a diffusion coefficient. In chapter 5, we will discuss how we can obtain an estimate of a diffusion coefficient from the compartmental model; in other words, we will discuss the relationship between the compartmental model (4.1) and the reaction-diffusion model (3.1).

Despite the simplicity of the exponential sum in the theoretical recovery curve (4.15), it is difficult to assign a biological meaning to the parameters α, β and γ just from their expressions in terms of the original parameters k_b, k_u, and D_t. However, from the application of the compartmental model to the dynamics of nuclear actin, one suspects that α should coincide with the dissociation rate k_u, and γ should coincide with the immobile pool P_b, at least when the FRAP data exhibits a biphasic behaviour. This suspicion will be confirmed in chapter 5.

Explicit solutions for the compartmental model (4.1) and the reaction-diffusion equation (3.1) have resulted in theoretical recovery curves that can be used to fit experimental FRAP data for nuclear proteins undergoing a reversible binding-unbinding process. However, the relationship between the expressions of these theoretical recovery curves and the different qualitative behaviours that can be exhibited by experimental fluorescence recoveries is not apparent. This issue is the main topic of chapter 5, where we will find simpler theoretical recovery curves that not only reflect the behaviour of FRAP data, but simplify the task of parameter estimation even further.

Chapter 5

Characterizing FRAP Curves Using Perturbation Analysis

In both chapter 3 and chapter 4, we examine two models that incorporate the assumption that fluorescent proteins undergo binding and unbinding events with an approximate spatially homogeneous structure, namely the reaction-diffusion model (3.1), and the compartmental model (4.1). Although explicit solutions for these two models were found, the theoretical recovery curves obtained from them offer very little in terms of characterizing the different types of behaviour of experimental FRAP data. Thus, the present chapter will focus on providing a simple and comprehensive characterization of the fluorescence recovery curves for biomolecules whose dynamics are described by models (3.1) and (4.1).

When the dynamics of the fluorescent proteins are governed by both diffusion and binding-unbinding events, the fluorescence recovery data can exhibit distinguished qualitative types of behaviour depending on the relative magnitude of the parameters k_b and k_u in models (3.1) and (4.1) [9]. We will classify these types of behaviour into limiting cases, and analyze them using perturbation theory.

The first case (section 5.1) will cover the trivial behaviour, in which the bound population can be neglected, and the recovery curve is produced simply by a diffusive population. The second case (section 5.2) will explain the overall reduced mobility or

reduced diffusive behaviour, in which the recovery, influenced by rapid association and dissociation events, looks like the one produced by a single slower diffusing population. And the third case (section 5.3) will describe how fluorescence recovery curves can present a biphasic behaviour, distinguished by a fast phase and a slow phase, and caused by binding events which are slow relative to the diffusion process.

For each of these cases, we carry out a perturbation analysis in which finite series expansions are considered, and find their corresponding leading-order terms.

The perturbation analysis will not only offer a characterization of the fluorescence recovery curves for nuclear proteins undergoing binding-unbinding events, but will simplify, whenever possible, the task of parameter estimation by providing simple expressions for fitting the experimental data [9].

Furthermore, since both models (3.1) and (4.1) aim to describe the same dynamics with slightly different approaches, we will show, in section 5.4, how they can be related in order to find a common ground between them. In section 5.5, the results are applied to quantify the dynamics or two nuclear proteins, namely actin and histone H1. We conclude with a discussion in section 5.6.

5.1 Trivial Behaviour

Assume that $k_b = \varepsilon\,\gamma_b \ll k_u$, where $\varepsilon \ll 1$. This means that the proportion of bound fluorescent population $\dfrac{k}{1+k}$, where $k = \dfrac{k_b}{k_u}$, can be neglected, and one would expect only diffusion to play a role in the fluorescence recovery.

Reaction-diffusion model

We rewrite the reaction-diffusion system (3.1) in terms of ε:

$$
\begin{aligned}
&\frac{\partial}{\partial t}u(x,t) = D\,\frac{\partial^2}{\partial x^2}u(x,t) - \varepsilon\gamma_b u(x,t) + k_u v(x,t)\,, && x\in(0,l)\,, \quad t>0\,,\\
&\frac{\partial}{\partial t}v(x,t) = \varepsilon\gamma_b u(x,t) - k_u v(x,t)\,, && x\in(0,l)\,, \quad t>0\,,\\
&\frac{\partial u}{\partial x} = \frac{\partial v}{\partial x} = 0 && x = 0, l\,, \quad t>0\,,\\
&u(x,0) = f(x)\,, \quad v(x,0) = g(x)\,, && x\in(0,l)\,,
\end{aligned}
\tag{5.1}
$$

where the initial conditions $f(x)$ and $g(x)$, given respectively by (3.2) and (3.3), can be expressed in terms of ε as follows,

$$f(x) = \begin{cases} 0\,, & |x-c| \le h\,, \\ \dfrac{k_u}{\varepsilon\gamma_b + k_u}\,, & |x-c| > h\,, \end{cases} \tag{5.2}$$

and

$$g(x) = \begin{cases} 0\,, & |x-c| \le h\,, \\ \dfrac{\varepsilon\gamma_b}{\varepsilon\gamma_b + k_u}\,, & |x-c| > h\,. \end{cases} \tag{5.3}$$

By considering the series expansion in ε up to order $N > 2$ of the solution (u, v) of the problem (5.1)

$$u(x,t) = \sum_{n=0}^{N} \varepsilon^n u_n(x,t)\,, \qquad v(x,t) = \sum_{n=0}^{N} \varepsilon^n v_n(x,t)\,, \tag{5.4}$$

the following leading-order problem is obtained:

$$\begin{aligned} &\frac{\partial}{\partial t}u_0(x,t) = D\frac{\partial^2}{\partial x^2}u_0(x,t) + k_u v_0(x,t)\,, && x \in (0,l)\,, \quad t > 0\,, \\ &\frac{\partial}{\partial t}v_0(x,t) = -k_u v_0(x,t)\,, && x \in (0,l)\,, \quad t > 0\,, \\ &\frac{\partial u_0}{\partial x} = \frac{\partial v_0}{\partial x} = 0 && x = 0, l\,, \quad t > 0\,, \\ &u_0(x,0) = f(x)\,, \quad v_0(x,0) = g(x)\,, && x \in (0,l)\,, \end{aligned} \tag{5.5}$$

where the initial conditions are given by

$$g(x) = 0\,, \qquad f(x) = \begin{cases} 0\,, & |x-c| \le h\,, \\ 1\,, & |x-c| > h\,. \end{cases} \tag{5.6}$$

Equations (5.5) and (5.6) imply that $v_0(x,t) = 0$ for all $t \ge 0$, and hence the dynamics of the total population $c(x,t) = u(x,t) + v(x,t)$ in equation (3.1) can be approximated by the simple diffusion equation

$$\begin{aligned} &\frac{\partial}{\partial t}c(x,t) = D\frac{\partial^2}{\partial x^2}c(x,t)\,, && x \in (0,l)\,, \quad t > 0\,, \\ &\frac{\partial c}{\partial x} = 0 && x = 0, l\,, \quad t > 0\,, \\ &c(x,0) = f(x)\,, && x \in (0,l)\,, \end{aligned} \tag{5.7}$$

where the initial condition $f(x)$ is given by equation (5.6). By integrating the solution of equation (5.7) over the photobleached region, subject to the initial condition (5.6), the corresponding normalized recovery curve can be approximated by

$$F(t) \sim 1 - \frac{l^2}{h(l-2h)} \sum_{n=1}^{\infty} \exp\left(-\frac{n^2\pi^2 D}{l^2}\, t\right) S_n^2 \,, \tag{5.8}$$

where S_n is as in equation (3.5).

Compartmental model

Rewriting the compartmental model (4.1), subject to the initial condition (4.11), in terms of ε, we obtain

$$\begin{aligned}
\dot{u}_0 &= -2D_1 u_0 + D_2 u_1 + D_2 u_2 - \varepsilon\gamma_b u_0 + k_u v_0 \,, \\
\dot{u}_1 &= D_1 u_0 - D_2 u_1 - \varepsilon\gamma_b u_1 + k_u v_1 \,, \\
\dot{u}_2 &= D_1 u_0 - D_2 u_2 - \varepsilon\gamma_b u_2 + k_u v_2 \,, \\
\dot{v}_0 &= \varepsilon\gamma_b u_0 - k_u v_0 \,, \\
\dot{v}_1 &= \varepsilon\gamma_b u_1 - k_u v_1 \,, \\
\dot{v}_2 &= \varepsilon\gamma_b u_2 - k_u v_2 \,,
\end{aligned} \tag{5.9}$$

subject to the initial condition

$$(u_0, u_1, u_2, v_0, v_1, v_2)_{(0)} = \left(0, \frac{k_u}{\varepsilon\gamma_b + k_u}\frac{r}{2}, \frac{k_u}{\varepsilon\gamma_b + k_u}\frac{r}{2}, 0, \frac{\varepsilon\gamma_b}{\varepsilon\gamma_b + k_u}\frac{r}{2}, \frac{\varepsilon\gamma_b}{\varepsilon\gamma_b + k_u}\frac{r}{2}\right) \,, \tag{5.10}$$

where r is as in equation (4.10).

By considering the series expansion in ε up to order $N > 2$ of the solution $(u_0, u_1, u_2, v_0, v_1, v_2)$ of the problem (5.9)

$$\begin{aligned}
u_0(t) &= \sum_{n=0}^{N} \varepsilon^n u_{0n}(t) \,, \qquad u_1(t) = \sum_{n=0}^{N} \varepsilon^n u_{1n}(t) \,, \qquad u_2(t) = \sum_{n=0}^{N} \varepsilon^n u_{2n}(t) \,, \\
v_0(t) &= \sum_{n=0}^{N} \varepsilon^n v_{0n}(t) \,, \qquad v_1(t) = \sum_{n=0}^{N} \varepsilon^n v_{1n}(t) \,, \qquad v_2(t) = \sum_{n=0}^{N} \varepsilon^n v_{2n}(t) \,,
\end{aligned} \tag{5.11}$$

the following leading-order problem is obtained:

$$
\begin{aligned}
\dot{u}_{00} &= -2D_1 u_{00} + D_2 u_{10} + D_2 u_{20} + k_u v_{00} \,, \\
\dot{u}_{10} &= D_1 u_{00} - D_2 u_{10} + k_u v_{10} \,, \\
\dot{u}_{20} &= D_1 u_{00} - D_2 u_{20} + k_u v_{20} \,, \\
\dot{v}_{00} &= -k_u v_{00} \,, \\
\dot{v}_{10} &= -k_u v_{10} \,, \\
\dot{v}_{20} &= -k_u v_{20} \,,
\end{aligned}
\tag{5.12}
$$

subject to the initial condition

$$
(u_{00}, u_{10}, u_{20}, v_{00}, v_{10}, v_{20})_{(0)} = \left(0, \frac{r}{2}, \frac{r}{2}, 0, 0, 0\right) \,. \tag{5.13}
$$

The last three equations in (5.12) and the initial condition (5.13) imply that

$$
(v_{00}, v_{10}, v_{20}) = (0, 0, 0) \,, \tag{5.14}
$$

and hence the dynamics of the total population $c(t) = (c_0(t), c_1(t), c_2(t)) = (u_0(t) + v_0(t), u_1(t) + v_1(t), u_2(t) + v_2(t))$ in the compartmental model (4.1) are governed by the simple diffusional compartmental model

$$
\begin{aligned}
\dot{c}_0 &= -2D_1 c_0 + D_2 c_1 + D_2 c_2 \,, \\
\dot{c}_1 &= D_1 c_0 - D_2 c_1 \,, \\
\dot{c}_2 &= D_1 c_0 - D_2 c_2 \,,
\end{aligned}
\tag{5.15}
$$

with an initial condition

$$
(c_0, c_1, c_2)_{(0)} = (0, r/2, r/2) \,. \tag{5.16}
$$

By normalizing the solution c_0, one obtains the following approximation for the recovery curve

$$
F(t) \sim 1 - \exp\left(-\frac{2\,D_t}{2 - r}\, t\right) \,. \tag{5.17}
$$

Note that the recovery curves (5.8) and (5.17) account only for the effect of the diffusion, since the bound population is being neglected, and they do so by means

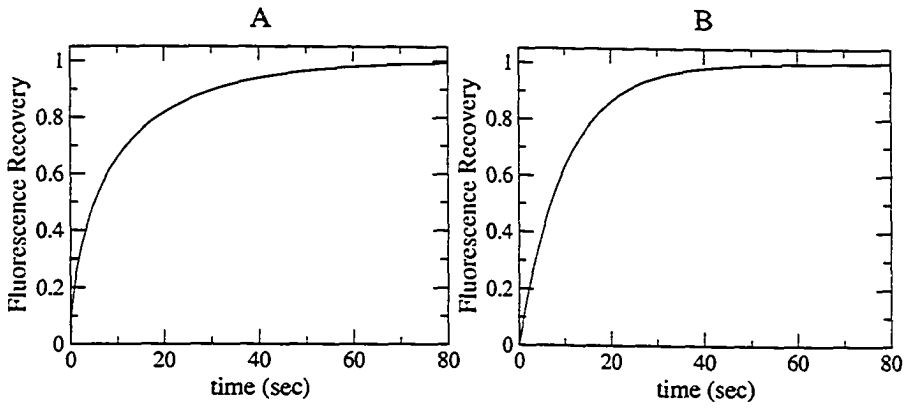

Figure 5.1: A: Simulated recovery curve obtained from equation (5.8) with $D = 0.05\mu^2\,\mathrm{s}^{-1}$, $l = 6\mu$, and $h = 1\mu$. B: Simulated recovery curve obtained from equation (5.17) with $D_t = 0.05\mathrm{s}^{-1}$, and $r = 0.67$.

of two different parameters, namely the diffusion coefficient, D, and the diffusional transfer coefficient D_t (figure 5.1). We will develop a relationship between these two parameters in Section 5.4.

5.2 Reduced Diffusive Behaviour

Assume in this case that $k_b = \frac{\gamma_b}{\varepsilon}$, and $k_u = \frac{\gamma_u}{\varepsilon}$, where $\varepsilon \ll 1$. This assumption implies that both the average residence time of biomolecules in bound form, $\tau_r = \frac{1}{k_u}$, and the average time between binding events, $\tau_w = \frac{1}{k_b}$, are small. In other words, the turnover of bound biomolecules is fast. In the context of chemical kinetics, this type of reaction, in which an immobilized reactant forms very rapidly compared to the diffusion process, is called instantaneous reaction [16]. This type of rapid reaction also is studied by Hillen in [38] for a more general parabolic model with resting phase for which the reaction-diffusion model (3.1) is a special case.

Reaction-diffusion model

We will show that the fluorescence recovery curve obtained from the reaction-diffusion equation (3.1) can be approximated by the one produced by a single population moving randomly with an effective diffusion coefficient $D_{eff} = \frac{D}{1+k}$, where

$k = \frac{k_b}{k_u}$. Adding the first and second equations in (3.1), and using the assumptions that $k_b = \frac{\gamma_b}{\varepsilon}$ and $k_u = \frac{\gamma_u}{\varepsilon}$, the reaction-diffusion system (3.1) can be rewritten as

$$
\begin{aligned}
&\frac{\partial}{\partial t}(u(x,t)+v(x,t)) = D\frac{\partial^2}{\partial x^2}u(x,t)\,, && x\in(0,l)\,, \quad t>0\,,\\
&\varepsilon\frac{\partial}{\partial t}v(x,t) = \gamma_b u(x,t) - \gamma_u v(x,t)\,, && x\in(0,l)\,, \quad t>0\,,\\
&\frac{\partial u}{\partial x} = \frac{\partial v}{\partial x} = 0 && x = 0,l\,, \quad t>0\,,\\
&u(x,0) = f(x)\,, \quad v(x,0) = g(x)\,, && x\in(0,l)\,.
\end{aligned}
\tag{5.18}
$$

If we consider a series expansion in ε up to order $N > 2$ for $u(x,t)$ and $v(x,t)$ of the form

$$
u(x,t) = \sum_{n=0}^{N}\varepsilon^n u_n(x,t)\,, \qquad v(x,t) = \sum_{n=0}^{N}\varepsilon^n v_n(x,t)\,,
\tag{5.19}
$$

the leading-order system is

$$
\begin{aligned}
&\frac{\partial}{\partial t}(u_0(x,t)+v_0(x,t)) = D\frac{\partial^2}{\partial x^2}u_0(x,t)\,, && x\in(0,l)\,, \quad t>0\,,\\
&0 = \gamma_b u_0(x,t) - \gamma_u v_0(x,t)\,, && x\in(0,l)\,, \quad t>0\,,\\
&\frac{\partial u_0}{\partial x} = \frac{\partial v_0}{\partial x} = 0 && x = 0,l\,, \quad t>0\,,\\
&u_0(x,0) = f(x)\,, \quad v_0(x,0) = g(x)\,, && x\in(0,l)\,.
\end{aligned}
\tag{5.20}
$$

From the second equation in (5.20), we obtain the quasi-steady state relation $v_0(x,t) = ku_0(x,t)$. Substituting this into the first equation, we obtain

$$
\frac{\partial}{\partial t}u_0(x,t) = \frac{D}{1+k}\frac{\partial^2}{\partial x^2}u_0(x,t)\,, \qquad \frac{\partial}{\partial t}v_0(x,t) = \frac{D}{1+k}\frac{\partial^2}{\partial x^2}v_0(x,t)\,.
\tag{5.21}
$$

Therefore, the leading-order approximation $c_0(x,t) = u_0(x,t) + v_0(x,t)$ for the dynamics of the fluorescent population is governed by the diffusion equation

$$
\begin{aligned}
&\frac{\partial}{\partial t}c_0(x,t) = D_{eff}\frac{\partial^2}{\partial x^2}c_0(x,t)\,, && x\in(0,l)\,, \quad t>0\,,\\
&\frac{\partial c_0}{\partial x} = 0 && x = 0,l\,, \quad t>0\,,\\
&c_0(x,0) = h(x)\,, && x\in(0,l)\,,
\end{aligned}
\tag{5.22}
$$

where the initial condition is given by

$$h(x) = \begin{cases} 0, & |x-c| \leq h, \\ 1, & |x-c| > h, \end{cases} \tag{5.23}$$

and the effective diffusion coefficient is given by

$$D_{eff} = \frac{D}{1+k} < D\,. \tag{5.24}$$

Thus, the approximated recovery curve derived from system (3.1) when the turnover binding process is fast compared to the diffusion process is given by

$$F(t) \sim 1 - \frac{l^2}{h(l-2h)} \sum_{n=1}^{\infty} \exp\left(-\frac{n^2\pi^2}{l^2} D_{eff}\, t\right) S_n^2\,, \tag{5.25}$$

where S_n is given by equation (3.5).

Comparing this last expression to the one in (5.8) explains why the recovery curve produced by a fluorescent population moving randomly with a diffusion coefficient D, and interacting with a homogeneous immobile structure at a rapid turnover rate, would be similar to the one produced by a single population moving randomly with an effective diffusion D_{eff} that has been reduced by a factor equal to the proportion of unbound population (figure 5.2A).

Compartmental model

Analogously, we will show that the fluorescence recovery curve obtained from the compartmental model (4.1) can be approximated by the one produced by a single population whose movement is characterized by an effective diffusional transfer coefficient $(D_t)_{eff} = \frac{D_t}{1+k}$, where $k = \frac{k_b}{k_u}$.

By adding the bound and free populations in each of the compartmentments, and using the assumptions that $k_b = \frac{\gamma_b}{\varepsilon}$ and $k_u = \frac{\gamma_u}{\varepsilon}$, we can rewrite the compart-

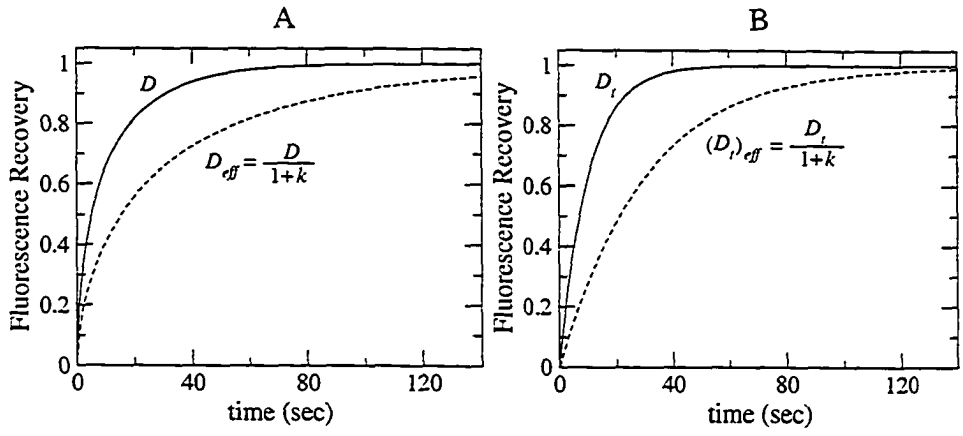

Figure 5.2: A: The solid curve is the simulated recovery curve of a fluorescent population moving randomly with a diffusion coefficient $D = 0.05\mu\text{m}^2/\text{s}$ (equation (5.8) with $l = 6\mu$, and $h = 1\mu$), and the dashed curve is the simulated recovery curve of the same population that interacts at a rapid turnover rate with a homogeneous immobile structure, and has steady-state proportion $\frac{1}{1+k} = \frac{1}{3}$ of diffusing biomolecules. The dashed curve is equivalent to a recovery curve obtained from a population just moving randomly with an effective diffusion coefficient $D_{eff} = \frac{D}{1+k} = \frac{0.05}{3}\mu\text{m}^2/\text{s}$ (equation (5.25)). B: The solid curve is the simulated recovery curve obtained when modeling a diffusing population with the compartmental model (equation (5.15) with $D_t = 0.05\text{s}^{-1}$ and $r = 0.67$), and the dashed curve is the same population that interacts at a rapid turnover rate with a homogeneous immobile structure, and that has a steady state proportion $\frac{1}{1+k} = \frac{1}{3}$ of diffusing biomolecules (equation (5.35)).

mental model (4.1) as

$$
\begin{aligned}
\dot{u}_0 + \dot{v}_0 &= -2D_1u_0 + D_2u_1 + D_2u_2\,, \\
\dot{u}_1 + \dot{v}_1 &= D_1u_0 - D_2u_1\,, \\
\dot{u}_2 + \dot{v}_2 &= D_1u_0 - D_2u_2\,, \\
\varepsilon\dot{v}_0 &= \gamma_b u_0 - \gamma_u v_0\,, \\
\varepsilon\dot{v}_1 &= \gamma_b u_1 - \gamma_u v_1\,, \\
\varepsilon\dot{v}_2 &= \gamma_b u_2 - \gamma_u v_2\,.
\end{aligned}
\tag{5.26}
$$

Considering a series expansion in ε up to order $N > 2$ for the solution $(u_0, u_1, u_2, v_0, v_1, v_2)$

of the form

(5.27)

$$u_0(t) = \sum_{n=0}^{N} \varepsilon^n u_{0n}(t) , \qquad u_1(t) = \sum_{n=0}^{N} \varepsilon^n u_{1n}(t) , \qquad u_2(t) = \sum_{n=0}^{N} \varepsilon^n u_{2n}(t) ,$$

$$v_0(t) = \sum_{n=0}^{N} \varepsilon^n v_{0n}(t) , \qquad v_1(t) = \sum_{n=0}^{N} \varepsilon^n v_{1n}(t) , \qquad v_2(t) = \sum_{n=0}^{N} \varepsilon^n v_{2n}(t) ,$$

the leading-order approximation yields the quasi-steady state relations

$$v_{00} = k u_{00} , \qquad v_{10} = k u_{10} , \qquad v_{20} = k u_{20} , \tag{5.28}$$

and

$$\begin{aligned} (1+k)\dot{u}_{00} &= -2D_1 u_{00} + D_2 u_{10} + D_2 u_{20} , \\ (1+k)\dot{u}_{10} &= D_1 u_{00} - D_2 u_{10} , \\ (1+k)\dot{u}_{20} &= D_1 u_{00} - D_2 u_{20} . \end{aligned} \tag{5.29}$$

In other words, the leading-order system is given by

$$\begin{aligned} \dot{u}_{00} &= -2\frac{D_1}{1+k} u_{00} + \frac{D_2}{1+k} u_{10} + \frac{D_2}{1+k} u_{20} , \\ \dot{u}_{10} &= \frac{D_1}{1+k} u_{00} - \frac{D_2}{1+k} u_{10} , \\ \dot{u}_{20} &= \frac{D_1}{1+k} u_{00} - \frac{D_2}{1+k} u_{20} , \\ \dot{v}_{00} &= -2\frac{D_1}{1+k} v_{00} + \frac{D_2}{1+k} v_{10} + \frac{D_2}{1+k} v_{20} , \\ \dot{v}_{10} &= \frac{D_1}{1+k} v_{00} - \frac{D_2}{1+k} v_{10} , \\ \dot{v}_{20} &= \frac{D_1}{1+k} v_{00} - \frac{D_2}{1+k} v_{20} , \end{aligned} \tag{5.30}$$

subject to the initial condition

$$(u_{00}, u_{10}, u_{20}, v_{00}, v_{10}, v_{20})_{(0)} = \left(0, \frac{1}{1+k}\frac{r}{2}, \frac{1}{1+k}\frac{r}{2}, 0, \frac{k}{1+k}\frac{r}{2}, \frac{k}{1+k}\frac{r}{2}\right) . \tag{5.31}$$

Thus, we conclude the dynamics of the total population $c(t) = (c_0(t), c_1(t), c_2(t)) = (u_0(t) + v_0(t), u_1(t) + v_1(t), u_2(t) + v_2(t))$ in the compartmental model (4.1) can be

approximated by the following diffusional compartmental model:

$$
\begin{aligned}
\dot{c}_0 &= -2\frac{D_1}{1+k}\,c_0 + \frac{D_2}{1+k}\,c_1 + \frac{D_2}{1+k}\,c_2\,, \\
\dot{c}_1 &= \frac{D_1}{1+k}\,c_0 - \frac{D_2}{1+k}\,c_1\,, \\
\dot{c}_2 &= \frac{D_1}{1+k}\,c_0 - \frac{D_2}{1+k}\,c_2\,,
\end{aligned}
\tag{5.32}
$$

subject to the initial condition

$$
(c_0, c_1, c_2)_{(0)} = (0, r/2, r/2)\,. \tag{5.33}
$$

This means that when the turnover binding process is fast, the dynamics of system (4.1) are determined by an effective diffusional transfer coefficient

$$
(D_t)_{eff} = \frac{D_t}{1+k} < D_t\,, \tag{5.34}
$$

and the approximated recovery curve is slowed down by a factor equal to the proportion of unbound population (figure 5.2B), i.e.,

$$
F(t) \sim 1 - \exp\left[-\frac{2}{(2-r)}(D_t)_{eff}\,t\right]\,. \tag{5.35}
$$

It is worthwhile to mention that the technique of adding the two subpopulations (bound and unbound) in each of the compartments readily allowed us to distinguish the first three equations of (5.26) as the limiting system that determines the dynamics of the model when ε goes to zero. The same technique is applied by Hadeler and Hillen in [29] in order to obtain a limiting system of diffusive coupled systems when the sum of the coupling constants is big.

5.3 Biphasic Behaviour

In contrast to the previous case, we now assume that $k_b = \varepsilon\gamma_b$, and $k_u = \varepsilon\gamma_u$, where $\varepsilon \ll 1$, which implies that both the average residence time of biomolecules in bound form, $\tau_r = \frac{1}{k_u}$, and the average time between binding events, $\tau_w = \frac{1}{k_b}$, are large. This strength of binding will cause a slow turnover process compared with the diffusion process.

Using boundary layer theory [2], we show that the resulting fluorescence recovery curve exhibits two phases in time. The initial phase or inner recovery, characterized by a fast time scale and determined solely by the diffusion process, is obtained by approximating the solutions of (3.1) and (4.1) for a fast time scale, i.e., by finding inner solutions in time, whereas the last phase of the recovery or outer recovery, characterized by a slow time scale and determined by the turnover process, is obtained by approximating the solutions of (3.1) and (4.1) for a slow time scale, i.e., by finding outer solutions in time. In what follows, we present the leading-order inner and outer solutions for the reaction-diffusion equation (3.1) and the compartmental model (4.1), and match them to find an approximate solution for the fluorescence recovery curve.

Inner solution for the reaction-diffusion model

Since the turnover process is slow with respect to the scale of time t, it suffices to rewrite the reaction-diffusion system (3.1) in terms of t and ε in order to obtain its inner problem:

$$
\begin{aligned}
&\frac{\partial}{\partial t}u(x,t) = D\,\frac{\partial^2}{\partial x^2}u(x,t) - \varepsilon\gamma_b u(x,t) + \varepsilon\gamma_u v(x,t)\,, && x\in(0,l)\,, \quad t>0\,,\\
&\frac{\partial}{\partial t}v(x,t) = \varepsilon\gamma_b u(x,t) - \varepsilon\gamma_u v(x,t)\,, && x\in(0,l)\,, \quad t>0\,,\\
&\frac{\partial u}{\partial x} = \frac{\partial v}{\partial x} = 0 && x=0,l\,, \quad t>0\,,\\
&u(x,0) = f(x)\,, \quad v(x,0) = g(x)\,, && x\in(0,l)\,,
\end{aligned}
\tag{5.36}
$$

where the initial conditions $f(x)$ and $g(x)$ are given by by (3.2) and (3.3), respectively.

By considering the series expansion in ε up to order $N>2$ of the solution (u_{in}, v_{in}) of the inner problem (5.36)

$$
u_{in}(x,t) = \sum_{n=0}^{N}\varepsilon^n u_n(x,t)\,, \qquad v_{in}(x,t) = \sum_{n=0}^{N}\varepsilon^n v_n(x,t)\,,
\tag{5.37}
$$

the following leading-order problem of system (5.36) is obtained

$$
\begin{aligned}
&\frac{\partial}{\partial t}u_0(x,t) = D\,\frac{\partial^2}{\partial x^2}u_0(x,t)\,, && x\in(0,l)\,,\quad t>0\,,\\
&\frac{\partial}{\partial t}v_0(x,t) = 0\,, && x\in(0,l)\,,\quad t>0\,,\\
&\frac{\partial u_0}{\partial x} = \frac{\partial v_0}{\partial x} = 0 && x=0,l\,,\quad t>0\,,\\
&u_0(x,0) = f(x)\,,\quad v_0(x,0) = g(x)\,, && x\in(0,l)\,.
\end{aligned}
\tag{5.38}
$$

Thus, to leading-order, the inner solution of the reaction-diffusion system (3.1) is given by

(5.39)

$$
u_{in}(x,t) \sim u_0(x,t) = \frac{1}{1+k}\frac{(l-2h)}{l} + \frac{2}{1+k}\sum_{n=1}^{\infty}\exp\left(-\frac{n^2\pi^2 D}{l^2}t\right) S_n\cos\left(\frac{n\pi x}{l}\right)\,,
$$

$$
v_{in}(x,t) \sim v_0(x,t) = g(x)\,,
$$

where S_n is as in equation (3.5), and $g(x)$ as in (3.3). As expected, the leading-order inner solution (5.39) satisfies the initial condition for the reaction-diffusion equation (3.1), but does not satisfy its asymptotic dynamics as $t\to\infty$. By integrating the inner solution (5.39) over the photobleached region, we obtain the inner recovery curve

$$
F_{in}(t) \sim \frac{1}{1+k}\left[1 - \frac{l^2}{h(l-2h)}\sum_{n=1}^{\infty}\exp\left(-\frac{n^2\pi^2}{l^2}D\,t\right) S_n^2\right]\,. \tag{5.40}
$$

Comparing with equation (5.8), the recovery of the diffusion equation, we see that when the turnover process is slow; only the fraction $\frac{1}{1+k}$ of the population is contributing to the initial fluorescence recovery (figure 5.3A).

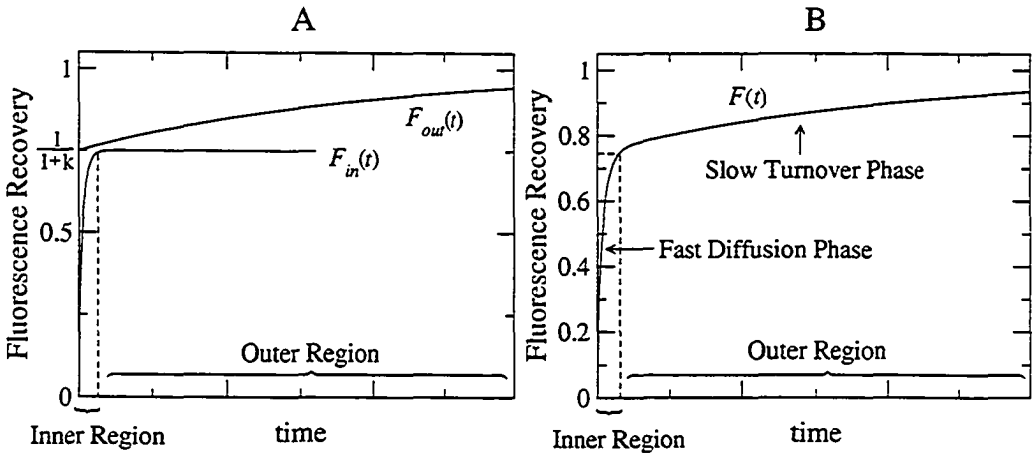

Figure 5.3: A: $F_{in}(t)$ denotes the inner recovery curve (5.40)(or (5.46)) obtained when solving the inner problem (5.36) (or (5.41)) in the boundary layer (inner region) in time; and $F_{out}(t)$ denotes the outer recovery curve (5.55) obtained when solving the outer problem (5.49) in the outer region in time. B: $F(t)$ denotes the approximated recovery curve (5.68) (or (5.73)) when the turnover process is slow compared to the diffusion process. $F(t)$ is obtained from matching the inner and outer recovery curves shown in A.

Inner solution for the compartmental model

In a similar manner, we rewrite the compartmental model (4.1) in terms of t and ε to obtain the following inner problem:

$$
\begin{aligned}
\dot{u}_0 &= -2D_1u_0 + D_2u_1 + D_2u_2 - \varepsilon\gamma_b u_0 + \varepsilon\gamma_u v_0 \,, \\
\dot{u}_1 &= D_1u_0 - D_2u_1 - \varepsilon\gamma_b u_1 + \varepsilon\gamma_u v_1 \,, \\
\dot{u}_2 &= D_1u_0 - D_2u_2 - \varepsilon\gamma_b u_2 + \varepsilon\gamma_u v_2 \,, \\
\dot{v}_0 &= \varepsilon\gamma_b u_0 - \varepsilon\gamma_u v_0 \,, \\
\dot{v}_1 &= \varepsilon\gamma_b u_1 - \varepsilon\gamma_u v_1 \,, \\
\dot{v}_2 &= \varepsilon\gamma_b u_2 - \varepsilon\gamma_u v_2 \,,
\end{aligned}
\tag{5.41}
$$

subject to the initial condition

$$(u_0, u_1, u_2, v_0, v_1, v_2)_{(0)} = \left(0, \frac{1}{1+k}\frac{r}{2}, \frac{1}{1+k}\frac{r}{2}, 0, \frac{k}{1+k}\frac{r}{2}, \frac{k}{1+k}\frac{r}{2}\right) . \tag{5.42}$$

By considering the series expansion in ε up to order $N > 2$ of the solution $(u_0^{in}, u_1^{in} u_2^{in}, v_0^{in}, v_1^{in}, v_2^{in})$ of the inner problem (5.41)-(5.42)

(5.43)

$$u_0^{in}(t) = \sum_{n=0}^{N} \varepsilon^n u_{0n}(t) , \qquad u_1^{in}(t) = \sum_{n=0}^{N} \varepsilon^n u_{1n}(t) , \qquad u_2^{in}(t) = \sum_{n=0}^{N} \varepsilon^n u_{2n}(t) ,$$

$$v_0^{in}(t) = \sum_{n=0}^{N} \varepsilon^n v_{0n}(t) , \qquad v_1^{in}(t) = \sum_{n=0}^{N} \varepsilon^n v_{1n}(t) , \qquad v_2^{in}(t) = \sum_{n=0}^{N} \varepsilon^n v_{2n}(t) ,$$

the following leading-order problem of the initial value problem (5.41)-(5.42) is obtained:

$$\begin{aligned}
\dot{u}_{00} &= -2D_1 u_{00} + D_2 u_{10} + D_2 u_{20} , \\
\dot{u}_{10} &= D_1 u_{00} - D_2 u_{10} , \\
\dot{u}_{20} &= D_1 u_{00} - D_2 u_{20} , \\
\dot{v}_{00} &= 0 , \\
\dot{v}_{10} &= 0 , \\
\dot{v}_{20} &= 0 ,
\end{aligned} \tag{5.44}$$

subject to the initial condition (5.42). Thus, the leading-order approximation for the inner solution (u_0^{in}, v_0^{in}) of the population in the photobleached region C_0, when $k_b = \varepsilon\gamma_b$, $k_u = \varepsilon\gamma_u$, and $\varepsilon \ll 1$, is given by

$$\begin{aligned}
u_0^{in}(t) &\sim \frac{1}{1+k} r(1-r)\left[1 - \exp\left(-\frac{2D_t}{2-r}t\right)\right] , \\
v_0^{in}(t) &\sim 0 ,
\end{aligned} \tag{5.45}$$

which in turns provides the following approximation of the inner recovery curve for the compartmental model (4.1):

$$F_{in}(t) \sim \frac{1}{1+k}\left[1 - \exp\left(-\frac{2D_t}{2-r}t\right)\right] . \tag{5.46}$$

Notice that as with the inner recovery curve (5.40) for the reaction-diffusion model, only the fraction $\frac{1}{1+k}$ of the population is contributing to the initial fluorescence recovery (figure 5.3A).

Outer solution for the reaction-diffusion model

In order to capture the behaviour of the slow turnover process, we introduce the following slow variable (or outer variable in time),

$$\tau = \varepsilon t\,, \tag{5.47}$$

that 'shrinks' the inner layer in time where diffusion governs the dynamics of the fluorescence recovery. By letting

$$U(x,\tau) = u(x,t) = u(x,\tau/\varepsilon)\,, \quad \text{and} \quad V(x,\tau) = v(x,t) = v(x,\tau/\varepsilon)\,, \tag{5.48}$$

the system (3.1) can be rewritten as the following outer problem:

$$\begin{aligned}
&\varepsilon\frac{\partial}{\partial\tau}U(x,\tau) = D\frac{\partial^2}{\partial x^2}U(x,\tau) - \varepsilon\gamma_b U(x,\tau) + \varepsilon\gamma_u V(x,\tau)\,, && x\in(0,l)\,,\ \tau>0\,,\\
&\varepsilon\frac{\partial}{\partial\tau}V(x,\tau) = \varepsilon\gamma_b U(x,\tau) - \varepsilon\gamma_u V(x,\tau)\,, && x\in(0,l)\,,\ \tau>0\,,\\
&\frac{\partial U}{\partial x} = \frac{\partial V}{\partial x} = 0 && x=0,l\,,\ \tau>0\,,\\
&U(x,0) = f(x)\,,\quad V(x,0) = g(x)\,, && x\in(0,l)\,.
\end{aligned} \tag{5.49}$$

Considering the series expansion in ε up to order $N>2$ of the solution (U_{out}, V_{out}) of the outer problem (5.49)

$$U_{out}(x,\tau) = \sum_{n=0}^{N}\varepsilon^n U_n(x,\tau)\,, \qquad V_{out}(x,t) = \sum_{n=0}^{N}\varepsilon^n V_n(x,\tau)\,, \tag{5.50}$$

the leading-order problem of equation (5.49) is given by

$$\begin{aligned}
&0 = D\frac{\partial^2}{\partial x^2}U_0(x,\tau)\,, && x\in(0,l)\,,\ \tau>0\,,\\
&\frac{\partial}{\partial\tau}V_0(x,\tau) = \gamma_b U_0(x,\tau) - \gamma_u V_0(x,\tau)\,, && x\in(0,l)\,,\ \tau>0\,,\\
&\frac{\partial U_0}{\partial x} = \frac{\partial V_0}{\partial x} = 0 && x=0,l\,,\ \tau>0\,,\\
&U_0(x,0) = f(x)\,,\quad V_0(x,0) = g(x)\,, && x\in(0,l)\,.
\end{aligned} \tag{5.51}$$

Due to the no-flux boundary condition, the solution for U_0 is given by

$$U_0(x,\tau) = C\,, \tag{5.52}$$

where C is a constant to be determined. As expected for the outer solution, U_0 will not satisfy the initial condition $f(x)$, and the second equation in system (5.51) becomes

$$\frac{\partial}{\partial\tau}V_0(x,\tau) = \gamma_b C - \gamma_u V_0(x,\tau)\,. \tag{5.53}$$

Note that the solution V_0 does not depend explicitly on the spatial variable. However, the constant C (and therefore V_0) will depend on whether the initial condition $g(x)$ for V_0 is considered in the bleached region or in the unbleached region. Since our interest focuses on the behaviour of the recovery curve in the bleached region, we will consider the solution for V_0 in the bleached region as well. More specifically, equation (5.53) is subject to the initial condition $V_0(x,0) = 0$. Thus, the solution of the outer problem (5.49) in the bleached region is given, up to leading order, by

$$\begin{aligned} U_{out}(x,\tau) &\sim U_0(x,\tau) = C \\ V_{out}(x,\tau) &\sim V_0(x,\tau) = k\,C\,(1-e^{-\gamma_u\tau})\,, \end{aligned} \tag{5.54}$$

where $k = \gamma_b/\gamma_u$, and the recovery in the outer region is approximated by the following outer recovery curve (figure 5.3A):

$$F_{out}(t) \sim C^* + k\,C^*\left(1-e^{-k_u t}\right)\,, \tag{5.55}$$

where $C^* = \dfrac{l}{l-2h}\,C$. We shall see shortly that $C^* = \dfrac{1}{1+k}$.

Outer solution for the compartmental model

Considering the slow variable τ given by (5.47), and letting

$$\begin{aligned} &w_0(\tau) = u_0(\tau/\varepsilon)\,, \quad w_1(\tau) = u_1(\tau/\varepsilon)\,, \quad w_2(\tau) = u_2(\tau/\varepsilon)\,, \\ &z_0(\tau) = v_0(\tau/\varepsilon)\,, \quad z_1(\tau) = v_1(\tau/\varepsilon)\,, \quad z_2(\tau) = v_2(\tau/\varepsilon)\,, \end{aligned} \tag{5.56}$$

the compartmental model (4.1) is rewritten as the following outer problem:

$$
\begin{aligned}
\varepsilon \dot{w}_0 &= -2D_1 w_0 + D_2 w_1 + D_2 u_2 - \varepsilon \gamma_b w_0 + \varepsilon \gamma_w z_0 \,, \\
\varepsilon \dot{w}_1 &= D_1 w_0 - D_2 w_1 - \varepsilon \gamma_b w_1 + \varepsilon \gamma_w z_1 \,, \\
\varepsilon \dot{w}_2 &= D_1 w_0 - D_2 w_2 - \varepsilon \gamma_b w_2 + \varepsilon \gamma_w z_2 \,, \\
\varepsilon \dot{z}_0 &= \varepsilon \gamma_b w_0 - \varepsilon \gamma_w z_0 \,, \\
\varepsilon \dot{z}_1 &= \varepsilon \gamma_b w_1 - \varepsilon \gamma_w z_1 \,, \\
\varepsilon \dot{z}_2 &= \varepsilon \gamma_b w_2 - \varepsilon \gamma_w z_2 \,,
\end{aligned}
\tag{5.57}
$$

where the dot denotes the derivative with respect to τ.

Considering the series expansion in ε up to order $N > 2$ of the solution $(w_0^{out}, w_1^{out} w_2^{out}, z_0^{out}, z_1^{out}, z_2^{out})$ of the outer problem (5.57)

(5.58)

$$
\begin{aligned}
w_0^{out}(t) &= \sum_{n=0}^{N} \varepsilon^n w_{0n}(t) \,, \qquad w_1^{out}(t) = \sum_{n=0}^{N} \varepsilon^n w_{1n}(t) \,, \qquad w_2^{out}(t) = \sum_{n=0}^{N} \varepsilon^n w_{2n}(t) \,, \\
z_0^{out}(t) &= \sum_{n=0}^{N} \varepsilon^n z_{0n}(t) \,, \qquad z_1^{out}(t) = \sum_{n=0}^{N} \varepsilon^n z_{1n}(t) \,, \qquad z_2^{out}(t) = \sum_{n=0}^{N} \varepsilon^n v_{2n}(t) \,,
\end{aligned}
$$

we obtain the following leading-order problem of system (5.57):

$$
\begin{aligned}
0 &= -2D_1 w_{00} + D_2 w_{10} + D_2 w_{20} \,, \\
0 &= D_1 w_{00} - D_2 w_{10} \,, \\
0 &= D_1 w_{00} - D_2 w_{20} \,, \\
\dot{z}_{00} &= \gamma_b w_{00} - \gamma_u z_{00} \,, \\
\dot{z}_{10} &= \gamma_b w_{10} - \gamma_u z_{10} \,, \\
\dot{z}_{20} &= \gamma_b w_{20} - \gamma_u z_{20} \,,
\end{aligned}
\tag{5.59}
$$

Writing D_1 and D_2 in terms of D_t (see equation (4.9)), we solve the first three equations in (5.59) and obtain that

$$
(w_{00}, w_{10}, w_{20}) = \left(B, \frac{r}{1-r} B, \frac{r}{1-r} B \right) \,, \tag{5.60}
$$

where r is as in equation (4.10) and B is a constant to be determined. Thus, the fourth equation, determining the dynamics of the bound population in the bleached region C_0, becomes

$$\dot{z}_{00} = \gamma_b B - \gamma_u z_{00} \,. \tag{5.61}$$

By solving equation (5.61) subject to the initial condition $\dot{z}_{00}(0) = 0$, we obtain the following leading-order approximation for the solution (w_0^{out}, z_0^{out}) of the outer problem (5.57), that represents the population in the photobleached region C_0:

$$\begin{aligned} w_0^{out}(\tau) &\sim w_{00}(\tau) = B \\ z_0^{out}(\tau) &\sim z_{00}(\tau) = k\,B\,(1 - e^{-\gamma_u \tau}) \,. \end{aligned} \tag{5.62}$$

Thus, the recovery in the outer region is approximated by the following outer recovery curve (figure 5.3A):

$$F_{out}(t) \sim B^* + k\,B^* \left(1 - e^{-k_u t}\right) \,, \tag{5.63}$$

where $B^* = \dfrac{B}{r(1-r)}$. We will show shortly that $B^* = \dfrac{1}{1+k}$. Assuming this, notice that (5.63) coincides with (5.55)

Asymptotic match and final approximation for the reaction-diffusion model

In order to find the values of C and C^* in equations (5.54) and (5.55), we match the inner and outer solutions in the overlapping region between the inner and outer regions. Note that the intermediate limits of the solutions in the bleached region of the outer problem (5.49) are given by

$$\begin{aligned} &\lim_{\varepsilon \to 0} U_{out}(x, \varepsilon t) = C \,, \\ &\lim_{\varepsilon \to 0} V_{out}(x, \varepsilon t) = \lim_{\varepsilon \to 0} k\,C \left(1 - e^{-\gamma_u \varepsilon t}\right) = 0 \,, \end{aligned} \tag{5.64}$$

and the intermediate limits of the solutions in the bleached region of the inner problem (5.36) are given by

$$
\begin{aligned}
\lim_{\varepsilon\to 0} u_{in}(x,\tau/\varepsilon) &= \lim_{\varepsilon\to 0}\left\{\frac{1}{1+k}\frac{(l-2h)}{l}+\frac{2}{1+k}\times\right. \\
&\qquad \left.\sum_{n=1}^{\infty}\exp\left(-\frac{n^2\pi^2 D\tau}{l^2\varepsilon}\right) S_n\, Cos\left(\frac{n\pi x}{l}\right)\right\} \\
&= \frac{1}{1+k}\frac{(l-2h)}{l}\,, \\
\lim_{\varepsilon\to 0} v_{in}(x,\tau/\varepsilon) &= \lim_{\substack{\varepsilon\to 0\\ |x-c|\le h}} g(x) = 0\,.
\end{aligned}
\tag{5.65}
$$

In order for the inner and outer solutions to match asymptotically, the intermediate limits given by equations (5.64)-(5.65) have to coincide [2]. Therefore,

$$
C=\frac{1}{1+k}\frac{(l-2h)}{l}\,, \qquad C^*=\frac{1}{1+k}\,,
\tag{5.66}
$$

and the leading-order approximation for the solution of the system (3.1) in the photobleached region when $k_b=\varepsilon\gamma_b$, $k_u=\varepsilon\gamma_u$, and $\varepsilon \ll 1$ is given by

$$
\begin{aligned}
u(x,t) &\sim u_{in}(x,t)+U_{out}(x,\varepsilon\, t)-\lim_{\varepsilon\to 0} U_{out}(x,\varepsilon\, t)\,, \\
v(x,t) &\sim v_{in}(x,t)+V_{out}(x,\varepsilon\, t)-\lim_{\varepsilon\to 0} V_{out}(x,\varepsilon\, t)\,.
\end{aligned}
\tag{5.67}
$$

By integrating the leading-order approximation for the total population $u(x,t)+v(x,t)$ obtained in equation (5.67) over the bleached region, and normalizing the result, we have that the recovery curve corresponding to the reaction-diffusion equation (3.1) can be approximated by

$$
F(t)\sim \underbrace{\frac{1}{1+k}\left[1-\frac{l^2}{h(l-2h)}\sum_{n=1}^{\infty} e^{-\left(\frac{n\pi}{l}\right)^2 Dt} S_n^2\right]}_{\text{Diffusion Phase}} + \underbrace{\frac{k}{1+k}\left(1-e^{-k_u t}\right)}_{\text{Turnover Phase}}\,,
\tag{5.68}
$$

when the turnover process is slow. This recovery curve exhibits a biphasic behaviour, which is illustrated in figure 5.3B. The first term of expression (5.68), which corresponds to the inner solution of equation (3.1), is responsible for the fast recovery phase in the inner region produced by the proportion $\frac{1}{1+k}$ of the population that

is diffusing rapidly, and the second term, which corresponds to the outer solution of equation (3.1), describes the slow recovery phase in the outer region produced by the turnover of the population that is bound.

Asymptotic match and final approximation for the compartmental model

Similarly, we match the inner solution (5.45) and the outer solution (5.62) in the overlapping region between the inner and outer regions. The intermediate limits of the solutions in the bleached region C_0 of the outer problem (5.57) are given by

$$\begin{aligned} &\lim_{\varepsilon\to 0} w_0^{out}(\varepsilon t) = B\,, \\ &\lim_{\varepsilon\to 0} z_0^{out}(\varepsilon t) = \lim_{\varepsilon\to 0} kB\left(1-e^{-\gamma_u \varepsilon t}\right) = 0\,, \end{aligned} \tag{5.69}$$

and the intermediate limits of the solutions in the bleached region of the inner problem (5.41) are given by

$$\begin{aligned} \lim_{\varepsilon\to 0} u_0^{in}(\tau/\varepsilon) &= \lim_{\varepsilon\to 0} \frac{1}{1+k} r(1-r)\left[1-\exp\left(-\frac{2D_t}{2-r}\frac{\tau}{\varepsilon}\right)\right] \\ &= \frac{1}{1+k} r(1-r)\,, \\ \lim_{\varepsilon\to 0} v_0^{in}(\tau/\varepsilon) &= 0\,. \end{aligned} \tag{5.70}$$

Equating the intermediate limits given by equations (5.69)-(5.70), we obtain

$$B = \frac{1}{1+k} r(1-r)\,, \qquad B^* = \frac{1}{1+k}\,, \tag{5.71}$$

and the leading-order approximation for the solution of the compartmental model (4.1) in the photobleached region C_0 when $k_b = \varepsilon\gamma_b$, $k_u = \varepsilon\gamma_u$, and $\varepsilon \ll 1$, is given by

$$\begin{aligned} u_0(t) &\sim u_0^{in}(t) + w_0^{out}(\varepsilon\, t) - \lim_{\varepsilon\to 0} w_0^{out}(\varepsilon\, t)\,, \\ v_0(t) &\sim v_0^{in}(t) + z_0^{out}(\varepsilon\, t) - \lim_{\varepsilon\to 0} z_0^{out}(\varepsilon\, t)\,. \end{aligned} \tag{5.72}$$

Adding the two equations in (5.72) provides an approximation for the dynamics of the fluorescent population of biomolecules $u_0(t) + v_0(t)$ in the photobleached region

C_0, which is then normalized to obtain the following approximation for the recovery curve corresponding to the compartmental model (4.1):

$$F(t) \sim \underbrace{\frac{1}{1+k}\left(1-e^{-2D_t t/(2-r)}\right)}_{\text{Diffusion Phase}} + \underbrace{\frac{k}{1+k}\left(1-e^{-k_u t}\right)}_{\text{Turnover Phase}}. \tag{5.73}$$

The biphasic behavior of the fluorescence recovery curve (5.73) can be illustrated in a figure similar to figure 5.3B. Note that the second term in equation (5.73) is identical to the second term in equation (5.68), which provides evidence for the strong relationship between the turnover phase of the compartmental model (4.1) and that of the reaction-diffusion system (3.1). In the next section, we will show how the diffusion phases of the two models can also be related by expressing the diffusional transfer coefficient D_t in terms of the diffusion coefficient D.

5.4 Relationship Between the Compartmental Model and the Reaction-Diffusion Model

From the previous section, it is evident that when the diffusion and the turnover processes take place on significantly different time scales (e.g., a fast diffusion phase and a slow turnover phase), both the reaction-diffusion system (3.1) and the compartmental model (4.1) produce exactly the same quantitative effect on the turnover phase of the recovery. This is because in both models the binding-unbinding process is described in terms of the same parameters, namely, a binding rate k_b and an unbinding rate k_u. But this is not the case for the diffusion process, which is described in terms of different parameters, namely, a diffusion coefficient D for the reaction-diffusion model (3.1), and a diffusional transfer coefficient D_t for the compartmental model (4.1). Thus, the natural question of how the diffusional transfer coefficient D_t relates to the diffusion coefficient D arises. In other words, how is equation (2.3) related to equation (5.15). To answer this question, we apply the concepts of *residence time*, *transit time* [31, 32], and *mean time to capture* [3].

Consider a cell nucleus whose shape is approximated with a rectangle of length

l, and whose photobleaching profile is given by a narrow band of width $2h$, centered on the x axis at c (see figure 2.2). According to the diffusional compartmental model (5.15), the average residence times in the bleached region and in each of the unbleached regions are given, respectively, by

$$\tau_{r1} = \frac{1}{2D_1}, \quad \text{and} \quad \tau_{r2} = \frac{1}{D_2}. \tag{5.74}$$

Moreover, since the relation

$$r = \frac{F_a}{F_0} = \frac{l-2h}{l} \tag{5.75}$$

must be satisfied, the expressions for the fractional diffusional transfer coefficients, D_1 and D_2, in terms of the diffusional transfer coefficient, D_t, given in equation (4.9), can be rewritten as

$$D_1 = \frac{l-2h}{l+2h} D_t, \qquad D_2 = 2\frac{2h}{l+2h} D_t, \tag{5.76}$$

which in turn implies that $\frac{D_1}{D_2} = \frac{l-2h}{2(2h)}$, i.e.,

$$\frac{\tau_{r2}}{\tau_{r1}} = \frac{2D_1}{D_2} = \frac{l-2h}{2h}. \tag{5.77}$$

This ratio between the average residence times was found based on the diffusional compartmental model (5.15). We aim to find the same ratio from the diffusion equation (2.3). If we portray the bleached region as a line segment of length $2h$ with open boundaries located at $x = 0$ and $x = 2h$, and let $\tau_{r1}(x)$ denote the mean residency time of a fluorescent particle located at x in the bleached region, then

$$\tau_{r1}(x) = w_a(x) + w_d(x), \tag{5.78}$$

where $w_a(x)$ is the mean time of arrival at x, i.e., the mean time that a particle takes to move from one of the open boundaries to the location x in the bleached region, and $w_d(x)$ is the mean time of departure of a particle located at x, i.e., the mean time that it takes to leave the photobleached region. (see figure 5.4A).

First, consider a particle located at x in the photobleached region, and assume, without loss of generality, that it has come from the left boundary $x = 0$. The mean

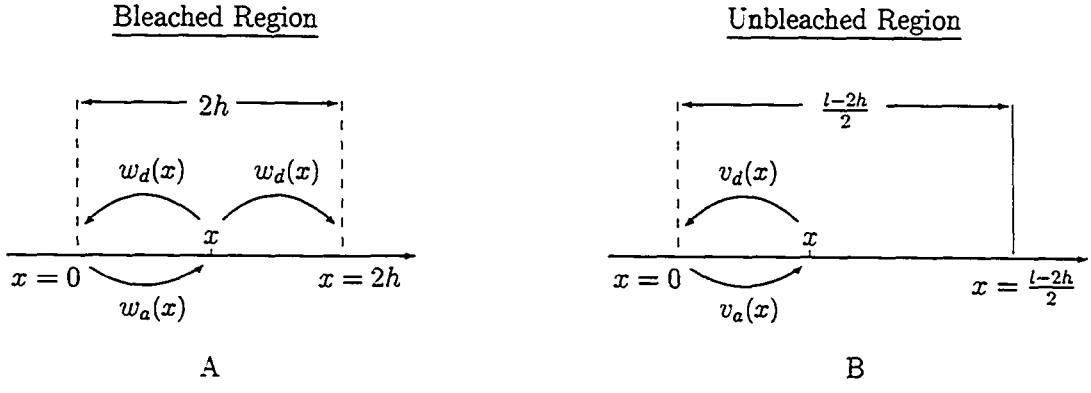

Figure 5.4: A: The mean residency time $\tau_{r1}(x)$ of a particle located at x in the bleached region is given by $\tau_{r1}(x) = w_a(x) + w_d(x)$, where $w_a(x)$ is the mean time of arrival at x, and $w_d(x)$ is the mean time of departure. B: The mean residency time $\tau_{r2}(x)$ of a particle located at x in the unbleached region is given by $\tau_{r2}(x) = v_a(x) + v_d(x)$, where $v_a(x)$ is the mean time of arrival at x, and $v_d(x)$ is the mean time of departure.

arrival time is given by the *transit time* [31, 32], which is the time that it takes a diffusing particle to move a certain length, i.e.,

$$w_a(x) = \frac{x^2}{2D} . \tag{5.79}$$

The particle located at x may leave the photobleached region at either the right or the left boundary (see figure 5.4A). Because of the assymetry, we cannot use the simple concept of transit time to find the mean time of departure. Instead, we use the concept of *mean time to capture* [3]. More specifically, if we consider the random walk of the particle located at x at time $t = 0$, and allow it to move to the right or left a distance δ every τ units of time, then at time $t = \tau$, the particle will be at $x + \delta$ with probability 1/2, or at at $x - \delta$ with probability 1/2. The mean times of departure from these new positions are $w_d(x + \delta)$ and $w_d(x - \delta)$, respectively, and thus the expected value for $w_d(x)$ is

$$w_d(x) = \tau + \frac{1}{2}\left[w_d(x + \delta) + w_d(x - \delta)\right] .$$

If we subtract $w_d(x)$ from both sides, multiply by $2/\delta$, and let $\delta \to 0$, we obtain

$$\frac{dw_d}{dx}(x) - \frac{dw_d}{dx}(x-\delta) + \frac{2\tau}{\delta} = 0 .$$

Dividing by δ and noticing that $\frac{2\tau}{\delta^2} = \frac{1}{D}$, we obtain the Poisson equation

$$\frac{d^2 w_d}{dx^2} + \frac{1}{D} = 0 . \tag{5.80}$$

In the bleached region, fluorescent particles could leave from either side, and hence appropriate boundary boundary conditions are $w_d(0) = w_d(2h) = 0$. Therefore, the solution of (5.80) is given by

$$w_d(x) = \frac{1}{2D}\left(2hx - x^2\right) . \tag{5.81}$$

Thus, combining (5.79) and (5.81), we find that $\tau_{r1}(x) = w_a(x) + w_d(x) = \frac{hx}{D}$, and then the mean residency time in the bleached region is given by

$$\tau_{r1} = \frac{\int_0^{2h} \tau_{r1}(x)\, dx}{2h} = \frac{h^2}{D} . \tag{5.82}$$

A similar procedure is followed to find the mean residency time τ_{r2} in either of the unbleached regions. Due to the symmetry of the right and left unbleached regions, it suffices to consider the right one, that can be portrayed as a line segment of length $\frac{l-2h}{2}$ with an open boundary at $x = 0$ and a closed boundary at $x = \frac{l-2h}{2}$ (see figure 5.4B). In this case, if $\tau_{r2}(x)$ denotes the mean residency time of a fluorescent particle located at x in the unbleached region, then

$$\tau_{r2}(x) = v_a(x) + v_d(x) , \tag{5.83}$$

where $v_a(x)$ represents the mean time of arrival at x, and $v_d(x)$ represents the mean time of departure from x (see figure 5.4B). The Poisson equation, (5.80), also applies to $v_d(x)$, but in this case is subject to a reflecting boundary condition, i.e., $v_d(0) = 0$ and $\frac{dv_d}{dx}(\frac{l-2h}{2}) = 0$. Therefore,

$$v_a(x) = \frac{x^2}{2D} , \quad v_d(x) = \frac{1}{2D}\left[(l-2h)x - x^2\right] ,$$

and the mean residency time in the right or left unbleached region is given by

$$\tau_{r2} = 2\,\frac{\int_0^{(l-2h)/2} \tau_{r2}(x)\,dx}{l-2h} = \frac{(l-2h)^2}{8D}\,. \tag{5.84}$$

Using (5.82) and (5.84), the ratio between the average residency times, based on the diffusion equation (2.3), is given by

$$\frac{\tau_{r2}}{\tau_{r1}} = \frac{(l-2h)^2}{2(2h)^2}\,. \tag{5.85}$$

Comparing (5.85) with the ratio obtained for the compartmental model, (5.77), we notice a difference due to the distinct approaches in modelling. In particular, the diffusion equation considers space explicitly and involves a unique parameter D, whereas the diffusional compartmental model does not consider space explicitly and involves two parameters D_1 and D_2. However, this difference can be 'reconciled' in order to find an empirical relationship between the diffusional transfer coefficient D_t and the diffusion coefficient D.

Equating the residency times (5.74) obtained from the diffusional compartmental model with the residency times (5.82) and (5.84) obtained from the diffusion equation, we obtain

$$\frac{1}{2D_1} = \frac{h^2}{D}\,, \quad \text{and} \quad \frac{1}{D_2} = \frac{(l-2h)^2}{8D}\,. \tag{5.86}$$

Moreover, when the expressions for the fractional diffusional transfer coefficients, D_1 and D_2, given by equation (5.76), are substituted in equation (5.86), we obtain two relations between the diffusion coefficient D and the diffusional transfer coefficient D_t,

$$(D_t)_1 = \frac{2(l+2h)}{(2h)^2(l-2h)}D\,, \qquad (D_t)_2 = \frac{2(l+2h)}{h(l-2h)^2}D\,, \tag{5.87}$$

where $(D_t)_1$ and $(D_t)_2$ are the diffusional transfer coefficients obtained from substituting the first and second expressions of equation (5.76) in equation (5.86), respectively.

Thus, the natural question that arises is which of the relations in equation (5.87) should be considered. Note first that when the region photobleached is precisely the

middle third of the cell nucleus, i.e., $\frac{2h}{l} = \frac{1}{3}$, the two ratios between the residency times given by Eqs. (5.77) and (5.85) are equivalent, as well as both relations in equation (5.87), which would provide the desired relationship between the diffusional transfer coefficient D_t and the diffusion coefficient D. However, the photobleached region does not necessarily correspond to one third of the nucleus size. So, to give an empirical solution to this problem, we take the average between $(D_t)_1$ and $(D_t)_2$, and call it the diffusional transfer coefficient D_t,

$$D_t = \frac{(D_t)_1 + (D_t)_2}{2} = \left[\frac{(l+2h)}{(2h)^2(l-2h)} + \frac{(l+2h)}{h(l-2h)^2}\right] D\,. \tag{5.88}$$

This last expression provides a fairly accurate empirical relation between the diffusional tranfer coefficient D_t and the diffusion coefficient D when the size of the photobleached region is close to one third of the cell nucleus. To illustrate the efficacy of relation (5.88), we plot in figure 5.5A a set of simulated recovery data obtained from adding noise to the recovery curve coming from a diffusion process characterized with a fixed diffusion coefficient $D = 0.5\,\mu\text{m}^2/\text{s}$, and then plot the theoretical recovery curve (5.17) coming from the diffusional compartmental model (5.15), with a diffusional transfer coefficient $D_t = 0.62\,\text{s}^{-1}$ obtained from relation (5.88). To verify that this value for D_t gives a good estimation, we also fit, in figure 5.5B, the simulated data with the recovery curve (5.17) coming from the diffusional compartmental model (5.15) using the method of least squares. This procedure gives an estimate of $D_t = 0.61\,\text{s}^{-1}$ for the diffusional transfer coefficient. Moreover, one could use this estimated value to recover the diffusion coefficient D, just by substituting it in the relation (5.88). On doing so, one obtains $D = 0.494\,\mu\text{m}^2/\text{s}$, a very accurate estimate for the diffusion coefficient, which illustrates the effectiveness of relation (5.88).

The important point to notice is that this last estimated value for the diffusion coefficient D was obtained just by fitting a simple exponential curve (equation (5.17)) to the data, and using the relation (5.88). Therefore, this relation also provides a simplified method for estimating the diffusion coefficient D.

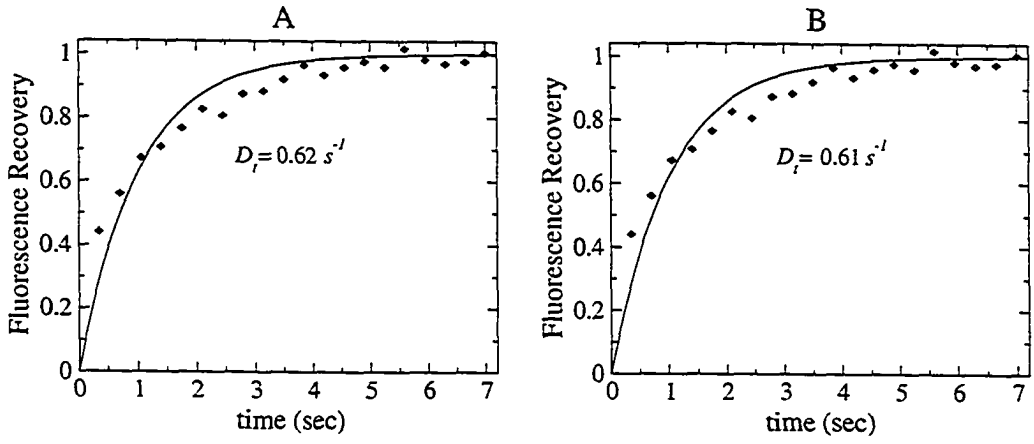

Figure 5.5: In both figures, the small diamonds represent the simulated recovery data obtained from adding noise to the recovery curve (5.8) with a fixed diffusion coefficient $D = 0.5\,\mu\text{m}^2/\text{s}$. In (A) the data is fitted by just plotting the theoretical recovery curve (5.17) coming from the diffusinal compartmental model (5.15), with a diffusional transfer coefficient $D_t = 0.62\,\text{s}^{-1}$ obtained from relation (5.88), and in (B) the data is fitted with equation (5.17) using the method of least squares, from which a diffusional transfer coefficient $D_t = 0.61\,\text{s}^{-1}$ is obtained.

5.5 Application to Nuclear Protein Dynamics

In this section, we will employ the results from the perturbation analysis obtained in the previous sections. We show how the results can be used to interpret different FRAP data sets and estimate model parameters for nuclear proteins whose dynamics are described with the reaction-diffusion model (3.1) or the compartmental model (4.1). In particular, we use data obtained from nuclear actin and histone H1.

5.5.1 Nuclear Actin

To illustrate a particular application of the results in the context of nuclear actin, we revisit the FRAP data on nuclear actin that were presented earlier in sections 2.3.2 and 3.3.2. The data are presented again in figure 5.6 (diamonds). As mentioned previously, the FRAP curve comprises a fast recovery phase and a slow recovery phase. This behaviour can be explained by assuming that nuclear actin is present in both globular and filamentous forms. In the previous chapters, we used the explicit

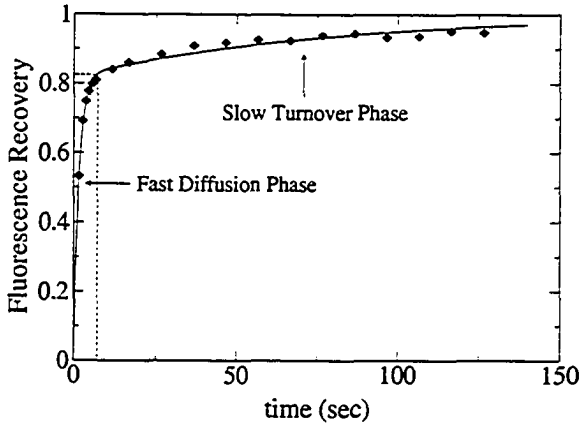

Figure 5.6: Nuclear GFP-actin FRAP data (diamonds), which exhibit a biphasic behaviour, are fitted with equation (5.73) (solid curve), obtaining $k_b = 0.0029\, s^{-1}$, $k_u = 0.0131\, s^{-1}$ and $D_t = 0.4331\, s^{-1}$, with a residual mean square $s^2 = 0.000174$.

solutions of the reaction-diffusion model (3.1) and the compartmental model (4.1) to analyze the data (sections 2.3.2 and 3.3.2, respectively).

In this section, we will avoid using the explicit solutions of the models by taking advantage of the qualitative biphasic behaviour of the experimental data, which suggests that the turnover process occurs on a significantly slower time scale than the diffusion process (figure 5.6). Specifically, we use the compartmental model (4.1), and fit the data with recovery curve (5.73). From the fitting, shown in figure 5.6, we obtain the following estimated parameters, representing the binding and unbinding rates, and the diffusional transfer coefficient, respectively,

$$k_b = 0.0029\, s^{-1}, \quad k_u = 0.0131\, s^{-1}, \quad D_t = 0.4331\, s^{-1}. \tag{5.89}$$

From these estimates, we conclude that the proportions of nuclear actin in globular and filamentous form are given by $P_u = \dfrac{k_u}{k_u + k_b} = 0.82$ and $P_b = \dfrac{k_b}{k_u + k_b} = 0.18$, respectively. Note that the estimates are consistent with the ones obtained using the explicit solution of the compartmental model (4.1) (figure 4.2).

Moreover, although the fitting does not provide an estimation of the diffusion coefficient, we can estimate it using the results of section 5.4. Specifically, we use the estimate of the diffusional transfer coefficient D_t and relation (5.88) to obtain an estimate of $D = 0.463\, \mu m^2/s$ for the diffusion coefficient. This estimate is consistent

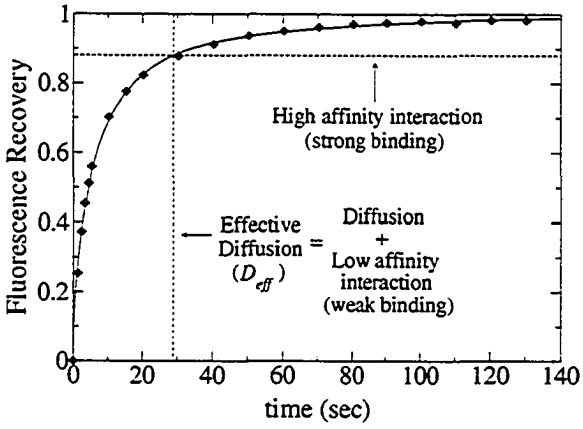

Figure 5.7: The GFP-histone H1 FRAP data (diamonds) are fitted with the recovery curve (3.4) (solid curve). From the fitting, we obtain that approximately 12% of the population is *strongly* bound to the chromatin structure with $k_b = 0.0026\, s^{-1}$ and $k_u = 0.0193\, s^{-1}$ as estimates for the binding and unbinding rates; and that approximately 88% of the population, which diffuses with an *effective* diffusion coefficient $D_{eff} = 0.073\, \mu m^2/s$, is constituted by a *weakly* bound subpopulation and a freely diffusing subpopulation.

with the one obtained using the explicit solution of the reaction-diffusion model (3.1) (figure 3.2).

5.5.2 Histone H1

The second application of the results is in the context of histone H1 dynamics. To illustrate the application, we complement the analysis on the histone H1 FRAP data presented earlier in section 3.3.1. The FRAP data are shown again in figure 5.7. The procedure followed in 3.3.1 was to fit the recovery curve (3.4), obtained by solving the reaction-diffusion equation (3.1), to the experimental FRAP data. From the fitting, it was estimated that approximately 88% of the population is moving freely with a diffusion coefficient of value $0.073\, \mu m^2/s$, and the remaining 12% of the population is bound to the chromatin structure. The estimated diffusion coefficient for the histone H1 appears to be smaller than expected for a diffusing biomolecule of its molecular weight, and the proportion of bound population is much smaller than biologically

expected. This discrepancy can be explained by attributing the 12% to a fraction of the population that is *strongly* bound to the chromatin structure, and interpreting the estimated diffusion coefficient for the other 88% of the population as an *effective* diffusion coefficient that accounts for a *weakly* bound subpopulation and an actual diffusing subpopulation (figure 5.7). That is, the initial 88% of the recovery exhibits a *reduced diffusive behaviour* (see section 5.2), resulting in a recovery curve that appears to be produced by a single population moving randomly with an effective diffusion coefficient

$$D_{eff} = \frac{D}{1+\omega} = 0.073\,\mu\text{m}^2/\text{s}\,, \tag{5.90}$$

where D is the actual diffusion coefficient of the biomolecules, and $\frac{1}{1+\omega}$ is the steady-state proportion of the population exhibiting reduced diffusive behaviour, that is freely diffusing.

Based on the molecular weight of the fusion protein GFP-histone H1 ($\sim$ 49 kDa), the average density of proteins ($\rho = 1.38 \times 10^3\,\text{Kg/m}^3$), the Einstein-Smoluchowski relation

$$D = \frac{KT}{f}\,, \tag{5.91}$$

where K is the Boltzmann's constant, T is the absolute temperature, $KT = 4.1164 \times 10^{-21}$ J at 25°C, f is the frictional drag coefficient for the fusion protein (assuming it has a spherical shape) given by Stokes' law [3, 17, 41]

$$f = 6\,\pi\,\eta\,r\,, \tag{5.92}$$

$\eta \sim 0.0023$ Pa s is the the approximated nuclear viscosity, and r is the radius of the fusion protein, we expect its diffusion coefficient D in the nucleoplasm to be approximately $D = 40\,\mu\text{m}^2/\text{s}$ (see table 5.1).

By substituting this expected diffusion coefficient, which is three orders of magnitude greater than the *effective* diffusion coefficient, we conclude that the steady-state proportion of the histone H1 population freely diffusing is less than 0.2%. This implies that almost all the histone H1 population is bound to the chromatin structure, as expected from its function in the compaction of chromatin. Moreover, this

Property	Value	Comment
Molecular weight	~ 49 kDa	1 kDa $= 100,000$ Da
Mass	$\sim 8134 \times 10^{-26}$ kg	Mass of 1 Da $= 1.66 \times 10^{-24}$ g
Density	$1.38 \times 10^{3}\,\mathrm{kg/m^3}$	Average density of proteins [41]
Volume	$\sim 58.9 \times 10^{-27}\,\mathrm{m^3}$	Mass/density
Radius	$\sim 2.4 \times 10^{-9}\,\mathrm{m}$	Assuming a spherical volume
Drag coefficient	$\sim 10.4 \times 10^{-11}\,\mathrm{Kg/s}$	From Stokes' law (5.92)
Diffusion coefficient	$\sim 40\,\mu\mathrm{m}^2/\mathrm{s}$	From Einstein relation (5.91)

Table 5.1: Physical properties of GFP-histone H1.

interpretation of the *effective* diffusion coefficient is consistent with the current understanding that there is a rapid exchange of histone H1 on the chromatin structure [51]. Although the steady-state proportion of diffusing biomolecules is very small, it is crucial for the functional dynamics of histone. In particular, if H1 histone proteins were permanently associated with chromatin it would be more difficult for chromatin remodelling factors to gain access to chromatin [21]. This small proportion allows histone molecules to move randomly from one binding site to another on the chromatin structure, and, evidently, it is the reason there is a fluorescence recovery after photobleaching. We are now in a better position to understand how mutations in these proteins change their binding events and functional dynamics [37].

5.6 Discussion

By applying perturbation analysis to the reaction-diffusion model (3.1) and the compartmental model (4.1), we have provided a formal explanation of two limiting dynamical types of behaviour exhibited by experimental recovery data, namely a *reduced diffusive behaviour* and a *biphasic behaviour*. We showed how a rapid turnover, or rapid exchange of binding proteins in the immobile structure, leads to a fluorescence recovery curve that looks as though it was produced by a purely

diffusing population, but one that is characterized by a reduced diffusion coefficient, called an *effective* diffusion coefficient. In contrast, slow exchange of proteins leads to a biphasic behaviour distinguished by a fast recovery phase due to the diffusion process and a slow recovery phase due to the turnover process. The analysis allowed for a characterization of the behaviour of the fluorescence recovery curves, which in turn put us in a better position to understand and interpret the data, and simplified the task of parameter estimation.

Also, we showed how the two models (3.1) and (4.1), describing the same type of dynamic using different approaches, relate and share a common ground. Their relation provides a simplified method for estimating the diffusion coefficient D.

We demonstrated that the theoretical characterization of the fluorescence recovery finds its application in the dynamics of nuclear proteins. More specifically, we illustrated the application of the results in the context of nuclear actin dynamics and histone H1 dynamics. For nuclear actin, we interpreted the biphasic behaviour of the experimental fluorescence recovery and simplified the task of parameter estimation by fitting the data with a simple recovery curve (equation (5.73)) that reflects in its expression the fast and slow phases of the experimental fluorescence recovery. We arrived to the same conclusion as in chapters 3 and 4, namely that the FRAP data supports the hypothesis that actin is present in both globular and filamentous forms in the nucleus [61]. For histone H1, we interpreted the reduced diffusive behaviour of its recovery after photobleaching, and concluded that the FRAP data is consistent with the current biological understanding that there is a rapid exchange of histone H1 on the chromatin structure [51], i.e., that there is a high population weakly bound to the chromatin structure.

From these applications, it is evident how the task of parameter estimation can be simplified for two types of recovery data. If the FRAP data exhibits obvious biphasic behaviour, where the turnover phase is slow compared to the diffusion phase, one can fit the data with either theoretical recovery curve (5.68) or (5.73). If the FRAP data does not exhibit biphasic behaviour but instead appears as if produced by a single diffusing population, and one knows *a priori* that the biomolecules under study are

weakly bound to an immobile structure (i.e., the turnover process is very fast relative to the time of recovery), one could fit the data with the recovery curve (5.25), coming from a simple diffusion model, and obtain an *effective* diffusion coefficient D_{eff} that relates to the real diffusion coefficient D and the parameter $k = \frac{k_b}{k_u}$ as in Eq. (5.24). Thus, if one knew the actual diffusion coefficient D of the free biomolecules in the nucleoplasm then it would be possible to calculate the proportion of bound biomolecules that is causing the reduced overall mobility, and, conversely, if one knew the proportion of bound biomolecules, then it would be possible to estimate the diffusion coefficient D of free biomolecules.

When falling in one of the two previous cases, the parameter estimation does not require the explicit solution for the reaction-diffusion equation (3.1) or the compartmental model (4.1). The great advantage of this stems not only from the simplicity of the approximated theoretical recovery curves (5.25), (5.35), (5.68), or (5.73) used to fit the data, but also from the fact that these theoretical recovery curves allow one to appraise the contribution of the dynamical processes involved, namely the random walk movement and the turnover binding-unbinding process. In general, if the fluorescence recovery does not exhibit clearly any of the previous behaviours, then one can use the explicit solution of the reaction-diffusion model (3.1) or the compartmental model (4.1) to obtain a theoretical recovery curve to fit the data (chapters 3 and 4).

In conclusion, we have provided a mathematical analysis that enriches the interpretation of FRAP data and simplifies the task of obtaining measurements of the mobility of proteins and their binding interactions.

Chapter 6

Modelling the Compartmentalization of Splicing Factors with an Aggregation-Reaction-Diffusion Model

The structure of eukaryotic cells is characterized by the presence of two intracellular compartments, namely the cytoplasm and the nucleus. While the structural and functional organization of the cytoplasm is well defined, the nucleus has been more enigmatic. This is principally due to the absence of membranes that define compartments within the nucleoplasm. For example, cellular organelles in the cytoplasm such as the endoplasmic reticulum, the Golgi apparatus, and the mitochondria have been clearly identified, whereas the nature of structures and compartments within the nucleoplasm remains poorly understood. With recent advances in fluorescence microscopy techniques, and the visualization of specific proteins within the nucleus, the structural organization of the nucleus has started to unfold. In particular, fluorescence microscopy has allowed for the identification of subnuclear structures

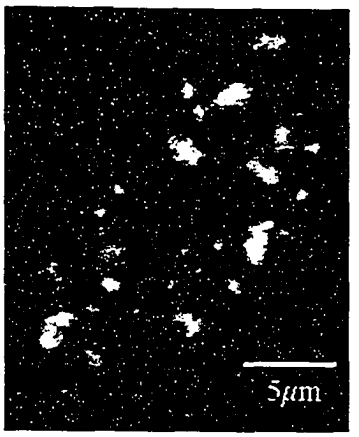

Figure 6.1: An indirect immunofluorescence image of the "speckled" distribution of the splicing factor SC-35 in an Indian Muntjac Fibroblast cell nucleus. The image was obtained at Dr. Hendzel's lab at the Cross Cancer Institute, University of Alberta, by staining cells with an antibody against SC-35.

or compartments [21, 48, 60, 97, 98]. These compartments differ from most cytoplasmic compartments in that they lack membrane boundaries. However, the identification of nuclear domains enriched in specific proteins has led to the conclusion that the nucleus itself is highly organized and dynamically compartmentalized [21, 36, 48, 52, 67, 87, 98].

The prototypical example of a non-nucleolar compartment is found in the spatial organization of splicing factors. Splicing factors are nuclear proteins that remove introns (noncoding sequences in the genes) from precursor mRNA molecules in order to form the mature mRNA that will be transported to the cytoplasm. During the interphase of the cell cycle, splicing factors are concentrated in approximately 25 to 50 clusters; during mitosis, these clusters disassemble. These membraneless clusters or aggregates of splicing factors, which are heterogeneously distributed in a "speckled" pattern in the nucleus (see figure 6.1), are called Splicing Factor Compartments (SFC's) or nuclear speckles [46, 49, 87, 97, 98].

One might infer that co-localized processes of splicing and transcription occur within the speckles, but this is not the case. In fact, splicing and transcription take place away from the speckles and predominantly at their periphery [35, 42, 65, 68].

This suggests the existence of a mechanism independent of interactions established during RNA splicing that is responsible for reversibly recruiting splicing factors. In other words, the organization of splicing factors must be highly dynamic. Indeed, fluorescence microscopy experiments have shown that (1) splicing factors are in continuous flux between the speckles and the nucleoplasm [46, 67, 68, 87], and (2) splicing factors move randomly throughout the cell nucleus [83, 87].

These dynamical aspects have brought forth two current biological hypotheses for splicing factor compartmentalization, one relating to the role of phosphorylation and dephosphorylation in the formation and disassembly of SFC's, and the other relating to the existence of an underlying nuclear structure. First, recent experimental evidence obtained from SR proteins suggests that the flux between the speckles and the nucleoplasm is modulated by phosphorylation and dephosphorylation [6, 71, 72, 114]. SR proteins are a family of splicing factors containing a carboxy-terminal domain rich in argine-serine dipeptides (RS-domain) [25, 59], and the phosphorylation status (phosphorylated or unphosphorylated) of this domain plays a major role in their localization. In particular, overexpression of kinases that phosphorylate the RS-domains results in the release of splicing factors from spleckles and the disassembly of SFC's [13, 19, 28, 68, 71, 107]. In contrast, the reassociation of splicing factors to SFC's requires the presence of specific phosphatases responsible for the removal of a phosphate group [70, 71]. Moreover, the unphosphorylated state of splicing factors enhances their self-interaction (binding), whereas the phosphorylated state diminishes it [114]. Understanding the role of phosphorylation in the location of splicing factors and the existence of self-interacting domains (RS-domains) [6, 113, 114] has led to the following hypothesis for splicing factor compartmentalization: self-organization is responsible for the formation of speckles, and phosphorylation and dephosphorylation modulate this organization.

Second, measurements of the mobility of splicing factors show that they move at a rate that is two orders of magnitude lower than expected based on their molecular weight [87]. A possible explanation for this apparent slow mobility of splicing factors is rapid transient binding to a relatively immobile nuclear scaffold or nuclear

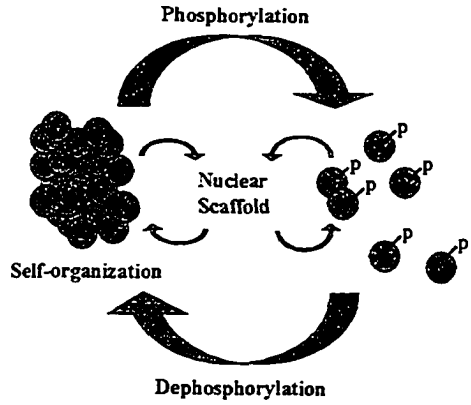

Figure 6.2: Mechanism for the compartmentalization of splicing factors. The thin arrows describe the transient binding of splicing factors to a nuclear scaffold or matrix, and the thick arrows represent the phosphorylation and dephosphorylation that modulate the flux between the speckles and the nucleoplasm. The self-interaction among dephosphorylated splicing factors leads to their self-organization into speckles, whereas phosphorylated splicing factors don't self-interact. Adapted from figure 3A in [65].

matrix [7, 33, 34, 46, 50, 79, 80, 108]. This idea has led to the following hypothesis for splicing factor compartmentalization: the existence of an underlying nuclear structure is a major determinant of the organization of splicing factors [34, 47, 80].

The dynamical aspects of splicing factors and their heterogeneous distribution in speckles provide strong evidence that there is more to the spatio-temporal dynamics of splicing factors than just simple diffusion. To unravel the mechanism underlying the organization of splicing factors, we incorporate the two existing biological hypotheses for splicing factor compartmentalization into a mathematical model. Unlike the current thinking that these two hypotheses are conflicting [49], we will see that they can, indeed, complement each other in a possible mechanism responsible for the compartmentalization of splicing factors (see figure 6.2). We use the model to suggest answers to a number of fundamental questions about SFC's [49, 65, 66]. What is the detailed mechanism of splicing factor compartmentalization? What controls the concentration of splicing factors inside and outside the speckles? Is speckle formation initiated randomly? What determines the number

and size of SFC's?

The model we derive is a fourth-order aggregation-reaction-diffusion model that describes a possible mechanism underlying the organization of splicing factors in speckles (section 6.1). Using linear stability analysis, we show how the onset of splicing factor compartmentalization is captured by the model (section 6.2), and using bifurcation analysis, we explain how the compartmentalization of splicing factors is modulated by the dynamical parameters of the model (section 6.3). We conclude the chapter with a discussion of the relevance of the results and possible directions of future work (section 6.4).

6.1 The Model

In order to formulate a simple model that can capture the essence of splicing factor compartmentalization, we accommodate the biological hypotheses stated previously into the following general assumptions:

1. Splicing factors (SF's) transiently bind to an immobile underlying nuclear scaffold that is assumed to be homogeneously distributed throughout the nucleus.

2. Transient binding is rapid, and results in reduced diffusive behaviour in the context of FRAP (Fluorescence Recovery After Photobleaching) experiments [9], or instantaneous reaction in the context of chemical kinetics [16]. This assumption allows us to characterize the motion of SF's with an effective diffusion coefficient $D = (1-k)D_b$, where k is the proportion of SF's dynamically bound to the underlying structure, and D_b is the actual diffusion coefficient of SF's based on their molecular weight.

3. There is no net growth of splicing factors, i.e., there is conservation of mass during the formation of speckles.

4. SF's density is divided into two classes, namely phosphorylated SF's, $v(x,t)$, and unphosphorylated SF's, $u(x,t)$, where x denotes space and t denotes time.

5. There is an exchange rate between phosphorylated splicing factors and unphosphorylated splicing factors given by a phosphorylation rate, ρ, and a dephosphorylation rate, δ, caused by the activity of kinases or phosphatases, respectively.

6. Unphosphorylated splicing factors are capable of self-interaction (binding to each other).

On the basis of these general assumptions, and considering a one-dimensional space, the resulting system of equations for the dynamical organization of splicing factors takes the following form

$$\begin{aligned} \frac{\partial v}{\partial t} &= D\frac{\partial^2 v}{\partial x^2} - \delta v + \rho u\,, \\ \frac{\partial u}{\partial t} &= \text{(motion and self-interaction term)} + \delta v - \rho u\,, \end{aligned} \tag{6.1}$$

where the "motion and self-interaction term" for the density of unphosphorylated SF's needs to be fleshed out. To find an exact expression for this term, we follow a diffusion-approximation approach [103], which is based on a random walk analysis that accounts for both the motion and self-interaction effects. This type of approach has been proven to be an effective tool when describing congregative behaviour in ecological systems [53, 103].

Let us assume that unphosphorylated splicing factor biomolecules move along a line that is discretized into small space intervals of length λ. Let us also discretize time into short intervals of length τ, and assume that every time step τ a biomolecule located at position x at time t can move a distance of λ either to the left with probability $L(x,t)$, to the right with probability $R(x,t)$, or remain in its current position with probability $N(x,t)$. Thus, the probability of moving is given by

$$R(x,t) + L(x,t) = 1 - N(x,t)\,. \tag{6.2}$$

We further assume that there is no bias in the movement, i.e., $R(x,t) = L(x,t)$. Following the procedure in [104], we arrive at the following diffusion approximation model for the density of unphosphorylated SF's

$$\frac{\partial u(x,t)}{\partial t} = D\frac{\partial^2}{\partial x^2}\left[(1 - N(x,t))\,u\right] = \frac{\partial^2}{\partial x^2}\left[\mu(x,t)\,u\right]\,, \tag{6.3}$$

where $D = (1-k)D_b = \lim_{\lambda,\tau\to 0} \frac{\lambda^2}{2\tau}$, and $\mu(x,t) = D(1-N(x,t))$ represents the motility.

As a final step, we need to develop an expression for $N(x,t)$. For this purpose, we assume that the probability $N(x,t)$ for an unphosphorylated biomolecule to remain in its current position is proportional to the average density of unphosphorylated SF's bound to the underlying structure, and is given by

$$N(x,t) = \frac{\kappa}{\omega} \int_{-\infty}^{\infty} H(s)\, u(x+s,t)\, ds\,, \tag{6.4}$$

where ω represents a critical density of biomolecules dictated by space limitations, $\kappa = k\,\alpha$ is called the aggregative sensitivity, k is the proportion of SF's dynamically bound to the underlying structure, α represents the binding affinity of SF's (probability of binding to each other), and the kernel function $H(s)$ is assumed to have the following form

$$H(s) = \begin{cases} \dfrac{1}{2\sigma} & for \quad |s| \le \sigma\,, \\ 0 & for \quad |s| > \sigma\,, \end{cases} \tag{6.5}$$

where σ denotes the range of influence of the self-interaction. Note that with equation (6.4), the model (6.1) now becomes nonlinear. Also, note that $N(x,t) \le 1$ provided that

$$u(x,t) < \omega\,, \tag{6.6}$$

i.e., $u(x,t)$ does not exceed the critical density ω. We shall see that this condition is satisfied during the onset of the compartmentalization, but when aggregation is pronounced, the density may exceed ω, and the model will no longer be valid. We will return to this issue in the discussion.

The diffusion approximation model (6.3) falls into the class of integro-differential equations. Such equations have been shown to have rich dynamics, including potential for pattern-formation [53, 73, 74, 75, 76, 77, 104]. We will take the approach used in [53, 77, 104] and expand the integral term in equation (6.3) for the stability analysis. This approach is not essential. The same results can be obtained by taking

an alternate approach such as the one used in [74, 75], where the integral term is not expanded and the consideration of normal mode solutions in the linear stability analysis leads to the appearance of the Fourier transform of the kernel $H(s)$.

Using the expansion in Taylor series

$$u(x+s,t) = u(x,t) + \frac{\partial u}{\partial x}s + \frac{\partial^2 u}{\partial x^2}\frac{s^2}{2} + \frac{\partial^3 u}{\partial x^3}\frac{s^3}{6} + O(s^4)\,,$$

and the expression of the kernel (6.5), the probability of staying (6.4) becomes

$$N(x,t) = \frac{\kappa u(x,t)}{\omega} + \frac{\kappa\sigma^2}{6\omega}\frac{\partial^2 u}{\partial x^2} + O(\sigma^4)\,. \tag{6.7}$$

Assuming that the range of influence σ is small and neglecting the fourth-order and higher-order terms with respect to σ, the motility, $\mu(x,t) = D(1-N(x,t))$, can be approximated by

$$\mu(x,t) = D - D\frac{\kappa u(x,t)}{\omega} - D\frac{\kappa\sigma^2}{6\omega}\frac{\partial^2 u}{\partial x^2}(x,t)\,. \tag{6.8}$$

Substituting (6.8) into (6.3), the diffusion approximation for the density of unphosphorylated SF's can be written as the following fourth-order partial differential equation:

$$\frac{\partial u}{\partial t} = \frac{\partial}{\partial x}\left[\left(D - 2D\kappa\frac{u}{\omega}\right)\frac{\partial u}{\partial x}\right] - \frac{\partial^2}{\partial x^2}\left[\left(\frac{D\kappa\sigma^2}{6}\frac{u}{\omega}\right)\frac{\partial^2 u}{\partial x^2}\right]\,, \tag{6.9}$$

which represents the motion and self-interaction term in equation (6.1). We refer to equation (6.9) as the aggregation-diffusion equation. Thus, the system of partial differential equations describing the compartmentalization of SF's becomes

$$\begin{aligned}
\frac{\partial v}{\partial t} &= D\frac{\partial^2 v}{\partial x^2} - \delta v + \rho u\,,\\
\frac{\partial u}{\partial t} &= \frac{\partial}{\partial x}\left[\left(D - 2D\kappa\frac{u}{\omega}\right)\frac{\partial u}{\partial x}\right] - \frac{\partial^2}{\partial x^2}\left[\left(\frac{D\kappa\sigma^2}{6}\frac{u}{\omega}\right)\frac{\partial^2 u}{\partial x^2}\right] + \delta v - \rho u\,.
\end{aligned} \tag{6.10}$$

We refer to equation (6.10) as the aggregation-reaction-diffusion system.

The cell nucleus is a domain bounded by a membrane. For this reason, we assume a bounded domain, $0 \le x \le L$, with no net flux of splicing factors across

the boundaries. This is achieved by considering the following no-flux boundary conditions

$$\begin{aligned} &\frac{\partial v}{\partial x}(0,t) = \frac{\partial v}{\partial x}(L,t) = \frac{\partial u}{\partial x}(0,t) = \frac{\partial u}{\partial x}(L,t) = 0\,, \\ &\frac{\partial^3 u}{\partial x^3}(0,t) = \frac{\partial^3 u}{\partial x^3}(L,t) = 0\,. \end{aligned} \tag{6.11}$$

In order to facilitate the analysis and reduce the number of parameters, we introduce the following dimensionless variables:

(6.12)

$$x^* = \frac{x}{L},\quad t^* = \frac{D}{L^2}t,\quad v^* = 2\kappa\frac{v}{\omega},\quad u^* = 2\kappa\frac{u}{\omega},\quad \sigma^* = \frac{\sigma}{L},\quad \delta^* = \frac{L^2}{D}\delta,\quad \rho^* = \frac{L^2}{D}\rho\,.$$

After making these substitutions and dropping the asterisks, the aggregation-diffusion equation (6.9) becomes

$$\frac{\partial u}{\partial t} = \frac{\partial}{\partial x}\left[(1-u)\frac{\partial u}{\partial x}\right] - \frac{\partial^2}{\partial x^2}\left[\left(\frac{\sigma^2}{12}u\right)\frac{\partial^2 u}{\partial x^2}\right]\,, \tag{6.13}$$

subject to the no-flux boundary condition

$$\begin{aligned} &\frac{\partial u}{\partial x}(0,t) = \frac{\partial u}{\partial x}(1,t) = 0\,, \\ &\frac{\partial^3 u}{\partial x^3}(0,t) = \frac{\partial^3 u}{\partial x^3}(1,t) = 0\,, \end{aligned} \tag{6.14}$$

and the aggregation-reaction-diffusion system (6.10) can be rewritten in a dimensionless form as

$$\begin{aligned} &\frac{\partial v}{\partial t} = \frac{\partial^2 v}{\partial x^2} - \delta v + \rho u\,, \\ &\frac{\partial u}{\partial t} = \frac{\partial}{\partial x}\left[(1-u)\frac{\partial u}{\partial x}\right] - \frac{\partial^2}{\partial x^2}\left[\left(\frac{\sigma^2}{12}u\right)\frac{\partial^2 u}{\partial x^2}\right] + \delta v - \rho u\,, \end{aligned} \tag{6.15}$$

subject to the no-flux boundary conditions

$$\begin{aligned} &\frac{\partial v}{\partial x}(0,t) = \frac{\partial v}{\partial x}(1,t) = \frac{\partial u}{\partial x}(0,t) = \frac{\partial u}{\partial x}(1,t) = 0\,, \\ &\frac{\partial^3 u}{\partial x^3}(0,t) = \frac{\partial^3 u}{\partial x^3}(1,t) = 0\,. \end{aligned} \tag{6.16}$$

Since self-organization appears to be driven by the dynamics of the unphosphorylated SF's, described by the aggregation-diffusion equation (6.9), our first interest

will be to demonstrate the potential of this equation for the spontaneous formation of spatial patterns (section 6.2). These patterns, which are a consequence of the nonhomogeneous distribution of biomolecules, can be interpreted as splicing factor compartments or speckles, where the density of biomolecules is high. In section 6.3, we focus on the aggregation-reaction-diffusion system (6.10), and study the modulating effect of phosphorylation on the compartmentalization of SF's. From the first equation in (6.10), we intuitively expect the modulation to be driven by the homogenizing effect of the spatial diffusion of phosphorylated SF's.

6.2 The Onset of the Compartmentalization of SF's

The potential of equation (6.15) for spatial pattern formation is interpreted as the onset of splicing factor compartmentalization during early G1. We can assert intuitively that no patterns will arise if there are no unphosphorylated SF's. For this reason, and to start the analysis as simple as possible, we will capture the essence of the onset of the compartmentalization by examining first the dynamics of just unphosphorylated SF's in the absence of phosphorylated ones. By carrying out a linear stability analysis about the homogeneous steady-state solutions of the aggregation-diffusion equation (6.13) subject to the boundary conditions (6.14), we will examine the behaviour of perturbations, and determine whether there are wave numbers with the ability to grow.

6.2.1 Dispersion Relation for the Aggregation-Diffusion Equation

The uniform steady states of (6.13) are given by any constant density u_{eq}. Thus, using the assumption of conservation of mass, we can think of the uniform steady state u_{eq} as a parameter that varies according to the amount of biomolecules in the system. Let us consider small perturbations of the biomolecule density $u(x,t)$ away from the spatially uniform steady state u_{eq}, of the form

$$u(x,t) = u_{eq} + \varepsilon \overline{u}(x,t) \ , \quad \text{where } \varepsilon \ll 1 \ . \tag{6.17}$$

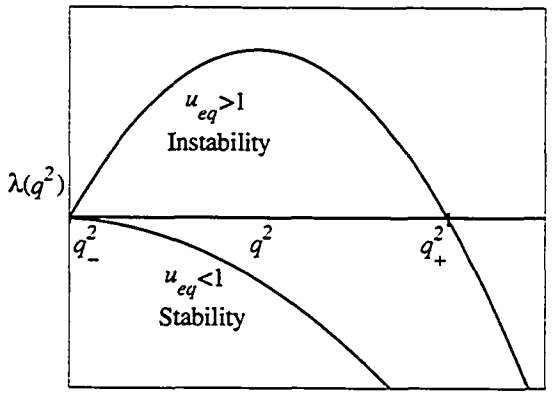

Figure 6.3: Dispersion relation λ as a function of q^2 (equation (6.20)).

Substituting (6.17) into (6.13) yields

$$\varepsilon \frac{\partial \overline{u}}{\partial t} = \frac{\partial}{\partial x}\left[(1 - u_{eq} - \varepsilon\overline{u})\,\varepsilon\frac{\partial \overline{u}}{\partial x}\right] - \frac{\partial^2}{\partial x^2}\left[\left(\frac{\sigma^2}{12}(u_{eq} + \varepsilon\overline{u})\right)\varepsilon\frac{\partial^2 \overline{u}}{\partial x^2}\right] .$$

Dividing this expression by ε, dropping the bars, and noting that $\varepsilon \ll 1$, we obtain the following linearization for the aggregation-diffusion equation (6.13):

$$\frac{\partial u}{\partial t} = (1 - u_{eq})\frac{\partial^2 u}{\partial x^2} - \frac{\sigma^2}{12}u_{eq}\frac{\partial^4 u}{\partial x^4} . \tag{6.18}$$

To investigate the behaviour of solutions for the linearized equation (6.18), we study the normal mode solutions of the form

$$u(x,t) \propto \exp(\lambda t + i\,qx) , \tag{6.19}$$

where λ is the growth rate corresponding to the wave number q. Thus, wavenumbers q with a corresponding $\lambda > 0$ will grow with wavelength $2\pi/q$.

Substitution of (6.19) into the linearized equation (6.18) gives the following dispersion relation between λ and q:

$$\lambda = (u_{eq} - 1)q^2 - \frac{\sigma^2}{12}u_{eq}\,q^4 , \tag{6.20}$$

which is shown as a function of q^2 in figure 6.3. The potential for pattern formation is determined simply by the fundamental condition $\lambda > 0$. Note that for the limit case $\sigma = 0$, the kernel (6.5) corresponds to a delta distribution centered at the current position of the biomolecule, and the dispersion relation increases or decreases monotonically with respect to q, depending on whether $u_{eq} > 1$ or $u_{eq} < 1$.

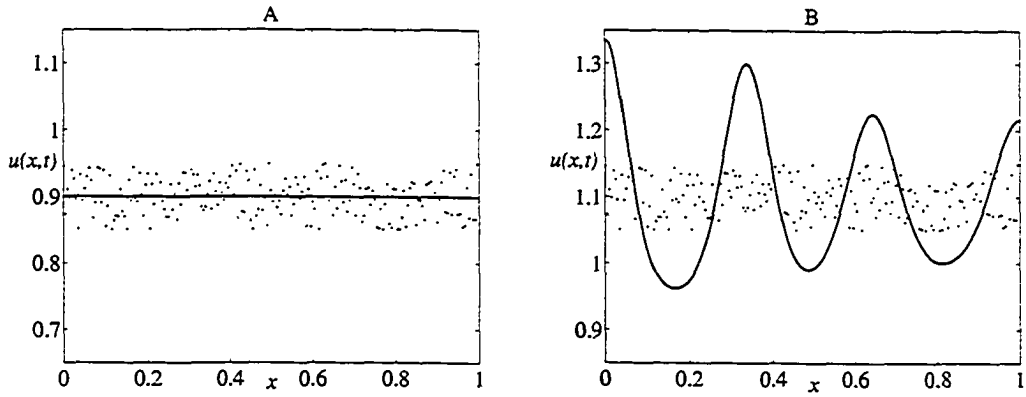

Figure 6.4: Evolution of the solution $u(x,t)$ of equation (6.13) for $\sigma = 0.04$ after a random perturbation of the steady state u_{eq} (represented by the dots). In figure (A), the simulation describes the stable steady state $u_{eq} = 0.9 < 1$, and the solid curve represents the solution $u(x,t)$ for $t = 3$. In figure (B), the simulation describes the unstable steady state $u_{eq} = 1.1 > 1$, and the solid line represents the solution $u(x,t)$ for $t = 0.25$.

Therefore, the smaller the perturbation wavelengths the faster they will grow, which means that the problem is ill-posed in the sense of Hadamard [116]. For this reason, we account for the realistic biological assumption that biomolecules can be influenced by other nearby biomolecules and consider only the case $\sigma > 0$, in which small wavelengths, characterized by high q, do not grow. The main requirement for λ to correspond to growing wave numbers is that $u_{eq} > 1$ (see figure 6.3) . In other words, the population of unphosphorylated SF's has to be large enough for pattern formation to occur. Otherwise, u_{eq} becomes a stable steady state.

In order to illustrate these stability scenarios, we have used MATLAB to implement the numerical scheme for fourth-order non-linear partial differential equations developed in [15] to perform two numerical simulations, one in which $u_{eq} < 1$, where stability is obtained (figure 6.4-A), and another for $u_{eq} > 1$, where instability leads to a potential spatial pattern (figure 6.4-B). Note that as a dimensionless parameter, u_{eq} has buried the dimensional parameter κ. Thus, the larger κ is, the more likely it is that pattern formation occurs; hence κ is called the aggregative sensitivity. Recalling that $\kappa = k\alpha$, the analysis suggests that the onset of the compartmen-

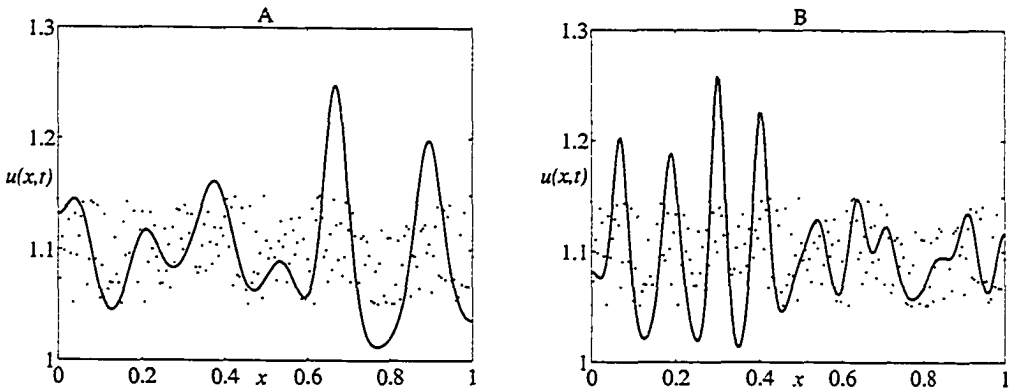

Figure 6.5: Evolution of the solution $u(x,t)$ of equation (6.13) after a random perturbation (represented by the dots) of the steady state $u_{eq} = 1.1$. In figure (A), the solid curve represents the solution $u(x,t)$ for $\sigma = 0.02$ at $t = 0.05$. In figure (B), the solid line represents the solution $u(x,t)$ for $\sigma = 0.012$ at $t = 0.01$.

talization is enhanced by the affinity of the interaction, α, as well as by a large proportion k of biomolecules bound to the underlying nuclear structure.

6.2.2 The Onset of Spatial Patterns

In order to gain a better understanding of how the spatial patterns start to arise, we study the dispersion relation (6.20) in more depth and determine which is the fastest growing wavelength (or equivalently, the dominating wave number), and examine the effect of different values of the parameter σ on the onset of the aggregation.

First, note that the only possible perturbations that satisfy the no-flux boundary conditions (6.14) on the domain $(0,1)$ are those whose wavenumbers take the discrete values

$$q_n = n\pi\,, \quad \text{where} \quad n = 0, 1, 2, \ldots\,. \tag{6.21}$$

From figure 6.3, we know that when $u_{eq} > 1$, λ as a function of q^2 has two zeroes, namely

$$q_-^2 = 0\,, \quad \text{and} \quad q_+^2 = \frac{12(u_{eq}-1)}{\sigma^2 u_{eq}}\,. \tag{6.22}$$

Therefore, the modes with positive growth rate (modes of instability) are given

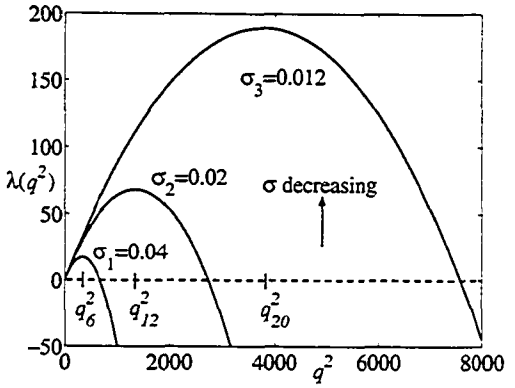

Figure 6.6: Dispersion relation (6.20) for $u_{eq} = 1.1$ and three values of σ: $\sigma_1 = 0.04$, $\sigma_2 = 0.02$, and $\sigma_3 = 0.012$.

by the wave numbers satisfying

$$q_-^2 < q_n^2 < q_+^2 \,. \tag{6.23}$$

Moreover, λ as a function of q^2 reaches a maximum at

$$q_{max}^2 = \frac{6(u_{eq}-1)}{\sigma^2 u_{eq}} \,. \tag{6.24}$$

Thus, the dominating wave number q_m, with $m \in \mathbb{N}$, is a wave number of an unstable mode, such that

$$|\lambda(q_m^2) - \lambda(q_{max}^2)| = \min_{q_-^2 < q_n^2 < q_+^2} \{|\lambda(q_n^2) - \lambda(q_{max}^2)|\} \,, \tag{6.25}$$

and the corresponding fastest growing wavelength of the spatial pattern that starts to evolve from the perturbation is

$$l_m = \frac{2\pi}{q_m} = \frac{2}{m} \,. \tag{6.26}$$

Note from equations (6.24)-(6.26) that $l_m \propto \sigma$, which means that initially after perturbation the longitude of the speckles or compartments is directly related to the scale of σ. This is illustrated in the numerical simulations shown in figure 6.4B and figure 6.5. These figures show the evolution of a random perturbation about a homogeneous steady state for various values of σ. The plot of the corresponding dispersion relations are shown in figure 6.6, and the numerical information gathered

σ	dominating wave number	dominating wavelength	growth rate	expected # of peaks
0.04	6π	$2/6 \approx 0.33$	$\lambda(q_6^2) \approx 17$	3
0.02	12π	$2/12 \approx 0.16$	$\lambda(q_{12}^2) \approx 68$	6
0.012	20π	$2/20 \approx 0.1$	$\lambda(q_{20}^2) \approx 189$	10

Table 6.1: Dominating wave numbers and wavelengths for the perturbations shown in figure 6.4B and figure 6.5 for different values of σ.

from them is arranged in table 6.1. Notice that as σ decreases, the dominating wavelength l_m decreases (or equivalently, the dominating wave number q_m increases), and the growth rate increases. In other words, the larger σ is, the fewer the speckles or compartments.

6.3 Modulating the Compartmentalization

In this section, we incorporate the phosphorylated population into the analysis and study its modulating effect on the compartmentalization of SF's. We carry out a linear stability analysis about the homogeneous steady state solutions of the aggregation-reaction-diffusion system (6.15) and perform a bifurcation analysis to understand how the phosphorylation and dephosphorylation rates modulate the formation of speckles.

6.3.1 Dispersion Relation for the Aggregation-Reaction-Diffusion System

From equation (6.15), positive uniform steady states (v_{eq}, u_{eq}) are given by points in the first quadrant of the $u\,v$-plane satisfying

$$u = \frac{\delta}{\rho} v \,. \tag{6.27}$$

Moreover, by introducing a new parameter

$$C = \int_0^1 (u_{eq} + v_{eq})\, dx = u_{eq} + v_{eq} \,, \tag{6.28}$$

representing the fixed amount of biomolecules in the system, the uniform steady (v_{eq}, u_{eq}) of (6.15) is determined by the intersection in the $v\,u$-plane of the straight line given by (6.27) and the straight line

$$u + v = C\,. \tag{6.29}$$

Therefore,

$$(v_{eq}, u_{eq}) = \left(\frac{\rho}{\rho+\delta}, \frac{\delta}{\rho+\delta}\right) C\,. \tag{6.30}$$

In order to assess the influence of the dynamical parameters of system (6.15) on the formation of speckles, we will consider small perturbations from the spatially homogeneous steady state (v_{eq}, u_{eq}) of the form

$$\begin{aligned} v &= v_{eq} + \varepsilon \overline{v}(x,t)\,, \\ u &= u_{eq} + \varepsilon \overline{u}(x,t)\,, \end{aligned} \tag{6.31}$$

where $\varepsilon \ll 1$. Substitution of these perturbations into (6.15) yields

(6.32)

$$\varepsilon \frac{\partial \overline{v}}{\partial t} = \varepsilon \frac{\partial^2 \overline{u}}{\partial x^2} - \delta\,\varepsilon\,\overline{v} + \rho\,\varepsilon\,\overline{u}\,,$$

$$\varepsilon \frac{\partial \overline{u}}{\partial t} = \frac{\partial}{\partial x}\left[(1 - u_{eq} - \varepsilon\overline{u})\,\varepsilon \frac{\partial \overline{u}}{\partial x}\right] - \frac{\partial^2}{\partial x^2}\left[\left(\frac{\sigma^2}{12}(u_{eq} + \varepsilon\overline{u})\right)\varepsilon \frac{\partial^2 \overline{u}}{\partial x^2}\right] + \delta\,\varepsilon\,\overline{v} - \rho\,\varepsilon\,\overline{u}\,.$$

Equating first-order terms with respect to ε, neglecting higher-order terms, and dropping the bars, we obtain the following linearized system for (6.15) :

$$\begin{aligned} \frac{\partial v}{\partial t} &= \frac{\partial^2 v}{\partial x^2} - \delta v + \rho u\,, \\ \frac{\partial u}{\partial t} &= (1 - u_{eq})\frac{\partial^2 u}{\partial x^2} - \frac{\sigma^2}{12}\,u_{eq}\frac{\partial^4 u}{\partial x^4} + \delta v - \rho u\,. \end{aligned} \tag{6.33}$$

To find the dispersion relation between the growth rate λ and the wave number q and draw conclusions about the stability of uniform steady states of (6.15), we study the following normal mode solutions of the linear system (6.33) :

$$\begin{aligned} v(x,t) &= A\exp(\lambda t + i\,qx)\,, \\ u(x,t) &= B\exp(\lambda t + i\,qx)\,, \end{aligned} \tag{6.34}$$

where A and B are constants. Substitution of (6.34) into the linear system (6.33), cancellation of the factor $\exp(\lambda t + i\,qx)$, and proper rearrangement leads to

(6.35)
$$\begin{bmatrix} \lambda+\delta+q^2 & -\rho \\ -\delta & \lambda+\rho-(u_{eq}-1)q^2+\frac{\sigma^2}{12}u_{eq}q^4 \end{bmatrix} \begin{bmatrix} A \\ B \end{bmatrix} = L \begin{bmatrix} A \\ B \end{bmatrix} = \begin{bmatrix} 0 \\ 0 \end{bmatrix}.$$

For nonzero solutions, it is required that A and $B \neq 0$. Therefore, we require $\det(L) = 0$, giving the following quadratic equation for the growth rate:

$$\lambda^2 + \beta(q)\lambda + \gamma(q) = 0\,, \tag{6.36}$$

where

$$\begin{aligned} \beta(q) &= \frac{\sigma^2}{12}u_{eq}q^4 - (u_{eq}-2)q^2 + \rho + \delta \\ \gamma(q) &= \frac{\sigma^2}{12}u_{eq}q^6 + \left(\delta\frac{\sigma^2}{12}u_{eq} - u_{eq} + 1\right)q^4 + (\rho - \delta u_{eq} + \delta)q^2\,. \end{aligned} \tag{6.37}$$

The two roots of (6.36) are given by

$$\lambda_{1,2} = \frac{-\beta \pm \sqrt{\beta^2 - 4\gamma}}{2}\,. \tag{6.38}$$

The necessary and sufficient condition for the growth rate λ of the perturbations (6.34) to have positive real part is that $\beta < 0$ or $\gamma < 0$. Note that if $\beta \leq 0$ then $u_{eq} > 2$. In terms of the dimensional variables (see variables (6.12)), this implies that the density of unphosphorylated SF's exceeds the critical density ω, i.e., the restriction given by (6.6) is violated. For this reason we assume $\beta > 0$. Therefore, one of the roots in (6.38) always has negative real part and the dispersion relation for possible growing modes is determined by the other root

$$\lambda = \frac{-\beta + \sqrt{\beta^2 - 4\gamma}}{2}\,, \tag{6.39}$$

which will have positive real part if and only if $\gamma < 0$, where γ is as in (6.37).

For the purpose of simplifying the analysis of the dispersion relation, we will consider all the parameters in system (6.15) fixed except for the dephosphorylation rate δ. An analogous analysis could be carried out if the free parameter were the

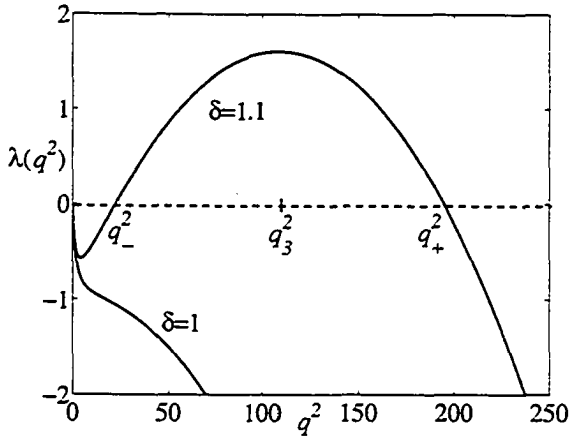

Figure 6.7: Dispersion relation (6.39), with $\delta = 1$ and $\delta = 1.1$, when $\sigma = 0.05$, $\rho = 1$, and $v_{eq} + u_{eq} = 2$. For the case $\delta = 1.1$, the modes of instability are determined by wave numbers q such that $q_-^2 < q^2 < q_+^2$, the dominating wave number is $q_3 = 3\pi$ with a growth rate $\lambda(q_3^2) \approx 1.5$, and the fastest growing wave length is $l_3 = 2/3$.

phosphorylation rate ρ. Note that varying δ affects the slope of (6.27), and consequently the value of the steady state (v_{eq}, u_{eq}). Thus, the natural question that arises is whether or not this variation affects the stability of the uniform steady state. In other words, we want to understand the influence of the dynamical parameter δ on the pattern forming potential of system (6.15).

The dispersion relation is visualized in figure 6.7 for two particular values of the dephosphorylation rate, namely $\delta = 1.1$, for which we obtain a dispersion relation defined by wave numbers with positive growth rates (modes of instabilities), and $\delta = 1$, for which the dispersion relation is defined by negative growth rates for all wave numbers. In other words, the uniform steady state (v_{eq}, u_{eq}) obtained with $\delta = 1.1$ is unstable and the evolving dynamics of its perturbation is characterized by the onset of spatial patterns, whereas the uniform steady state (v_{eq}, u_{eq}) obtained with $\delta = 1$ is stable and no spatial patterns will evolve. These stability results are corroborated by the numerical simulations shown in figures 6.8 and 6.9, respectively. The numerical scheme was implemented in MATLAB, where the "motion and self-interaction term" in (6.15) is treated with the scheme for fourth-order non-linear partial differential equations developed in [15], the diffusion term in the first equation

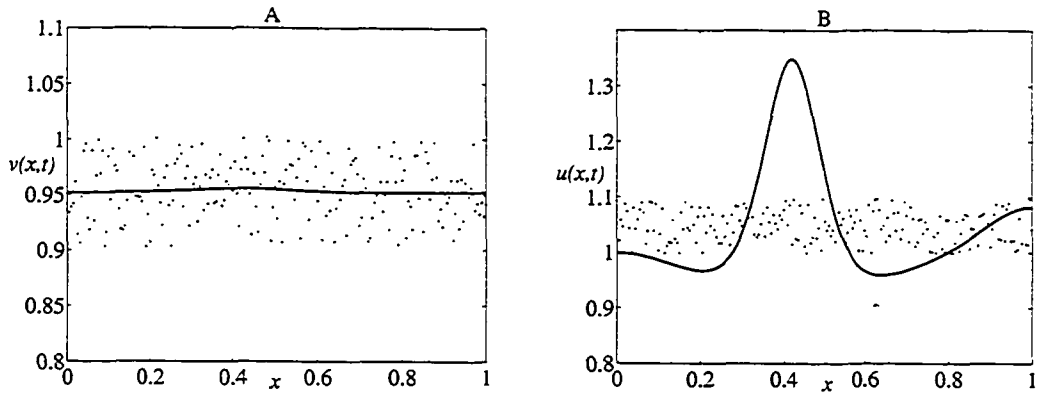

Figure 6.8: Evolution of the solution $(v(x,t), u(x,t))$ of system (6.15), with $\sigma = 0.05$, $\rho = 1$, and $\delta = 1.1$, from a random perturbation (represented by the dots) of the unstable steady state $(v_{eq}, u_{eq}) = (0.95, 1.05)$. The solid curves represent the solutions $v(x,t)$ and $u(x,t)$ at $t = 4$.

of (6.15) is treated implicitly, and the reaction terms are treated explicitly.

In the case of the aggregation-diffusion equation (6.13), we were able to use the dispersion relation (6.20) in order to find the dominating wave number q_m dictated by (6.24) and the fastest growing wavelength given by (6.26). But in the case of the aggregation-reaction-diffusion system (6.15), the complicated expression for the dispersion relation (6.39) has made the task of finding the dominating wave number very difficult. In spite of this, Hadeler and Hillen [29] were able to estimate the dominating wave number for system (6.15). Under the assumption that the turnover rate of phosphorylated and unphosphorylated splicing factors is fast, the authors approximated system (6.15) with a limiting model that was linearized in order to obtain an estimate of the dominating wave number for system (6.15).

6.3.2 Bifurcation Analysis. Instability and Stability Regions.

We investigate the modulating effect of the phosphorylation and dephosphorylation rates on the onset of the compartmentalization by addressing the question of how the transition from stability to instability takes place when the dephosphorylation rate is taken as the bifurcation parameter. We already know that this transition occurs when the real part of the dispersion relation λ, given by (6.39), becomes

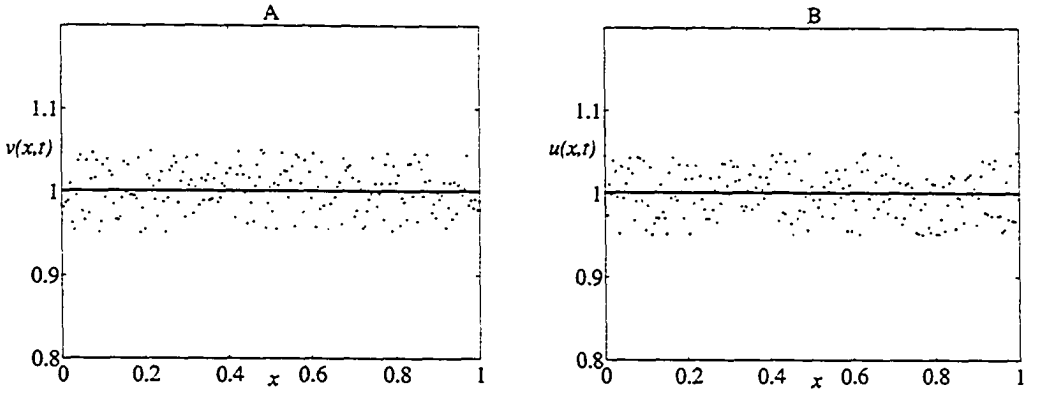

Figure 6.9: Evolution of the solution $(v(x,t), u(x,t))$ of system (6.15), with $\sigma = 0.05$, $\rho = 1$, and $\delta = 1$, from a random perturbation (represented by the dots) of the stable steady state $(v_{eq}, u_{eq}) = (1, 1)$. The solid curves represent the solutions $v(x,t)$ and $u(x,t)$ at $t = 4$.

positive. Equivalently, the transition occurs when γ, given by (6.37), becomes negative. Therefore, this transition is described by a real bifurcation [53]. To simplify the analysis of this bifurcation problem, we let both λ and γ be functions of $z = q^2$. From (6.30) and (6.37), it then follows that the roots of $\lambda(z)$ are determined by the positive roots of

$$\gamma(z) = zp(z) = z(az^2 + bz + c)\,, \tag{6.40}$$

where

$$\begin{aligned} a &= C\frac{\sigma^2}{12}\frac{\delta}{\delta+\rho}\,, \\ b &= C\frac{\delta}{\delta+\rho}\left(\frac{\delta\sigma^2}{12} - 1\right) + 1\,, \\ c &= \rho - C\frac{\delta^2}{\delta+\rho} + \delta\,, \end{aligned} \tag{6.41}$$

and C is as in equation (6.28). Thus, one of the roots of $\gamma(z)$ is zero, and the other roots are given by the roots of $p(z)$:

$$r_{1,2} = \frac{-b \pm \sqrt{b^2 - 4ac}}{2a}\,. \tag{6.42}$$

The following theorem provides details on the real bifurcation, plus an algorithm to determine the bifurcation value.

Theorem 4. Consider system (6.15), with uniform steady state (v_{eq}, u_{eq}) given by (6.30). Let the parameters $C, \rho, \sigma > 0$ be given, and

$$f(\delta) = b^2(\delta) - 4\,a(\delta)\,c(\delta)\,, \tag{6.43}$$

where $a(\delta)$, $b(\delta)$, and $c(\delta)$ are as in (6.41). Let δ^* denotes the largest root of $f(\delta)$, and $\overline{\delta} = \dfrac{(1+\sqrt{C})}{C-1}\rho$.

1. If $0 < C \leq 1$, then (v_{eq}, u_{eq}) is stable.

2. If $C > 1$, and

   (a) if $\rho > \dfrac{3(C-1)^2}{C\sigma^2}$ then (v_{eq}, u_{eq}) is stable for $\delta < \delta_b$ and unstable for $\delta > \delta_b$, where $\delta_b = \overline{\delta}$;

   (b) if $\rho \leq \dfrac{3(C-1)^2}{C\sigma^2}$, and

      (i) if $b(\delta^*) < 0$, then (v_{eq}, u_{eq}) is stable for $\delta < \delta_b$ and unstable for $\delta > \delta_b$, where $\delta_b = \delta^*$;

      (ii) if $b(\delta^*) \geq 0$, then (v_{eq}, u_{eq}) is stable for $\delta < \delta_b$ and unstable for $\delta > \delta_b$, where $\delta_b = \overline{\delta}$.

Proof. Since the roots of the dispersion relation $\lambda(x)$ are determined by the positive roots of $\gamma(x)$ and the coefficient $a(\delta) > 0$, the transition from a stable to an unstable steady state can only occur when $f(\delta) = 0$ or $c(\delta) = 0$. To distinguish these two cases, we note first that the coefficient $b(\delta) = 0$ if and only if $\rho = l(\delta)$, where

$$l(\delta) = -\frac{C\sigma^2}{12}\delta^2 + (C-1)\delta\,. \tag{6.44}$$

Note as well that $c(\delta) = 0$ if and only if $\rho = m_{\pm}(\delta)$, where

$$m_{\pm}(\delta) = \frac{C-1}{(1 \pm \sqrt{C})}\delta\,. \tag{6.45}$$

1. For $0 < C \leq 1$, the values of both (6.44) and (6.45) are negative. On the one hand, $l(\delta) < 0$ implies that $b(\delta) > 0$. The bifurcation cannot take place at any root of $f(\delta)$. If it did, the only root of $p(z)$ at the bifurcation point, given by (6.42), would be negative. On the other hand, the bifurcation cannot occur when $c(\delta) = 0$, because $\rho > 0$ and $m_{\pm}(\delta) < 0$. Therefore, (v_{eq}, u_{eq}) is stable for $0 < C \leq 1$.

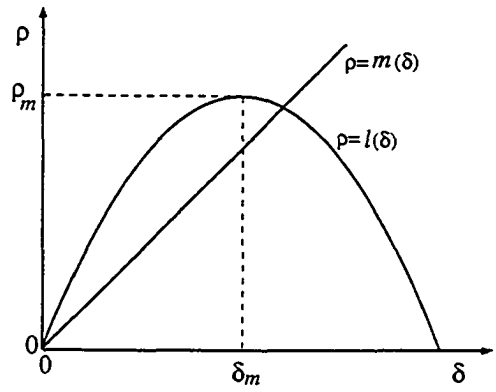

Figure 6.10: Graphs of the curves $l(\delta)$ and $m(\delta)$ given by (6.44) and (6.46), respectively.

2. For $C > 1$, the parabola $l(\delta)$ reaches a maximum value $\rho_m = \dfrac{3(C-1)^2}{C\sigma^2}$ at $\delta_m = \dfrac{6(C-1)}{C\sigma^2}$ (see figure 6.10) and $c(\delta) = 0$ if $\rho = m(\delta)$, where

$$m(\delta) = \frac{C-1}{(1+\sqrt{C})}\delta. \tag{6.46}$$

Since the slope of $m(\delta)$ is smaller than the slope of $l(\delta)$ at $\delta = 0$ and $m(\delta_m) < \rho_m$, the straight line $m(\delta)$ is as shown in figure 6.10.

(a) With figure 6.10 in mind, we conclude that if $\rho > \dfrac{3(C-1)^2}{C\sigma^2}$, then $b(\delta) > 0$ for all δ, and the bifurcation cannot occur at any root of $f(\delta)$. Thus, the bifurcation takes place when $c(\delta) = 0$, i.e., at $\delta_b = \dfrac{(1+\sqrt{C})}{C-1}\rho$.

(b) To study the case $\rho \leq \dfrac{3(C-1)^2}{C\sigma^2}$, we observe that the roots of $p(z)$, given by (6.42), are both negative when $\delta \ll 1$. As δ increases, we note from figure 6.10 that there is at least one value $\tilde{\delta}$ such that $b(\tilde{\delta}) = 0$ and $c(\delta) \neq 0$ for $\delta \leq \tilde{\delta}$. This means that at $\tilde{\delta}$, the roots (6.42) of $p(z)$ have distinct signs or are conjugate complex numbers. Therefore, the only possible way for this transition in the roots of $p(z)$ to happen as δ increases is that there exists a $\widehat{\delta} < \tilde{\delta}$ such that $f(\widehat{\delta}) = 0$, i.e., $f(\delta)$ has at least one root. Moreover, it is not difficult to see that all the roots of $f(\delta)$ are smaller than those of $c(\delta)$. Since we are interested in the bifurcation from a stable to an unstable steady state, and $f(\delta) \to \infty$ as $\delta \to \infty$, we let δ^* denote the largest root of $f(\delta)$. Thus, (i) if $b(\delta^*) < 0$, then the bifurcation occurs at $\delta_b = \delta^*$, and (ii) if $b(\delta^*) \geq 0$, then the root of $p(z)$ is negative and the bifurcation occurs

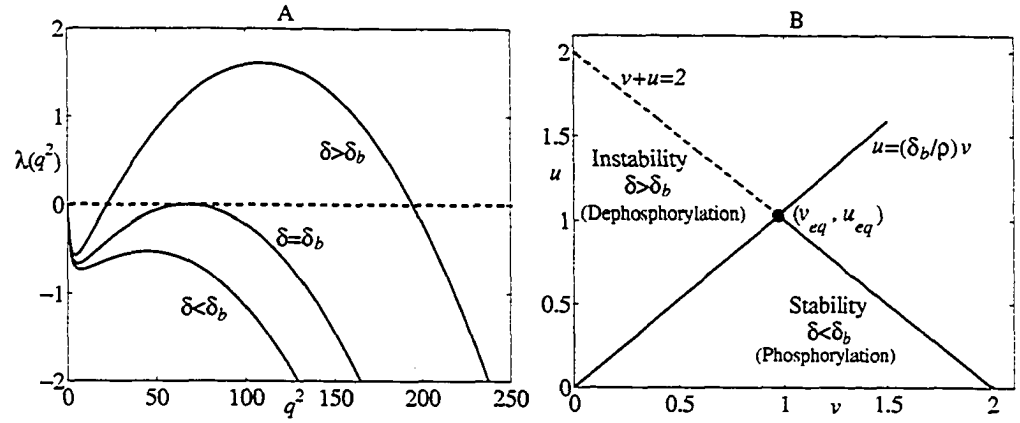

Figure 6.11: A: Evolution of the dispersion relation (6.39), with $\sigma = 0.05, \rho = 1, C = 2$, as δ passes through the bifurcation value $\delta_b \approx 1.06$. B: Bifurcation diagram for the stability of the steady state (v_{eq}, u_{eq}) as the dephosphorylation rate δ varies. The dotted portion of the line $v + u = 2$ represents unstable uniform steady states, the solid portion represents stable ones, and the filled circle represents the steady state at the bifurcation value δ_b.

when $c(\delta) = 0$, i.e., at $\delta_b = \overline{\delta}$. This completes the proof. □

To describe the use of theorem 4, we first find the bifurcation value δ_b for the example illustrated in figures 6.7-6.9, in which the dispersion relation becomes positive as the dephosphorylation rate δ increases. For the particular choice of the parameter values in the example ($\sigma = 0.05, \rho = 1, C = 2$), we note that $\rho = 1 < \dfrac{3(C-1)^2}{C\sigma^2} = 600$. The largest root of $f(\delta)$, defined in (6.43), is $\delta^* \approx 1.06$. Since $b(\delta^*) \approx -0.03 < 0$, case 2(b)(i) of theorem 4 applies, and the bifurcation value is given by $\delta_b = \delta^* \approx 1.06$. The evolution of the dispersion relation (6.39) as δ passes through δ_b is shown in figure 6.11A, which is consistent with the results in figures 6.7-6.9.

Figure 6.11B shows the bifurcation diagram for the steady state (v_{eq}, u_{eq}) obtained from the intersection of line (6.27), $u = \dfrac{\delta}{\rho} v$, and (6.29), $v+u = 2$. When δ is small, the steady state is stable (denoted by the solid portion of the line $v + u = 2$). The slope of line (6.27) increases as δ increases (or equivalently, decreases as ρ increases), and as it passes through the value δ_b/ρ, the resulting steady state becomes

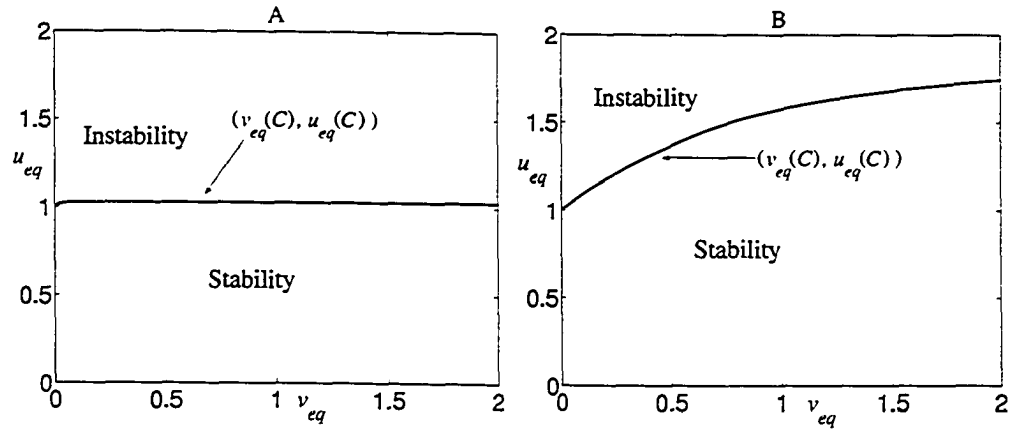

Figure 6.12: Stability and instability regions for the resulting steady state (v_{eq}, u_{eq}), with $\sigma = 0.05$. In figure A, $\rho = 1$ and the curve that separates the stability regions is given by equation (6.47). In figure B, $\rho > \frac{3(2-1)^2}{2\sigma^2}$ and the curve that separates the largest possible stability region to the instability region is given by equation (6.49).

unstable (denoted by the dotted portion of the line $v + u = 2$). The outcome is consistent with the biological fact that dephosphorylation (increased δ, or decreased ρ) enhances the self-organization of splicing factors, and that phosphorylation (increased ρ, or decreased δ) enhances the disassembly of speckles.

With the bifurcation diagram from figure 6.11B in mind, we can apply theorem 4 with any value of C. We consider values of $0 < C \leq 2$ to avoid breaking the restriction on the density of splicing factors given by (6.6). For each value of C, we obtain a bifurcation value $\delta_b(C)$, yielding the stability and instability regions for the steady state (v_{eq}, u_{eq}) shown in figure 6.12A. The uniform steady states that have the potential for pattern formation after perturbation lie in the instability region. The bifurcation curve

$$(v_{eq}(C), u_{eq}(C)) = \left(C\frac{\rho}{\rho+\delta_b}, C\frac{\delta_b}{\rho+\delta_b}\right) \tag{6.47}$$

that separates the regions of stability and instability in figure 6.12A lies slightly above the curve $u_{eq} = 1$. Thus, for the onset of the compartmentalization to take place, it is necessary to have enough biomolecules in the system ($C > 1$), and to have enough unphosphorylated biomolecules, which is consistent with the results

obtained in the analysis of the aggregation-diffusion equation (6.13), where it was required that $u_{eq} > 1$ for instability to occur. The natural question that arises now is how the bifurcation curve changes as the phosphorylation rate increases. As expected, the stability region will increase, but only up to a certain point. From case 2(a) of theorem 4, and considering that the bifurcation curve is given by equation (6.47), we conclude that the curve that separates the regions when $\rho > \dfrac{3(2-1)^2}{2\sigma^2}$ is given by the intersection of the line $v_{eq} + u_{eq} = C$ and the line $u_{eq} = r(C)v_{eq}$, where

$$r(C) = \frac{1+\sqrt{C}}{C-1}, \tag{6.48}$$

i.e., by the parameterized curve

$$(v_{eq}(C), u_{eq}(C)) = \left(\frac{C(C-1)}{C+\sqrt{C}}, \frac{C(1+\sqrt{C})}{C+\sqrt{C}} \right). \tag{6.49}$$

Therefore, the largest region of stability, reached when $\rho > \dfrac{3(2-1)^2}{2\sigma^2}$, will be determined by (6.49) (see figure 6.12B). This implies that no matter how big the phosphorylation rate is, there will always be a region of instability, i.e., there exists a dephosphorylation rate that is high enough such that the resulting uniform steady state (v_{eq}, u_{eq}) becomes unstable.

If one wants to obtain information on the modulating effect of both the phosphorylation and dephosphorylation rates at the same time, one can portray the regions of stability in the $\rho\,\delta$-plane. This is done by keeping the rest of the parameters in the system fixed and applying theorem 4 to any $\rho > 0$ to obtain the bifurcation curve $\delta_b(\rho)$, as follows:

$$\delta = \delta_b(\rho) = \begin{cases} \dfrac{1+\sqrt{C}}{C-1}\rho & ; \quad \rho > \dfrac{3(C-1)^2}{C\sigma^2}, \\ \delta^* & ; \quad \rho \leq \dfrac{3(C-1)^2}{C\sigma^2} \text{ and } b(\delta^*) < 0, \\ \dfrac{1+\sqrt{C}}{C-1}\rho & ; \quad \rho \leq \dfrac{3(C-1)^2}{C\sigma^2} \text{ and } b(\delta^*) \geq 0, \end{cases} \tag{6.50}$$

where δ^* and $b(\delta)$ are as in theorem 4. Figures 6.13A and 6.13B show this bifurcation curve and the resulting stability regions in the $\rho\,\delta$-plane when $\sigma = 0.05$, for $C = 2$ and $C = 1.5$, respectively. In figure 6.13B, note that decreasing the amount

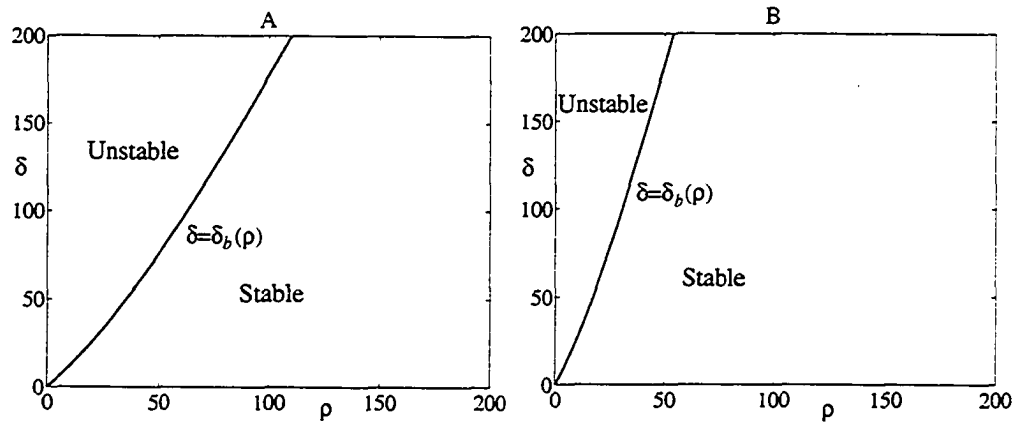

Figure 6.13: Stability and instability regions in the $\rho\delta$-plane when $\sigma = 0.05$, $C = 2$ (figure A), and $C = 1.5$ (figure B). The solid curve $\delta = \delta_b(\rho)$ that separates the stable region to the unstable region is obtained according to equation (6.50).

of biomolecules in the system, represented by C, has caused the region of instability to be reduced, i.e., there is a lower chance for the onset of compartmentalization of splicing factors.

In this section, we have demonstrated the existence of unstable uniform steady states of system (6.15), whose perturbation can result in the onset of the compartmentalization of splicing factors. Through the bifurcation analysis, we have concluded that the potential for the formation of compartments can be eliminated by increasing the phosphorylation rate or decreasing the amount of splicing factors in the system.

6.4 Discussion

Understanding the dynamical organization of splicing factors is an important step towards understanding the architecture of eukaryotic cell nuclei and the changes that take place under different physiological conditions or stresses. In this chapter, we have approached understanding nuclear compartmentalization using a mathematical model. In particular, we have proposed a model that describes a possible mechanism for the onset of splicing factors compartmentalization, i.e., for the formation of speckles. The model, namely the fourth-order aggregation-reaction-

diffusion equation (6.10), is based on the current biological hypotheses that self-organization of splicing factors is modulated by phosphorylation and dephosphorylation [6, 71, 72, 114], and that the existence of an underlying nuclear structure plays a major role in the formation of speckles [34, 47, 80]. Fourth-order partial differential equations have been shown to have rich dynamics, including potential for pattern-formation [15, 53, 103].

A linear stability analysis of the model and a study of its dispersion relation has brought to light a possible mechanism for the formation of speckles, in which slight perturbations of a uniform steady state of the system may lead to potential spatial patterns. This is possible as long as there are sufficient biomolecules in the cell nucleus. This result mimics the onset of the compartmentalization of splicing factors during the early stage of the cell interphase, when the distribution of splicing factors undergoes a transition from spatially homogeneous to heterogeneous [49], and suggests that speckle formation can be initiated randomly. Moreover, the model illustrates how the ratio between the size of the domain (cell nucleus) and the size of the range of influence of the self-interaction, defined by the dimensionless paramenter σ, can determine the number and size of SFC's. The larger σ is, the fewer the speckles or compartments.

The bifurcation analysis illustrates that an appropriate ratio of phosphorylation-dephosphoration rates is needed for speckles to form. An increase in the dephosphorylation rate leads to a larger region of instability, and therefore enhances the compartmentalization of splicing factors, whereas an increase in the phosphorylation rate leads to a small region of instability, and therefore has a homogenizing effect on the spatial distribution of splicing factors. This is consistent with naturally occurring processes that have been shown to lead to speckle disassembly, caused right before mitosis by an increase in kinase activity or induced experimentally by increasing the abundance of specific kinases [13, 19, 28, 68, 71, 107].

Although the model illustrates successfully a mechanism for the onset of the compartmentalization, the restriction given by (6.6) limits it from being able to describe the long-term behaviour for the aggregation of splicing factors. This has

left us with an interesting modelling problem to be investigated.

Chapter 7

Concluding Remarks

Advances in fluorescence microscopy techniques have become crucial to the study of the spatio-temporal dynamics of nuclear proteins. Thanks to this technology, the structural organization of the nucleus, and the functional biology and dynamics of nuclear proteins are becoming known. For example, with the use of fluorescence microscopy, the identification and study of nuclear compartments such as the splicing factor compartments have been possible [40, 46, 87]. Also, the fluorescence microscopy technique called FRAP (fluorescence recovery after photobleaching) and its accompanying mathematical analysis have become useful tools for studying dynamical properties of proteins within the nucleus of living cells. The combination of FRAP experiments and mathematical modelling allows experimentalists to estimate kinetic parameters that describe the processes affecting the movement of nuclear proteins.

In this thesis, we examined three models that can be used to interpret FRAP data for nuclear proteins, and developed one model that provides a possible mechanism for the formation of nuclear compartments enriched in splicing factors.

The first model used to interpret FRAP data is the diffusion equation (2.3), which is used to determine the overall mobility of biomolecules by estimating an effective diffusion coefficient [8, 58, 67]. The standard technique to estimate diffusion coefficients of nuclear proteins using FRAP experiments assumes that biomolecules diffuse on an two-dimensional infinite domain, where the photobleached region is

a circular area [1, 87]. However, the cell nucleus is a finite region bounded by a membrane. On the basis of the work by Axelrod *et al.* [1], we presented, in chapter 2, an exposition of how the diffusion equation is used in the analysis of FRAP data on both bounded and unbounded domains. We simplified the analysis of FRAP data by choosing rectangular photobleached regions. This allowed us to compare the behaviour of fluorescence recovery curves on bounded and unbounded domains, and to reduce the problem to a one-dimensional spatial domain. By solving the diffusion equation explicitly, we were able to derive the theoretical recovery curves on bounded and unbounded domains (equations (2.35)-(2.38)) that can be used to interpret FRAP data. The behaviour of these curves provided an explanation for the experimental differences in the fluorescence recovery curves that are observed depending on the size and the location of the photobleached region. We showed how disregarding the existence of a nuclear membrane can lead to erroneous estimations of effective diffusion coefficients, and concluded that the appropriate theoretical recovery curve to be used for estimating effective diffusion coefficients for nuclear proteins when photobleaching a band across the cell nucleus is the one obtained on a one-dimensional bounded domain, given by equation (2.42). This theoretical recovery curve was fit to FRAP data of two nuclear proteins, histone H1 and nuclear actin, in order to quantify their overall mobility in the cell nucleus.

The second model used to interpret FRAP data is the system of reaction-diffusion equations (3.1), which incorporates protein interactions in the analysis of FRAP data. In chapter 3, the model was used to describe the dynamics of diffusive fluorescent proteins in the cell nucleus undergoing binding and unbinding events with an approximate spatially homogeneous structure that is considered immobile on the time scale of molecular movement. Particular nuclear proteins of interest undergoing this type of interaction are histone H1, which binds to and unbinds from an approximately homogeneous chromatin structure, and actin, which is hypothesized to undergo an association-dissociation process between two pools, a globular pool of biomolecules free to diffuse and an approximately immobile and homogeneous polymeric population. By solving the reaction-diffusion system explicitly, we derived

the theoretical recovery curve (3.4) that can be used to fit experimental FRAP data and estimate the kinetic parameters that describe reversible binding interactions, namely the binding (association) and unbinding (dissociation) rates.

The theoretical recovery curve (3.4) was used to fit FRAP data of histone H1 and nuclear actin, and the estimated parameters were used to infer biologically meaningful information of the protein dynamics such as the protein residence time in a bound state, the wandering time between binding events, the proportion of the protein population that is bound, and the proportion that is free to diffuse.

For histone H1, the fitting was quite accurate, but the quantitative estimate obtained for the proportion of the population bound to the chromatin structure was much smaller than biologically expected, or equivalently, the proportion of the population free to diffuse was higher than expected. This apparent inconsistency suggested that the estimated high proportion of the population free to diffuse was actually a proportion of the population that accounted for a subpopulation weakly bound to the chromatin structure and a small proportion free to diffuse. Thus, we hypothesized that there are three subpopulations of histone H1, namely a subpopulation free to diffuse, a subpopulation weakly bound to the chromatin structure, and a subpopulation strongly bound to the chromatin structure. In other words, there are two types of binding interactions of histone H1 with the chromatin structure, namely a low-affinity (weak binding) interaction, and a high-affinity (strong binding) interaction, and that it is only the latter contributing to the low estimated proportion of bound population. The hypothesis is consistent with the experimental evidence of a rapid exchange (weak interaction) of histone H1 on chromatin [51].

In the case of nuclear actin, the FRAP data exhibited biphasic behaviour, with a fast initial recovery followed by a slow final recovery, which could not be explained by just the diffusion equation. Using the reaction-diffusion model (3.1), we obtained an accurate fitting of the FRAP data, whose fast and slow phases were attributed to the fast diffusion and to the slow turnover of globular actin into an immobile filamentous population, respectively. Using the estimated kinetic parameters from the fitting, we quantified the proportions of the population in monomeric and polymeric forms

and concluded that nuclear actin, although mostly present in monomeric form, also contains a significant polymeric pool. Based on the accuracy of the fitting, we conclude that the interpretation of FRAP data for nuclear actin using the reaction-diffusion model (3.1) supports recent evidence that actin is present in the nucleus in filamentous form [61].

The third model used to interpret FRAP data is the compartmental model (4.1), consisting of a linear system of ordinary differential equations where the only independent variable is time. The model was motivated by the fact that FRAP data are only time dependent. It describes the same dynamics as the reaction-diffusion model (3.1), but its kinetic parameters are the binding and unbinding rates, and a new parameter, called the diffusional transfer coefficient, that can be thought of as playing the same role as the diffusion coefficient in the reaction-diffusion model (3.1).

In chapter 4, we solved the compartmental model explicitly, and on the basis of the solution we derived the theoretical recovery curve (4.15). Its expression, given by a simple sum of two exponential terms, allows for a significant simplification in the task of parameter estimation. The theoretical recovery curve was used to fit FRAP data of nuclear actin, and the estimated proportions of the filamentous and globular pools were consistent with the estimates obtained using the reaction-diffusion model in chapter 3.

The compartmental model provides a formal mathematical explanation of the empirical procedure of fitting sum of exponential terms to FRAP data of nuclear proteins undergoing binding events proposed recently by Phair *et al.* in [86], and has motivated the current research on FRAP data processing by Li *et al.* [55].

In chapter 5, we showed how the reaction-diffusion model (3.1) and the compartmental model (4.1), describing the same type of dynamic using different approaches, relate and share a common ground. Specifically, we related the diffusional transfer coefficient to the diffusion coefficient by applying the concepts of *residence time*, *transit time* [31, 32], and *mean time to capture* [3]. The resulting relation provides a simplified method for estimating diffusion coefficients. The method was applied to

estimate the diffusion coefficient of nuclear actin, and the estimate was consistent with the one obtained in chapter 3 using the reaction-diffusion model.

In chapter 5, we also carried out a thorough analysis of the dynamics of both the reaction-diffusion model (3.1) and the compartmental model (4.1). Using perturbation analysis, we provided a formal explanation of two limiting dynamical types of behaviour exhibited by experimental recovery data, namely a *reduced diffusive behaviour* and a *biphasic behaviour*. We showed how a rapid turnover, or rapid exchange of binding proteins in the immobile structure, leads to a fluorescence recovery curve that looks as though it was produced by a purely diffusing population, but one that is characterized by a reduced diffusion coefficient. In contrast, slow exchange of proteins leads to a biphasic behaviour distinguished by a fast recovery phase due to the diffusion process and a slow recovery phase due to the turnover process. We identified successfully the FRAP data for histone H1 as having a reduced diffusive behaviour, and the FRAP data for nuclear actin as having a biphasic behaviour. The perturbation analysis also provided a spectrum of simple theoretical recovery curves that simplifies the task of parameter estimation.

From the analysis of the three models used to interpret FRAP data, namely the diffusion model (2.3), the reaction-diffusion model (3.1), and the compartmental model (4.1), we conclude that the specific theoretical recovery curve to be used for the fitting of FRAP data for nuclear proteins depends entirely on the knowledge of the specific protein dynamics, on the characteristics of the experimental recovery curve, and on the criteria and needs of the experimentalists. The results promise to be a useful tool for quantifying the effect of mutations in proteins on their functional dynamics. For example, it would be interesting to complement the work by Hendzel *et al.* in [37] by quantifying the effect of mutations in histone H1 on its affinity to the chromatin structure. Specifically, different sets of FRAP data for different types of mutations in histone H1 would be fitted with theoretical recovery curves in order to obtain estimates of kinetic parameters such as the binding and unbinding rates, and the proportions of the population weakly and strongly bound to the chromatin structure.

In order to facilitate the mathematical analysis of FRAP data by experimentalists, we envision the creation of a simple, user-friendly computer interface that can be used in the lab to obtain numerical estimates of the kinetic parameters describing the dynamics of specific nuclear proteins, based on the theoretical recovery curves obtained from the diffusion model (2.3), the reaction-diffusion model (3.1), and the compartmental model (4.1).

The last model analyzed in this thesis (chapter 6) is not directly related to FRAP experiments. Instead, its purpose is to provide a description of the process of splicing factor compartmentalization. The model, given by the aggregation-reaction-diffusion system (6.10), describes a possible mechanism for the onset of splicing factors compartmentalization, i.e., for the formation of splicing factor compartments or speckles. The model incorporates two biological hypotheses, namely (1) that self-organization of splicing factors is modulated by phosphorylation and dephosphorylation [6, 71, 72, 114], and (2) that an underlying nuclear structure plays a major role in organization of splicing factors [34, 47, 80]. A linear stability analysis of the model and a study of its dispersion relation revealed how slight perturbations of a uniform steady state of the system may lead to potential spatial patterns. A detailed bifurcation analysis of the model illustrated how an increase in the dephosphorylation rate enhances the compartmentalization of splicing factors, and how an increase in the phosphorylation rate has a homogenizing effect on the spatial distribution of splicing factors. This result is consistent with processes that have been shown to lead to speckle disassembly, naturally occurring right before mitosis and initiated by an increase in kinase activity or induced experimentally by increasing the abundance of specific kinases [13, 19, 28, 68, 71, 107]. The bifurcation analysis also allowed us to delimit regions of stability and instability.

The aggregation-reaction-diffusion model illustrates successfully a mechanism for the onset of the compartmentalization. However, the restriction given by (6.6) limits the model from being able to describe the long-term behaviour for the aggregation of splicing factors. This has left us with an interesting modelling problem to be investigated in the future. The idea to solve this problem is to modify the interaction

term among unphosphorylated splicing factors described by equation (6.4). As it is now, the term depends linearly on the average density of unphosphorylated splicing factors. By making this dependence nonlinear on the basis of reasonable biological assumptions, the restriction (6.6) can be withdrawn, and a new model that describes the long-term behaviour for the aggregation of splicing factors can be proposed. One also could go even further, and extend such a new model to two spatial dimensions.

In chapter 6, we emphasized a qualitative mathematical description of the onset of the compartmentalization. For this purpose, we introduced new dynamical parameters with biological significance, such as phosphorylation and dephosphorylation rates, that are of real interest for the experimentalists and for which experimental estimates are currently lacking. Thus, the design of new experiments for estimating parameters seems to have a promising future in this research field.

One of the basic assumptions of the aggregation-reaction-diffusion model is the existence of an underlying nuclear structure. Although this assumption has been proven to be true [34, 47, 79, 80], it still remains a topic of controversy among scientists [84]. For this reason, another future challenge is the development of alternative models for splicing factors compartmentalization in which no underlying nuclear structure is considered. In a broader scientific context, the aggregation-reaction-diffusion model will lead not only to its own improvement but also to the design of experiments for validating or rejecting it.

Finally, we hope that the research carried out in this thesis motivates more interdisciplinary work in the field of nuclear protein dynamics.

Bibliography

[1] D. Axelrod, D.E. Koppel, J. Schlessinger, E. Elson, and W.W. Webb. Mobility measurement by analysis of fluorescence photobleaching recovery kinetics. *Biophys. J.*, 16:1055–1069, 1976.

[2] C.M. Bender and S.A. Orszag. *Advanced Mathematical Methods for Scientists and Engineers.* McGraw-Hill, New York, 1978.

[3] H.C. Berg. *Random Walks in Biology.* Princenton Unviversity Press, New Jersey, 1993.

[4] P.R. Bevington. *Data Reduction and Error Analysis for the Physical Sciences.* McGraw-Hill Book Company, 1969.

[5] R. Bomprezzi, P. Kovanen, and R. Martin. New approaches to investigating heterogeneity in complex traits. *J. Med. Genet.*, 40:553–559, 2003.

[6] J.F. Cáceres, T. Misteli, G.R. Screaton, D.L. Spector, and A. R. Krainer. Role of Modular Domains of SR Proteins in Subnuclear Localization and Alternative Splicing Specificity. *J. Cell Biol.*, 138(2):225–238, 1997.

[7] D.G. Capco, K.M. Wan, and S. Penman. The nuclear matrix: three-dimensional architecture and protein composition. *Cell*, 29(3):847–858, 1982.

[8] G. Carrero, D. McDonald E. Crawford, G. de Vries, and M.J. Hendzel. Using FRAP and mathematical modeling to determine the in vivo kinetics of nuclear proteins. *Methods*, 29:14–28, 2003.

[9] G. Carrero, E. Crawford, M.J. Hendzel, and G. de Vries. Characterizing Fluorescence Recovery Curves for Nuclear Proteins Undergoing Binding Events. *Bull. Math. Biol.*, 6:1515–1545, 2004.

[10] G. Carrero, E. Crawford, J. Th'ng, G. de Vries, and M. J. Hendzel. Quantification of protein-protein and protein-DNA interactions in vivo using Fluorescence Recovery After Photobleaching. *Methods Enzymol.*, 375:415–442, 2004.

[11] M. Chalfie, Y. Tu, G. Euskirchen, W.W. Ward, and D.C. Prasher. Green Fluorescent Protein as a Marker for Gene Expression. *Science*, 263:802–805, 1994.

[12] D. Chen and S. Huang. Nucleolar Components Involved in Ribosome Biogenesis Cycle between the Nucleolus and Nucleoplasm in Interphase Cells. *J. Cell Biol.*, 153:169–176, 2001.

[13] K. Colwill, T. Pawson, B. Andrews, J. Prasad, J.L. Manley, J.C. Bell, and P.I. Duncan. The Clk/Sty protein kinase phosphorylates SR splicing factors and regulates their intracellular distribution. *EMBO (Eur. Mol. Biol. Organ.) J.*, 15:265–275, 1996.

[14] G.M. Cooper. *The Cell: A Molecular Approach.* Sinauer Associates, Inc., Sunderland, Massachusetts, 2000.

[15] A. Coors. Numerial Solutions to the Aggregation Model and to Lubrication Approximation of Hele-Shaw Flow Model. Master's thesis, Department of Physics, The University of Utah, June 1998.

[16] J. Crank. *The Mathematics of Diffusion.* Oxford University Press, Oxford, 1975.

[17] M. Doi and S.F. Edwards. *The Theory of Polymer Dynamics.* Oxford University Press, New York, 1986.

[18] Y. Dou, J. Bowen, Y. Liu, and M.A. Gorovsky. Phosphorylation and an ATP-dependent process increase the dynamic exchange of H1 in chromatin. *J. Cell Biol.*, 158:1161–1170, 2002.

[19] P.I. Duncan, D.F. Stojdl, R.M. Marius, and J.C. Bell. The Clk2 and Clk3 dual-specificity protein kinases regulate the intracellular distribution of SR proteins and influence pre-mRNA splicing. *Exp. Cell Res.*, 241:300–308, 1998.

[20] M. Dundr, U. Hoffmann-Rohrer, Q. Hu Q, I. Grummt, L.I. Rothblum, R.D. Phair, and T. Misteli. A kinetic framework for a mammalian RNA polymerase in vivo. *Science*, 298:1623–1626, 2002.

[21] M. Dundr and T. Misteli. Functional architecture in the cell nucleus. *Biophys. J.*, 356:297–310, 2001.

[22] M. Edidin, Y. Zagyansky, and T.J. Lardner. Measurement of membrane protein lateral diffusion in single cells. *Science*, 191:466–468, 1976.

[23] R. Eils and C. Athale. Computational imaging in cell biology. *J. Cell Biol.*, 161:477–481, 2003.

[24] J. Ellenberg and J. Lipincott-Schwartz. Dynamics and mobility of nuclear envelope proteins in interphase and mitotic cells revealed by green fluorescent protein chimeras. *Methods*, 19:362–372, 1999.

[25] X.-D. Fu. The superfamily of arginine/serine-rich splicing factors. *RNA*, 1:663–680, 1995.

[26] K. Godfrey. *Compartmental Models and Their Applications.* Academic Press, London, 1983.

[27] M. Gong, J.H. Ni, and H.T. Jia. Increased exchange rate of histone H1 on chromatin by exogenous myogenin expression. *Cell Res.*, 12:395–400, 2002.

[28] J.F. Gui, W.S. Lane, and X.-D. Fu. A serine kinase regulates intracellular localization of splicing factors in the cell cycle. *Nature*, 369:678–682, 1994.

[29] K.P. Hadeler and T. Hillen. Coupled Dynamics and Quiescent States. AMI Preprint 01/2005, University of Alberta, 2005.

[30] K.P. Hadeler and M. Lewis. Spatial dynamics of the diffusive logistic equation with a sedentary compartment. *Canad. Appl. Math. Quart.*, 10:473–499, 2002.

[31] S.L. Hardt. Aspects of diffusional transport in microorganisms. In S.R. Caplan and M. Ginzburg, editors, *Energetics and Structure of Halophilic Microorganisms*, pages 591–597. Elsevier, Amsterdam, 1978.

[32] S.L. Hardt. The diffusion transit time: A simple derivation. *Bull. Math. Biol.*, 150:591–597, 1978.

[33] D. He, J.A. Nickerson, and S. Penman. Core filaments of the nuclear matrix. *J. Cell Biol.*, 110:569–580, 1990.

[34] M. Hendzel, F.-M. Boisvert, and D.P. Bazett-Jones. Direct visualization of a protein nuclear architecture. *Mol. Biol. Cell*, 10:2051–2062, 1999.

[35] M. Hendzel, M. Kruhlak, and D.P. Bazett-Jones. Organization of highly acetylated chromatin around sites of heterogeneous nuclear RNA accumulation. *Mol. Biol. Cell*, 9:2491–2507, 1998.

[36] M.J. Hendzel, M.J. Kruhlak, N.A. MacLean, F. Boisvert, M.A. Lever, and D.P. Bazett-Jones. Compartmentalization of regulatory proteins in the cell nucleus. *J. Steroid Biochem. Mol. Biol.*, 76:9–21, 2001.

[37] M.J. Hendzel, M.A. Lever, E. Crawford, and J.P.H. Th'ng. The C-terminal domain is the primary determinant of histone H1 binding to chromatin in vivo. *J. Biol. Chem.*, 279:20028–20034, 2004.

[38] T. Hillen. Transport Equations with Resting Phases. *Europ. J. Appl. Math.*, 14:613–636, 2003.

[39] M.W. Hirsch and S. Smale. *Differential Equations, Dynamical Systems, and Linear Algebra.* Academic Press, New York, 1974.

[40] A.B. Houtsmuller and W. Vermeulen. Macromolecular dynamics in living cell nuclei revealed by fluorescence redistribution after photobleaching. *Histochem. Cell Biol.*, 115:13–21, 2001.

[41] J. Howard. *Mechanics of Motor Proteins and the Cytoskeleton.* Sinauer Associates. Inc., Massachusetts, 2001.

[42] S. Huang and D.L. Spector. Intron-dependent recruitment of pre-mRNA splicing factors to sites of trasncription. *J. Cell Biol.*, 131:719–732, 1996.

[43] K. Jacoson. Lateral diffusion in membranes. *Cell Motil.*, 3:367–373, 1983.

[44] M.K. Keane. *A Very Applied First Couser in Partial Differential Equations.* Prentice-Hall, Inc., New Jersey, 2002.

[45] N. Klonis, M. Rug, I. Harper, M. Wickham, A. Cowman, and L. Tilley. Fluorescence photobleachin analysis for the study of cellular dynamics. *Eur. Biophys. J.*, 31:36–51, 2002.

[46] M.J. Kruhlak, M.A. Lever, W. Fischle, E. Verdin, D. P. Bazzett-Jones, and M. J. Hendzel. Reduced mobility of the Alternate Splicing Factor (ASF) through the nucleoplasm and steady-state speckle compartments. *J. Cell Biol.*, 150:41–52, 2000.

[47] R.I. Kumaran, B. Muralikrishna, and V. Paranaik. Lamin A/C speckles mediate spatial organization of splicing factor compartments and RNA polymerase II transcription. *J. Cell Biol.*, 159:783–793, 2002.

[48] A.I. Lamond and W.C. Earnschaw. Structure and Function in the Nucleus. *Science*, 280:547–553, 1998.

[49] A.I. Lamond and D.L. Spector. Nuclear speckles: a model for nuclear organelles. *Nat. Rev. Mol. Cell Biol*, 4:605–612, 2003.

[50] L.A. Lasky. The nucleoskeleton: go EAST, young man. *Nature Cell Biol.*, 2:E74–E76, 2000.

[51] M.A. Lever, J.P. Th'ng, X. Sung, and M.J. Hendzel. Rapid exchange of histone H1.1 on chromatin in living human cells. *Nature*, 408:873–876, 2000.

[52] J.D. Lewis and D. Tollervey. Like Attracts Like: Getting RNA Processing Together in the Nucleus. *Science*, 288:1385–1389, 2000.

[53] M.A. Lewis. Spatial Coupling of Plant and Hervivore Dynamics: The Contribution of Hervivore Dispersal to Transient and Persistent "Waves" of Damage. *Theor. Popul. Biol.*, 45:277–312, 1994.

[54] M.A. Lewis and G. Schmitz. Biological Invasion of and Organism with Separte Mobile and Stationary States: Modeling and Analysis. *FORMA*, 11:1–25, 1996.

[55] T. Li, W. Zhou, and Q. Luo. FRAP data processing with three-exponential fitting method. *Proc. SPIE*, 5696:159–167, 2005.

[56] P.A. Liebman and G. Entine. Lateral diffusion of visual pigment in photoreceptor disk membranes. *Science*, 185:457–459, 1974.

[57] J. Lippincott-Schwartz, J.F. Presley, K.J.M. Zaal, K. Hirschberg, C.D. Miller, and J. Ellenberg. Monitoring the Dynamics and Mobility of Membrane Proteins Tagged with Green Flourescent Protein. *Methods Cell Biol.*, 58:261–281, 1999.

[58] J. Lippincott-Schwartz, E. Snapp, and A. Kenworthy. Studying protein dynamics in living cells. *Nat. Rev. Mol. Cell Biol*, 2:444–456, 2001.

[59] J.L. Manley and R. Tacke. SR proteins and splicing control. *Genes Dev.*, 10:1569–1579, 1996.

[60] A.G. Matera. Nuclear bodies: multifaceted subdomains of the interchromatin space. *Trends Cell Biol.*, 9:302–309, 1999.

[61] D. McDonald, G. Carrero, E. Crawford, Christi Andrin, G. de Vries, and M.J. Hendzel. Nuclear beta actin exists in a dynamic equilibrium between filaments and monomers in mammalian cells. In preparation.

[62] J.L. McGrath, Y. Tardy, C.F. Dewey, J.J. Meister, and J.H. Hartwig. Simultaneous measurements of actin filament turnover, filament fraction, and monomer diffusion in endothelial cells. *Biophys. J.*, 75:2070–2078, 1998.

[63] J.G. McNally, W.G. Mller, D. Walker, R. Wolford, and G.L. Hager. The Glucocorticoid Receptor: Rapid Exchange with Regulatory Sites in Living Cells. *Science*, 287:1262–1265, 2000.

[64] T. Misteli, , and D.L. Spector. Applications of the green fluorescent protein in cell biology and biotechnology. *Nature Biotechnol.*, 15:961–964, 1997.

[65] T. Misteli. Cell bioligy of transcription and pre-mRNA splicing: nuclear architecture meets nuclear function. *J. Cell Sci.*, 113:1841–1849, 2000.

[66] T. Misteli. The concept of self-organization in cellular architecture. *J. Cell Biol.*, 155(2):181–185, 2001.

[67] T. Misteli. Protein Dynamics: Implications for Nuclear Architecture and Gene Expression. *Science*, 291:843–847, 2001.

[68] T. Misteli, J.F. Cáceres, and D.L. Spector. The dynamics of a pre-mRNA splicing factor in living cells. *Nature*, 387:523–527, 1997.

[69] T. Misteli, A. Gunjan, R. Hock, M. Bustin, and D.T. Brown. Dynamic binding of histone H1 to chromatin in living cells. *Nature*, 408:877–881, 2000.

[70] T. Misteli and D.L. Spector. Serine/threonine phosphatase 1 modulates the subnuclear distribution of pre-mRNA spling factors. *Mol. Biol. Cell*, 7:1559–1572, 1996.

[71] T. Misteli and D.L. Spector. Protein phosphorylation and the nuclear organization of pre-mRNA splicing. *Trends Cell Biol.*, 7:135–138, 1997.

[72] T. Misteli and D.L. Spector. The cellular organization of gene expression. *Curr. Opin. Cell Biol.*, 10:322–331, 1998.

[73] A. Mogilner and L. Edelstein-Keshet. Selecting a common direction i: How orientational order can arise from simple contact responses between interacting cells. *J. Math. Biol.*, 33:619–660, 1995.

[74] A. Mogilner and L. Edelstein-Keshet. Spatio-angular order in populations of self-aligning objects: formation of oriented patches. *Physica D*, 89:346–367, 1996.

[75] A. Mogilner and L. Edelstein-Keshet. A non-local model for a swarm. *J. Math. Biol.*, 38:534–570, 1999.

[76] A. Mogilner, L. Edelstein-Keshet, and G.B. Ermentrout. Selecting a common direction ii. Peak-like solutions representing total alignment of cell clusters. *J. Math. Biol.*, 34:811–842, 1996.

[77] J.D. Murray. *Mathematical Biology. Biomathematics Texts*, volume 19. Springer-Verlag, New York, 1993.

[78] R.H. Myers. *Classical and Modern Regression with Applications.* Duxbury Press, Boston, 1986.

[79] G. Nalepa and J.W. Harper. Visualization of a Highly Organized Intranuclear Network of Filaments in Living Cells. *Cell Motil. Cytoskeleton*, 59:94–108, 2004.

[80] J.A. Nickerson. Experimental observations of a nuclear matrix. *J. Cell Sci.*, 114:463–474, 2001.

[81] L.A. Parada, J.J. Roix, and T. Misteli. An uncertainty principle in chromosome positioning. *Trends Cell Biol.*, 13:393–396, 2003.

[82] T. Pederson. Movement and localization of RNA in the cell nucleus. *FASEB J.*, 13:S238–S242, 1999.

[83] T. Pederson. Diffusional protein transport within the nucleus: a message in the medium. *Nature*, 2:E73–E74, 2000.

[84] T. Pederson. Half a Century of "The Nuclear Matrix". *Mol. Biol. Cell*, 11:799–805, 2000.

[85] T. Pederson. Protein Mobility within the Nucleus–What Are the Right Moves? *Cell*, 104:635–638, 2001.

[86] R.D. Phair, S.A. Gorski, and T. Misteli. Measurement of Dynamic Protein Binding to Chromatin *In Vivo*, Using Photobleaching Microscopy. *Methods Enzymol.*, 375:393–414, 2004.

[87] R.D. Phair and T. Misteli. High mobility of proteins in the cell nucleus. *Nature*, 404:604–609, 2000.

[88] R.D. Phair and T. Misteli. Kinetic modelling approaches to in vivo imaging. *Nat. Rev. Mol. Cell Biol*, 2:898–907, 2001.

[89] J. Politz and A. Pombo. Genomics meets nanoscience: probing genes and the cell nucleus at 10-9 meters. *Genome Biol.*, 3:REPORTS4007, 2002.

[90] M. Poo and R.A. Cone. Lateral diffusion of rhodopsin in the photoreceptor membrane. *Nature*, 247:438–441, 1974.

[91] O.J. Rando, K. Zhao, and G.R. Crabtree. Searchin for a function for nuclear actin. *Trends Cell Biol.*, 10:92–97, 2000.

[92] R. Rizzuto, M. Brini, F. De Giorgi, R. Rossi, R. Heim, R.Y. Tsien, and T. Pozzan. Double labelling of subcellular structures with organelle-targeted GFP mutants *in vivo*. *Curr. Biol.*, 6:183–188, 1996.

[93] M. Ronen, R. Rosenberg, B. Shraiman, and U. Alon. Assigning numbers to the arrows: parameterizing a gene regulation network by using accurate expression kinetics. *Proc. Natl. Acad. Sci. USA*, 99:10555–10560, 2002.

[94] M. Schindler, J.F. Holland, and M. Hogan. Lateral diffusion in nuclear membranes. *J. Cell Biol.*, 100:1408–1414, 1985.

[95] J. Schlessingerand, D.E. Koppel, D. Axelrod, K. Jacobson, W.W. Webb, and E.L. Elson. Lateral transport in cell membranes: mobility of concanavalin A receptors on myoblasts. *Proc. Natl. Acad. Sci. USA*, 73:2409–2413, 1976.

[96] O. Seksek, J. Biwersi, and A.S. Verkman. Translational diffusion of macromolecule-sized solutes in cytoplasm and nucleus. *J. Cell Biol.*, 138:131–142, 1997.

[97] D.L. Spector. Macromolecular domains within the cell nucleus. *Annu. Rev. Cell Biol.*, 9:265–315, 1993.

[98] D.L. Spector. Nuclear domains. *J. Cell Sci.*, 114:2891–2893, 2001.

[99] D.A. Stavera and J.G. McNally. Fluorescence Recovery after Photobleaching (FRAP) Methods for Visualizing Protein Dynamics in Living Mammalian Cell Nuclei. *Methods Enzymol.*, 375:443–455, 2004.

[100] D.L. Stenoien, K. Patel, M.G. Mancini, M. Dutertre, C. L. Smith, B. W. O'Malley, and M. A. Mancini. FRAP reveals that mobility of oestrogen receptor-α is ligand- and proteasome-dependent. *Nature Cell Biol.*, 3:15–23, 2001.

[101] Y. Tardy, J.L. McGrath, J.H. Hartwig, and C.F. Dewey. Interpreting photoactivated fluorescence microscopy measurements of steady-steady actin dynamics. *Biophys. J.*, 69:1674–1682, 1995.

[102] R.Y. Tsien. The green fluorescent protein. *Annu. Rev. Biochem.*, 67:509–544, 1998.

[103] P. Turchin. Population consequences of aggregative movement. *J. Anim. Eco.*, 58:75–100, 1989.

[104] P. Turchin. *Quantitative Analysis of Movement: Measuring and Modeling Population Redistribution in Animals and Plants.* Sinauer Associates, Inc., Sunderlan, MA, 1998.

[105] R. Verheijen, H. Kuijpers, P. Vooijs, W. van Venrooij, and F. Ramaekers. Protein composition of nuclear matrix preparations from HeLa cells: an immunochemical approach. *J. Cell Sci.*, 80:103–122, 1986.

[106] A.S. Verkman. Solute and macromolecule diffusion in cellular aqueous compartments. *Trends Biochem. Sci.*, 27:27–33, 2002.

[107] H.-Y. Wang, W. Lin, J.A. Dyck, J.M. Yeakley, Z. Songyang, L. C. Cantley, and X. D. Fu. SRPK2: a differentially expressed SR protein-specific kinase involved in mediating the interaction and localization of pre-mRNA splicing in mammalian cells. *J. Cell Biol.*, 140:737–750, 1998.

[108] M. Wasser and W. Chia. The EAST protein of Drosophila controls an expandable nuclear endoskeleton. *Nature Cell Biol.*, 2:268–275, 2000.

[109] W.W. Webb, L.S. Barak, D.W. Tank, and E.S. Wu. Molecular mobility on the cell surface. *Biochem. Soc. Symp.*, 46:191–205, 1981.

[110] J. White and E. Stelzer. Photobleaching GFP reveral protein dynamics inside live cells. *Trends Cell Biol.*, 9:61–65, 1999.

[111] D.E. Wolf. Designing, building, and using a fluorescence recovery after photobleaching instrument. *Methods Cell Biol.*, 30:271–306, 1989.

[112] D.E. Wolf. Fundamentals of fluorescence and fluorescence microscopy. *Methods Cell Biol.*, 72:157–184, 2003.

[113] S.H. Xiao and J.L. Manley. Phosphorylation of the ASF/SF2 RS domain affets both protein-protein and protein-RNA interactions and is necessary for splicing. *Genes Dev.*, 11:334–344, 1997.

[114] S.H. Xiao and J.L. Manley. Phosphorylation-dephosphorylation differentially affects activities of splicing factor ASF/SF2. *EMBO (Eur. Mol. Biol. Organ.) J.*, 17:6359–6367, 1998.

[115] H. Yokoe and T. Meyer. Spatial dynamics of GFP-tagged proteins investigated by local fluorescence enhancement. *Nature Biotechnol.*, 14:1252–1256, 1996.

[116] E. Zauderer. *Partial Differential Equations of Applied Mathematics.* John Wiley & Sons, Inc., New York, 1998.